PHYSICS AND TECHNOLOGY OF THE INFRARED DETECTION SYSTEMS BASED ON HETEROJUNCTIONS

A THESIS SUBMITTED TO
THE GRADUATE SCHOOL OF NATURAL AND APPLIED SCIENCES
OF
THE MIDDLE EAST TECHNICAL UNIVERSITY

BY

BÜLENT ASLAN

IN PARTIAL FULFILLMENT OF THE REQUIREMENTS FOR THE DEGREE OF
DOCTOR OF PHILOSOPHY
IN
THE DEPARTMENT OF PHYSICS

MARCH 2004

Approval of the Graduate School of Natural and Applied Sciences

Prof. Dr. Canan Özgen
Director

I certify that this thesis satisfies all the requirements as a thesis for the degree of Doctor of Philosophy.

Prof. Dr. Sinan Bilikmen
Head of Department

This is to certify that we have read this thesis and that in our opinion it is fully adequate, in scope and quality, as a thesis for the degree of Doctor of Philosophy.

Prof. Dr. Raşit Turan
Supervisor

Examining Committee Members

Prof. Dr. Raşit TURAN _____

Prof. Dr. Özcan ÖKTÜ _____

Prof. Dr. Çiğdem ERÇELEBİ _____

Assoc. Prof. Dr. Mehmet PARLAK _____

Assoc. Prof. Dr. Cengiz BEŞİKÇİ _____

ABSTRACT

PHYSICS AND TECHNOLOGY OF THE INFRARED DETECTION SYSTEMS BASED ON HETEROJUNCTIONS

Aslan, Bülent

Ph. D., Department of Physics

Supervisor: Prof. Dr. Raşit Turan

March 2004, 127 pages

The physics and technology of the heterojunction infrared photodetectors having different material systems have been studied extensively. Devices used in this study have been characterized by using mainly optical methods, and electrical measurements have been used as an auxiliary method. The theory of internal photoemission in semiconductor heterojunctions has been investigated and the existing model has been extended by incorporating the effects of the difference in the effective masses in the active region and the substrate, nonspherical-nonparabolic bands, and the energy loss per collisions. The barrier heights (correspondingly the cut-off wavelengths) of SiGe/Si samples have been found from their internal photoemission spectrums by using the complete model which has the wavelength and doping concentration dependent free carrier absorption parameters. A qualitative model describing the mechanisms of photocurrent generation in SiGe/Si HIP devices has been presented. It has been shown that the performance of our devices depends significantly on the applied bias and the operating temperature. Properties of internal photoemission in a PtSi/Si Schottky type infrared detector have also been studied. InGaAs/InP quantum well

photodetectors that covers both near and mid-infrared spectral regions by means of interband and intersubband transitions have been studied. To understand the high responsivity values observed at high biases, the gain and avalanche multiplication processes have been investigated. Finally, the results of a detailed characterization study on a systematic set of InAs/GaAs self-assembled quantum dot infrared photodetectors have been presented. A simple physical picture has also been discussed to account for the main observed features.

Keywords: Infrared photodetectors, internal photoemission, SiGe/Si, dual-band, quantum well, quantum dot.

ÖZ

ÇOKLUEKLEM TABANLI KIZILÖTESİ ALGILAMA SİSTEMLERİNİN FİZİĞİ VE TEKNOLOJİSİ

Aslan, Bülent
Doktora, Fizik Bölümü
Tez Yöneticisi: Prof. Dr. Raşit Turan

Mart 2004, 127 sayfa

Farklı malzeme sistemlerine sahip çokluekleklem kızılötesi fotoalgılayıcıların fiziği ve teknolojisi geniş ölçüde çalışıldı. Bu çalışmada kullanılan aygıtlar, temel olarak optiksel yöntemler kullanılarak nitelendirildi ve yardımcı bir yöntem olarak elektriksel ölçümler kullanıldı. Yarıiletken çokluekleklemlerdeki dahili ışılsalım teorisi incelendi ve varolan model, aktif bölge ve alttaş etkin kütleleri arasındaki farkın, küresel olmayan-parabolik olmayan bantların ve çarpışma başına düşen enerji kaybının etkileriyle birleştirilerek genişletildi. SiGe/Si örneklerin engel yükseklikleri (denkçe eşik dalgaboyları), dahili ışılsalım tayflarından dalgaboyu ve katkı miktarı bağımlı özgür taşıyıcı soğurması parametrelerine sahip tam model kullanırak bulundu. SiGe/Si HIP aygıtlardaki fotoakım oluşma mekanizmalarını açıklayan nitel bir model sunuldu. Aygıtlarımızın performanslarının uygulanan voltaja ve çalışma sıcaklığına önemli derecede bağlı olduğu gösterildi. PtSi/Si Schottky tipi kızılötesi algılayıcılardaki dahili ışılsalım özellikleri de çalışıldı. Bantlar ve altbantlar arasındaki geçişler yoluyla hem yakın hem de orta-kızılötesi bölgeyi kapsayan InGaAs/InP kuatum kuyu fotoalgılayıcılar çalışıldı. Büyük besleme değerlerinde gözlenen yüksek tepkiselliği anlamak için kazanç ve çığ

çoğalma olayları incelendi. Son olarak, bir InAs/GaAs kendiliğinden oluşan kuantum nokta kızılötesi fotoalgılayıcılar grubu üzerindeki ayrıntılı nitelendirme çalışması sonuçları sunuldu. Gözlenen temel özellikleri değerlendirmek için basit bir fiziksel resim tartışıldı.

Anahtar kelimeler: Kızılötesi fotoalgılayıcılar, dahili ışılsalım, SiGe/Si, ikili-bant, kuantum kuyu, kuantum nokta.

ACKNOWLEDGMENTS

I must express my gratitude to my supervisor Prof. Dr. Raşit Turan for giving me the chance to work with him. His unconditional guidance and help throughout my graduate study is a great value to me. I would also like to thank him for his enthusiastic support as a friend.

Dr. H. C. Liu is another important person whom I must thank very much. It was my privilege to work with him. I have greatly benefited from his knowledge and scientific vision.

I intensely acknowledge my colleagues in the laboratories both here at METU and at the Institute for Microstructural Sciences, National Research Council of Canada, Ottawa for their genial attitude to me.

I would like to thank the Scientific and Technical Research Council of Turkey (TUBITAK) for financial support during my stay at the National Research Council, Canada.

Finally, I would like to express my endless gratitude to my parents, without whom I would not have had the opportunity to carry on this study.

TABLE OF CONTENTS

ABSTRACT iii
ÖZ v
ACKNOWLEDGMENTS vii
TABLE OF CONTENTS vii
LIST OF FIGURES xi
LIST OF TABLES xvi

CHAPTER
1. INFRARED DETECTORS 1
1.1 Introduction 1
1.2 Photon Detectors 3
1.2.1 Mercury Cadmium Telluride (HgCdTe) Photodiodes 4
1.2.2 Schottky Barrier Infrared Photodetectors 5
1.2.3 Heterojunction Internal Photoemission (HIP) Detectors 6
1.2.4 Blocked Impurity Band (BIB) Detectors 6
1.2.5 Homojunction Internal Photoemission Detectors 6
1.2.6 Quantum Well Infrared Photodetectors (QWIP) 7
1.2.7 Quantum Dot Infrared Photodetectors (QDIP) 8
1.3 Thermal Detectors 8
1.3.1 Bolometers 9
1.3.2 Pyroelectric Detectors 9
1.3.3 Thermoelectric Detectors 10
2. THEORY OF INTERNAL PHOTOEMISSION IN HETEROJUNCTIONS 11

2.1 Model for Escape Probability 13
2.2 Band Correction over Effective Mass 24
2.3 Effects of Multiple Reflections and Scattering 28
2.4 Quantum Mechanical Effects 34
2.5 Effect of e-p Collisions and Energy Losses 34
2.6 Analysis: Effects of the Scattering Parameters on the Yield 37
2.7 Infrared Absorption 42
3. MECHANISMS OF PHOTOCURRENT GENERATION IN SiGe/Si HIP INFRARED PHOTODETECTORS 45
3.1 Experimental Details and Device Operation 46
3.1.1 Device Operation 48
3.2 Spectral Photoresponse and a Simple Model 49
3.2.1 Fowler Analysis 53
3.3 Responsivity versus Voltage 55
3.4 I-V Characteristics and Activation Energy Analysis 57
3.5 Samples with Different Parameters 59
4. DOUBLE-BARRIER LONG WAVELENGTH SiGe/Si HIP INFRARED PHOTODETECTORS 63
4.1 Experimental Details 63
4.2 Experimental Results and Discussions on the Double-Barrier SiGe/Si HIP 65
4.2.1 Spectral Photoresponse 65
4.2.2 Fowler Analysis and Responsivity 67
4.2.3 I-V and Activation Energy Analysis 69
5. INTERNAL PHOTOEMISSION SPECTROSCOPY FOR PtSi/p-Si INFRARED DETECTORS 73
5.1 Internal Photoemission in Metal/Semiconductor Systems 74
5.2 Experimental Details 77
5.3 PtSi/p-Si Spectrum 79
5.4 Effect of the Ice Formation on the Detector's Response 80
5.5 I-V Characteristics of PtSi/p-Si Diodes 83
6. InGaAs/InP QUANTUM WELL INFRARED PHOTODETECTORS .. 87

6.1 Basic principles of QWIPs 88
6.2 InGaAs/InP Dual-Band QWIP 90
6.3 Experimental Details 91
6.4 Spectral Photoresponse 91
6.5 Responsivity versus Voltage 94
6.6 Noise and Avalanche Multiplication 94
7. DETAILED CHARACTERIZATION OF A SYSTEMATIC SET OF QUANTUM DOT INFRARED PHOTODETECTORS 99
7.1 Anticipated Advantages of QDIPs 100
7.2 Experimental Details 103
7.3 Physical Picture 104
7.4 Results and Discussion 107
8. CONCLUSION 113

REFERENCES 116
VITA 125

LIST OF FIGURES

FIGURE

1.1 Transmission spectrum of the atmosphere 2

2.1 Valence band profile and the energy levels..... 13

2.2 Distribution of holes in momentum space for a spherical Fermi surface at 0 K. a) $h\nu < E_F$, b) $h\nu > E_F$ 15

2.3 3D graphical representation of the carriers in momentum space for m_2 (=0.6 m_0) > m_1. a) m_1 = 0.3 m_0, b) m_1 = 0.55 m_0, c) Floating 3D view of the system showing the intersection..... 17

2.4 3D graphical representation of the carriers in momentum space for a) m_2 = m_1 = 0.6 m_0, b) Floating 3D view of the system showing the intersection..... 18

2.5 3D graphical representation of the carriers in momentum space for m_2 (=0.6 m_0) < m_1. a) m_1 = 0.7 m_0, b) m_1 = 0.9 m_0, c) Floating 3D view of the system showing the intersection..... 19

2.6 Escape volume for holes in momentum space for three different cases (the hatched region corresponds to the holes that may escape over the barrier). a) m(SiGe) < m(Si), b) m(SiGe) = m(Si), c) m(SiGe) > m(Si) .. 20

2.7 Geometrical definitions of the parameters in momentum space 21

2.8 Calculated effective mass and Fermi energy versus doping concentration graph for different x values at 4 K (from reference [69]) 24

2.9 Calculated yields versus photon energy graph for different *M* values when the constant effective mass is considered 25

2.10 Calculated yields versus effective masses ratio M for different photon energies when the constant effective mass is considered 26
2.11 Calculated yields versus photon energy graph for different M values when the energy dependent effective mass is considered 27
2.12 Calculated yields versus effective masses ratio M for different photon energies when the energy dependent effective mass is considered 27
2.13 a) 3-dimensional representation of the variation of the yield with respect to the effective masses ratio and the energy of the incident photons. b) The projections of the 3D surface on each plane in the shaded form 28
2.14 The effect of different substrate (Si in this case) effective masses on the yield 29
2.15 Schematic diagram showing the different processes during the motion of an excited carrier before emission 30
2.16 Diagram illustrating the definition of the spherical shell of emission 33
2.17 Effect of the film thicknesses on the yield versus energy plots 38
2.18 Yield versus energy plots for several hot-hole/phonon scattering mean free paths (L_p) with an energy loss per collision ($\hbar\omega$) of a) 1 meV, and b) 10 meV 39
2.19 Yield versus energy plots for several hot-hole/cold electron scattering mean free paths (L_e) 40
2.20 Effect of the energy loss per collisions ($\hbar\omega$) term on the yield 41
2.21 Yield versus energy plots for different Fermi energies 41
2.22 Variation of the yield with different barrier height values 42
2.23 a) External yield (product of the internal yield and the optical absorption) versus energy plot, b) same graph in the form of Fowler plot 44
3.1 Schematic device structure with layer thicknesses and the valence band edge profile showing the basic operation principle of the SiGe/Si HIP investigated here 47

3.2 The schematic representation of a device: (a) cross-section of the device and (b) the top view of the mesa with ring shaped Al ohmic contact 48
3.3 Responsivity measurement setup 48
3.4 Spectral photoresponse curves under different bias conditions at 10 K. The voltage values written in the legend are the potential differences across the device when it is illuminated by the light coming from the IR source. The inset shows the change in the photovoltage with the applied bias for 10 K measurements 50
3.5 Qualitative physical picture for interpreting the experimental results. The potential difference is negative for (a) and positive for (b). The bottom contact is the ground and arrows show the direction of the photoexcited holes' direction 52
3.6 Fowler plot of the experimental data (circles) and the theoretical fit (solid lines) for the device biased with 75 mV and -37 mV 54
3.7 Responsivity versus voltage characteristics of the device at different temperatures. Measurements have been performed at 7.14 μm 56
3.8 Semilogarithmic plot of I-V characteristics of the sample under different experimental conditions 58
3.9 Activation energy plot for determination of barrier height 58
3.10 Spectral photoresponse curves for a set of samples. Samples were biased with 75 mV except 1105 which is biased with 20 mV 60
3.11 Activation energy plots for determination of barrier height (for the entire set of samples) 61
3.12 Responsivity versus voltage characteristics of the devices at 10 K. Measurements have been performed at 8.06 μm, 8.06 μm, 7.14 μm, 6.67 μm, and 6.25 μm, respectively 62
4.1 Schematic device structure with layer thicknesses for both sample 1111 and sample 1105 (a) and the valence band edge profile showing the operation principle (b) 65
4.2 Spectral photoresponse curves under positive bias at different temperatures for sample 1111 (a) and for sample 1105 (b) under

small positive bias. Applied bias values are 250 mV (10 K), 200 mV (20 K), 125 mV (30 K), and 30 mV (50 K) for sample 1111. As for sample 1105, 20 mV was applied at both temperatures. Note that 20 K spectrum was multiplied by 10 66
4.3 Responsivity versus voltage characteristics of the sample 1111 at different temperatures; 10 K and 50 K. Measurements have been performed at 5.8 μm 68
4.4 Fowler plots of internal photoemission spectra for the sample 1111 at 10 K and 50 K 69
4.5 Semilogarithmic plot of I-V characteristics of the samples 1111 and 1105 under different experimental conditions 71
4.6 Activation energy plot for determination of barrier height 72
5.1 Energy levels in metal-semiconductor band structure 75
5.2 Escape cap for holes in momentum space. The hatched region corresponds to the holes that may escape over the barrier 76
5.3 Cross-section of the PtSi/p-Si diodes 77
5.4 Optoelectronic spectrum measurement system 78
5.5 Internal photoemission spectrum of the PtSi/p-Si diode. Curves fitted by modified Fowler theory and extended theory are also shown 80
5.6 a) Effect of different vacuum conditions on the internal photoemission spectrum of the PtSi/p-Si diode. b) Direct comparison of the observed dip to the spectrum of the ice taken from Ref. [109]. (Experimental data are normalized against the theoretical response curve). The solid line (ice's absorption spectrum) belongs to the left axis and the others (experimental data) belong to the right axis. Marker types are same as (a) 81
5.7 I-V characteristics of the PtSi/p-Si diode at different temperatures for (a) forward and (b) reverse bias. Fitted lines for the extraction of the barrier height and the ideality factor are also shown 84
6.1 Density of states versus energy for 0, 2, and 3-dimensional carries 88
6.2 Schematic band diagram of a quantum well showing the basics of infrared absorption: Intersubband absorption can take place between

the energy levels of a QW associated with the conduction or valence band while the interband absorption is between the bands 89

6.3 a) Schematic energy-band diagram of the device used here under bias. The arrows indicate the processes for dual-band detection. b) 45^{o} facet measurement geometry for the light coupling..... 92

6.4 Spectral photoresponse curves for samples 235 and 236 at device temperature of 77 K. The two parts are separately normalized. The spectral shapes are insensitive to the bias values and voltages in the range of 2 – 3 V are used for the curves shown 93

6.5 Responsivity versus voltage characteristics of (a) sample 235 and (b) sample 236 at device temperature of 77 K. Measurements in MIR were performed at 9.4 and 8.6 μm for samples 235 and 236, respectively. For NIR calibration 0.96 μm light was used for both devices 95

6.6 a) Dark current (density) versus voltage characteristic, and b) photoconductive gain g_{ph} and noise gain g_n, and the ratio (g_n / g_{ph}) of the two gains versus voltage for sample 236. The latter is the excess noise factor *F* which approximately equals the multiplication factor *M*..... 97

7.1 Schematic (a) layers of a QWIP and QDIP and (b) potential profile for both structures under bias 101

7.2 Schematic conduction band inter-shell transitions in a self-assembled InAs/GaAs quantum dot. Solid and dotted arrows represent transitions for *E//z* and *E//x-y* polarized lights, respectively. The top part is for transitions originating from the s shell, and the bottom for p shell..... 106

7.3 Dark current characteristics for all samples at two different temperatures, 77 K (a) and 6 K (b)..... 108

7.4 Comparison of mid-infrared photoresponse curves of samples having different numbers of electrons per dot for (a) P-polarized and (b) S-polarized lights. The P-spectra are normalized to unity, while the S-

spectra are scaled by the same amounts for comparison. The inset to the bottom panel shows the experimental geometry 109

7.5 Normalized far-infrared photoresponse curves for (a) P-polarized and (b) S-polarized lights. To compare the relative magnitudes between P and S responses, the lower panel curves should be multiplied by 0.6, 0.8, and 3.8 for sample A, B, and C, respectively, for example, the solid curve in (b) should be multiplied by 0.6 to compare with the curve in (a)..... 111

7.6 Responsivity versus voltage characteristics for samples A, B and C at 7.14 μm (174 meV) and 6 K..... 112

LIST OF TABLES

TABLE

3.1 Structural parameters of the samples 60

3.2 Parameters used in Fowler analysis and the barrier height values obtained from both electrical and optical measurements 62

5.1 Barrier height and ideality factor (n) values extracted from I-V analysis of PtSi/p-Si diodes at various temperatures 85

5.2 Barrier height values of PtSi/p-Si obtained by I-V analysis and internal photoemission spectroscopy (IPS) analysis 86

7.1 Structural parameters obtained from atomic force microscopy and plan-view transmission electron microscopy observations to estimate the number of the electrons per dot 104

CHAPTER 1

INFRARED DETECTORS

1.1 Introduction

Infrared (IR) spectrum is a part of the electromagnetic spectrum: It is defined as the region just above the visible (0.7 μm) to millimeter waves (1000 μm). This is the region where every object having non-zero temperature emits "thermal radiation". The characteristics of this radiation depend on the temperature and the wavelength. Since the human eye responds well to the visible light but poorly to infrared radiation, almost all the information encoded in the infrared radiation is not directly detected by the human eyes. Therefore, it is necessary to develop a device if thermal radiation is to be detected.

The interest in the detection of IR radiation has centered mainly on the two atmospheric windows, 3-5 μm and 8-12 μm, based on two facts: (*i*) Most of the energy emitted by an object at around room temperature is in 3-14 μm wavelength region [1]. (*ii*) Atmospheric transmission is the highest in these windows. Fig. 1.1 shows the infrared transmission over a spectral range from 0.7 μm to 15 μm [2]. In recent years, along with the technological development/progress, there has been increasing interest in longer wavelengths stimulated by space applications.

The main function of a detector is the conversion of the radiation falling on it into an electrical signal for further investigation. This can be done by using many different physical phenomena. IR detectors are divided into two basic groups; photon detectors (or photodetectors) and thermal detectors which differ by the

physical mechanism used for the detection process. In the photon detectors, the radiation is absorbed within the material by interaction with electrons either bound to lattice atoms or to impurity atoms or with free electrons. This interaction produces parameter changes (such as voltage, current, resistance etc.) that are detected by external measurement circuits. As in thermal detectors, the radiation must alter the temperature of the sensor resulting in the change in some basic property of the device. Thermal detectors produce a signal that is independent of energy or wavelength, while photon detectors are dependent on the number of photons and their energy.

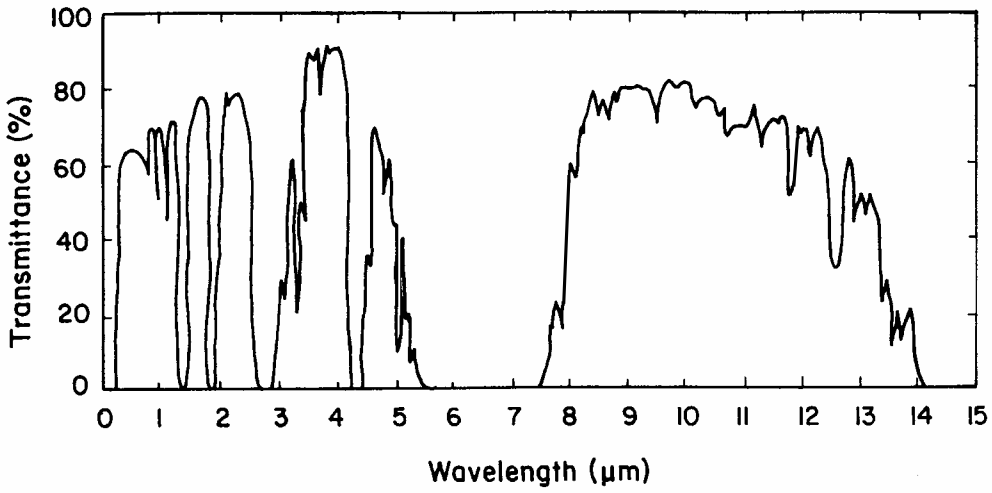

Fig. 1.1 Transmission spectrum of the atmosphere.

This thesis is designed in a way that each chapter is self-contained. This chapter is devoted to the general discussion of infrared detectors. In chapter 2, the theory of internal photoemission in semiconductor heterojunctions is discussed and a complete model is derived. In chapters 3 and 4, SiGe/Si HIP infrared photodetectors are characterized by optical and electrical methods. Additionally, a qualitative model describing the photocurrent generation mechanisms is presented. PtSi/Si Schottky type infrared photodetectors are given in chapter 5. In the following chapter (chapter 6), InGaAs/InP dual-band quantum well infrared photodetectors showing high responsivity feature at high biases are presented. Finally, the results

of a detailed characterization study on a systematic set of InAs/GaAs self-assembled quantum dot infrared photodetectors are presented in chapter 7. All samples except PtSi/Si ones used in this study were grown and processed at the Institute for Microstructural Sciences, National Research Council, Ottawa, Canada.

1.2 Photon Detectors

Photon detectors are quantum counters where the incident photons create electrons that are conducted to the external measurement circuit. They are usually characterized by a minimum energy of photon detection or, equivalently, a long wavelength cut-off beyond which the device has no response to the incident photon. Photon detectors having long wavelength limits (>3 μm) generally need to be cooled to achieve good signal-to-noise ratio and a fast response.

Depending on the nature of the interaction, the photon detectors are divided into sub-groups: Intrinsic detectors (e.g. PbS, PbSe, HgCdTe, InGaAs, InAs, InSb etc), extrinsic detectors (e.g. Si:Ge, Si:As, Ge:Cu etc.), free carrier detectors (PtSi, IrSi etc.), quantum well detectors (GaAs/AlGaAs, InGaAs/AlGaAs, InAs/InAsSb, etc.), and quantum dot detectors (InAs/GaAs, Ge/Si, etc). Depending also on how the electric signal is developed, there are various modes such as photoconductive, photovoltaic, and photoemissive ones. There are several detailed review articles and texts on these photon detectors in the literature [3-12].

Detectors are characterized by figures of merit that allow comparison of different detectors. The most important figure of merit is the responsivity of the photodetector which is determined by the quantum efficiency, η, and the gain, g, if available, and can be written as [5]

$$R = \frac{\lambda_c}{hc} e \eta g \tag{1.1}$$

where λ_c is the cut-off wavelength of the detector. The quantum efficiency value describes how well the detector is coupled to the radiation to be detected. It is usually defined as the number of carriers generated per incident photon. The idea of

gain is proposed as a simplifying concept for the understanding of photoconductive phenomena [13] and defined as the number of carriers passing contacts per one generated carrier. There are some other figures of merit which are not mentioned here such as noise equivalent power (NEP), detectivity (D^*), photon-noise-limited performance, etc., since they are not the main emphases of the thesis.

In the following sub-sections, some of the important photon detectors are presented for the sake of completeness.

1.2.1 Mercury Cadmium Telluride (HgCdTe) Photodiodes

From fundamental considerations Mercury-Cadmium Telluride (MCT) is the most important and worldwide attracted semiconductor alloy system for IR detectors in the spectral range between 1 and 25 μm [8, 14 and references therein]. This material is a ternary compound that alloys two binary compounds HgTe and CdTe. Its chemical formula is defined as $Hg_{1-x}Cd_xTe$. By tailoring the composition ratio of the material (i.e. x value in $Hg_{1-x}Cd_xTe$), the energy gap of this material varies from semimetallic for HgTe (x = 0) with a gap of -0.3 eV to semiconducting CdTe (x = 1), which has a gap of 1.65 eV [15]. The negative sign for HgTe shows that the bottom of the conduction band is lower than the top of the valence band. Thus, the longer wavelength response can be achieved by increasing the Hg percentage in the compound. These detectors are made by building a *p-n* junction and the optical absorption occurs at or near the junction. If a photon with sufficient energy is absorbed in photoactive region, an electron will gain sufficient energy to move into the conduction band and leave a hole behind. With the movement of these photogenerated electron-hole pair to the detector's terminal a current flow is set up. Note that they can also be designed as a photoconductive detector by using a slab of material in which the created electron-hole pairs are separated by the applied bias. Therefore, the bandgap energy determines the cut-off wavelength of the detector. On the other hand, it is not easy to determine the bandgap of this material: As is typical of most semiconductors, CdTe has a bandgap that decreases with temperature. However, the bandgap energy of HgTe is increases with temperature [16]. Therefore, various empirical expressions have been developed relating the

bandgap energy to the temperature T and the fraction x of cadmium. The most accurate expression relying on data from several different studies is given as [17]

$$E_g = -0.302 + 1.93\,x + 5.35\,(10^{-4})\,T\,(1-2\,x) - 0.810\,x^2 + 0.832\,x^3 \qquad (1.2)$$

Another important advantage of this material is its "intrinsic" behavior. Since the intrinsic energy gap determines the wavelength response, the cooling requirement is not as severe as for extrinsic detectors; because, the absorption of the radiation is due to the bulk material HgCdTe, not the impurities.

1.2.2 Schottky Barrier Infrared Photodetectors

The metal/semiconductor contacts have been studied extensively since they have an important role in microelectronics technology as well as their wide range of practicability to the very large scale integration (VLSI) technology [18,19, and references therein]. If a semiconductor is brought into a physical contact with a metal, a rectifying or an ohmic contact is formed, depending on the type of metal and semiconductor used. The formation of an electronic barrier at the junction is the most important feature of a metal-semiconductor junction. The physical mechanism responsible for this formation has been studied for many years [20,21]. Various models using different physical concepts have been proposed and used [22-25].

In this type of detectors, light is absorbed in the metal/silicide side of the junction and creates a "hot" carrier which passes over the potential barrier; this process is known as internal photoemission (IP). The internal photoemission process is discussed in details in the following chapters.

The variety of metals (or their silicides) can be used to make the Schottky barrier. On condition of using a p-type Si substrate, the most important Schottky junction is made of platinum (Pt → PtSi), which produces a response to ~5.6 μm [26]; other possibilities include palladium (Pd → Pd_2Si) out to ~3.5 μm [26], and iridium (Ir → IrSi) out to ~10 μm [27,28]. All these are of interest primarily because they are suitable for the standard silicon VLSI processing.

1.2.3 Heterojunction Internal Photoemission (HIP) Detectors

The heterojunction internal photoemission (HIP) detector is entirely analogous to the Schottky type detector: The metal or silicide electrode is replaced by degenerately doped another semiconductor material. The idea of Schottky barrier photodiode with a degenerate semiconductor active region is first proposed by Shephard *et al*. [29] and is first demonstrated by Lin *et al*. [30] for SiGe/Si system. HIP detectors offers higher internal quantum efficiency compared to the Schottky barrier detectors. There are two main reasons; (*i*) photons can excite carriers from the states far below the Fermi level such that they do not gain sufficient energy to overcome the barrier in Schottky type detectors. In contrast, narrow band of absorbing states in the SiGe layer of the HIP detector leads to more energetic carriers. (*ii*) Photoexcited holes traveling over the barrier are less likely to be backscattered from the heterojunction interface because of the more favorable ratio of effective masses. However, the absorption coefficient for SiGe is less than that of the silicide or metal due to the lower free carrier density.

1.2.4 Blocked Impurity Band (BIB) Detectors

A blocked impurity band (BIB) detector is an example of the extrinsic detectors. It is first conceived by Petroff and Stapelbroek [31]. The extrinsic Si:As detector was reported with high sensitivity and quantum efficiency in far infrared region (to 28 μm) [32]. The BIB detector resembles the photovoltaic detector in its operation. It has a heavily doped donor band in silicon and an undoped blocking layer is introduced to the structure to prevent dark current from dominating the carriers. The detailed operating principles described by an analytical model for the figure of merit of a BIB detector can be found in [33].

1.2.5 Homojunction Internal Photoemission Detectors

Homojunction internal photoemission detectors are novel detectors for basically very far infrared detection. The basic structure of these detectors consists of a heavily doped layer, which acts as the IR absorber region, and an intrinsic (or lightly doped) layer, across which most of the external bias is dropped. Therefore,

the barrier height depends on the applied bias. The concept of homojunction IR detector was first proposed by Tohyama *et al*. [34] with the cut-off wavelength of 12 μm. Later they reported a silicon homojunction IR detector having an active PtSi layer with extended cut-off wavelength of 30 μm [35]. Various detector approaches (depending on the doping amount) based on Si and GaAs homojunction IP junctions have been discussed by Perera *et al*. [36,37]. They obtained >40μm cut-off wavelength.

1.2.6 Quantum Well Infrared Photodetectors (QWIP)

The concept of light detection by using quantum wells has been studied extensively by many researchers for more than 25 years. The earliest studies were on two dimensional electron systems in metal-oxide-semiconductor inversion layer that has triangular barrier [38, and references therein]. Possibility of using quantum wells with rectangular barrier for infrared detection was first suggested by Esaki and Sakaki [39]. The first experiment on making use of quantum wells for IR detection was reported by Smith *et al*. [40]. Their device operation was based on the absorption of the IR radiation by the free carriers which are trapped in the wells formed by GaAs/AlGaAs heterojunction material systems. Quantum wells are constructed by growing a lower bandgap material (i.e. GaAs) between two larger bandgap materials (i.e. AlGaAs). Therefore, the larger bandgap material serves as a barrier while the small bandgap material serves as a well. When the width of the well is small enough, discrete energy levels are created in the well. Intersubband transition (ISBT) in the wells is the base of modern quantum well infrared detectors. The prediction and the first observation of ISBT in quantum wells was reported by West and Eglash [41]. The first clear demonstration of quantum well infrared photodetectors (QWIPs) was made by Levine *et al*. [42]. Since then tremendous progress has been made on both experimental and theoretical considerations about QWIPs and can be found in the literature [12,43,44].

1.2.7 Quantum Dot Infrared Photodetectors (QDIP)

With the success of quantum well (QW) structures for the infrared detection, the quantum dot infrared photodetector (QDIP) has attracted a lot of interest in recent years. In general, QDIPs are similar to QWIPs but with the quantum wells replaced by quantum dots in which electrons have discrete energy levels created by the three dimensional confinement [45]. Quantum dots used in the detection of infrared radiation are generally formed by the process called Stranski-Krastanov: when the thickness of the film with the larger lattice constant exceeds a certain critical thickness, the compressive strain within the film is relieved by the formation of coherent island. These islands may be quantum dots called self-assembled QDs. Because of this self assembling process, dots show large inhomogeneity both in size and in vertical alignment. Some efforts on size and shape engineering can be found in [46,47 and references therein].

There are several material systems used in QDIP applications. Most widely studied one is InAs dots on GaAs substrate (i.e. InAs/GaAs) [48-50]. Another important material system consists of Ge dots on Si substrate (Ge/Si) [51-53].

1.3 Thermal Detectors

Thermal detectors are made of materials whose physical properties change in the presence of radiant heat. The most common thermal detectors are; (*i*) bolometers, where temperature change produces a change in the resistance of the bulk material; (*ii*) pyroelectric detectors, where temperature change produces a change in the surface charge of the material; and (*iii*) thermocouples, where temperature change produce a change in voltage at the junction of two different solid state materials.

Thermal detectors are important because they offer uncooled operation and cover a large portion of the infrared spectrum. Basically the detector is suspended on lags which are connected to the heat sink. Different from the photon detectors, thermal detectors respond to the intensity of absorbed radiant power without regarding to spectral content. In other words, they respond equally well to all photon

wavelength. Since they work based on the heat flow in the device, heat balance equations are an important consideration when analyzing these devices.

1.3.1 Bolometers

A bolometer is the thermal analogue of a photoconductor. The effect is that of change in resistivity of a material in response to the heating effect of incident radiation. In contrast to photoconductors, bolometers can be made of any material which exhibits temperature dependent change of resistance. The temperature dependence is specified in terms of the temperature coefficient of resistance α defined as [5]

$$\alpha = \frac{1}{R_d}\frac{dR_d}{dT_d} \tag{1.3}$$

where R_d is the detector resistance and T_d is the detector temperature. The electrical circuit requires a voltage source to measure the change in resistance due to the heating effect of the radiation.

1.3.2 Pyroelectric Detectors

Pyroelectric detectors were developed to be worked as a sensitive uncooled detector. They have wide spectral response. Pyroelectric detectors are made from ferroelectric crystals, that is, crystals that can exhibit a permanent electric dipole moment even in the absence of an applied electric field [54]. Lithium tantalite and triglycerine sulfate are the most common detector materials. If the temperature of such material is altered, the electric dipole moment of the crystal must change, leading to the motion of bound charge. If electrodes are placed on the surfaces of the crystal, this motion can induce a current flowing through the external circuit. The magnitude of this current is given by [55]

$$i = p\,A\frac{dT_d}{dt} \tag{1.4}$$

where A is the area of the electrode and p is the pyroelectric coefficient. This process is independent of the wavelength of the radiation and hence pyroelectric sensors have a flat response over a very wide spectral range.

1.3.3 Thermoelectric Detectors

In a circuit consisting of two different conductors and the junctions between them, preferential heating of one junction will generate a voltage which is a measure of temperature difference. When the temperature difference arises from the absorption of radiation at one junction, the device is known a radiation thermocouple. In order to increase the signal voltage, they are connected in series to form a radiation thermopile.

Radiation thermopiles are generally made by subsequent evaporation of metal films such that they are partly overlapped forming a junction. They require no electric bias. They have been found to be useful in spaceborne applications. The preparation and properties of radiation thermopiles can be found in review article [56].

CHAPTER 2

THEORY OF INTERNAL PHOTOEMISSION IN HETEROJUNCTIONS

Internal photoemission is the process in which a carrier is created / excited by an incoming photon, transported to another region and detected as an electric signal. To understand the photon-detection process, the concept of converting a photon of light into an electron must be investigated and for whole process a model must be developed. The efficiency of converting a photon to an electron is defined as quantum efficiency and it takes into account reflectance, absorptance, scattering and electron recombination.

The internal photoemission studies started after R. H. Fowler [57] developed a model describing the response characteristics of the photoemission from metal into vacuum in 1931. According to the theory, photoelectric sensitivity or number of electrons emitted per quantum of light absorbed is proportional to the number of electrons per unit volume of the metal whose kinetic energy normal to the surface augmented by incident photon energy $h\nu$ is sufficient to overcome the potential step at the interface. This is the basic statement for the later studies. In late 1960's internal photoemission in a metal-semiconductor junction was first studied by Cohen *et al.* [58] without taking into account the optical absorptance and the carrier scattering. In this approach, a geometrical analysis was applied to derive the photoyield in the photoemission process. Moreover, several simplifications were assumed to make photoemission model tractable and to drive an equation known as "modified Fowler equation". Then the theory must have been further extended, taking into account multiple reflections of the excited electrons from the surfaces of

the metal film, in addition to collisions with phonons, imperfections, and cold electrons. Vickers [59] and Dalal [60] each developed a ballistic transport model independently in 1971. They showed that the redistribution of momentum by phonon and wall scattering (which can redirect the hot-hole momentum so that it falls in the escape volume) increases the yield. Later, the model was advanced by Mooney and Silverman [61,62] in 1985. They incorporated the "counting loss correction" and "energy loss" terms to the model.

During this period, the idea of utilizing the internal photoemission over a heterojunction barrier for infrared detection was first proposed by Shepherd *et al.* in 1971 [29]. The idea was very attractive since it is possible to control the barrier height and to improve the quantum efficiency. However, the technology was not available at that time to demonstrate the operation of heterojunction infrared detector. It was 1990 that the first $Si_{1-x}Ge_x$/Si heterojunction internal photoemission (HIP) infrared (IR) photodetector was demonstrated by T. L. Lin and J. Maserjian [30]. With the development of molecular beam epitaxy (MBE), several works on heterojunction infrared detectors have been reported [63-66]. A theoretical model for the quantum efficiency of the $Si_{1-x}Ge_x$/Si HIP detector was reported by Tsaur *et al.* [63]. In the model, the internal yield was calculated through the integration of density of states. Nevertheless, it was developed for the region $h\nu > E_F$, and the wavelength dependent absorption was not considered, which made model not applicable for the determination of the optical barrier. This is because the Fermi energies in such structures are usually quite high due to the high doping concentration. The model which includes these aspects was then developed by Lin *et al.* in 1994 [67]. But, neither of these models was including scattering mechanisms that the carriers experienced during their motion. Another model taking into account the scattering of excited carriers was reported by Strong *et al.* [65,68]. In this model, they followed the model which was developed for the metal(silicide)/semiconductor systems by Vickers [59] and incorporated the wavelength and doping concentration dependent absorption. The model comprises several assumptions and needs to be improved.

In this chapter, an extended model, whose contents are similar to that of Mooney's extended model [61], for semiconductor heterojunction internal photoemission detectors is presented. The extensions incorporate the effects on the yield of the difference in the effective masses in the active region and the substrate, nonspherical-nonparabolic bands, and the energy loss per collisions. Before analyzing the effect of the nonspherical-nonparabolic bands on the yield, different equations are derived for the yield for different regions depending on the relative magnitudes of the photon's energy, Fermi level position and the barrier height considering the relation between the magnitudes of the effective masses in both sides of the interface in the next section. In section 2.2 band corrections over the effective mass is discussed. Sections 2.3 – 2.5 present effects of several physical mechanisms such as wall reflection, hot carrier-phonon collision, quantum mechanical reflection, e-p collisions and energy losses. The results of theoretical calculations as a function of different material parameters are presented in section 2.6. Finally in the last section, the model is completed by incorporating the wavelength and doping concentration dependent free carrier absorption to the model.

2.1 Model for Escape Probability

Quantum efficiency (namely external photoyield) can be taken as the product of the absorption of the incident photons and the internal yield which describes the photocurrent generation mechanisms inside the structure after the photons have been absorbed:

$$Y_{ext} = A\,Y_i \tag{2.1}$$

Here A is the optical absorption of the active layer as a function of wavelength and doping concentration, and Y_i is the internal photoyield. We first demonstrate the model describing internal yield.

Fig.2.1 shows the valence band profile and the energy levels for a SiGe/Si HIP structure. For SiGe heterojunction detectors with a degenerately doped SiGe layer,

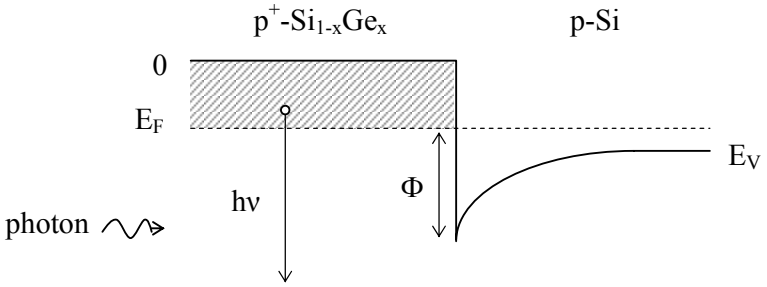

Fig. 2.1 Valence band profile and the energy levels.

holes populate states from the valence band to the Fermi level. When T = 0K all states up to Fermi level is full of carriers and there is no hole above the Fermi level. Note that, energy value of the valence band edge of the SiGe layer has been taken as 0 eV. Excited holes are generated in the active region through the free carrier absorption of photons. Some of these holes reach the SiGe/Si interface, where they can be emitted over the potential barrier created by the valence band offset between strained p^+-$Si_{1-x}Ge_x$ and p-Si. Depending on the relative magnitudes of (hν) and the E_F, distribution of excited holes can be written in momentum space as

$$k(E_F) < k < k(E_F+h\nu), \qquad h\nu < E_F \tag{2.2a}$$

$$k(h\nu) < k < k(E_F+h\nu), \qquad h\nu > E_F \tag{2.2b}$$

Schematic representation of the excited holes' distributions for both $h\nu < E_F$ and $h\nu > E_F$ are shown in Fig.2.2. If the spherical-parabolic band is considered for the holes at the SiGe and the Si layers, the condition for the conservation of total energy is found to be

$$\frac{\hbar^2 k^2}{2m_1} = E_F + \Phi + \frac{\hbar^2 k'^2}{2m_2} \tag{2.3}$$

Here m_1 and m_2 are the effective masses in the SiGe film and the Si substrate respectively, k is the magnitude of the hole's wave vector in SiGe and k' is that of in silicon substrate. Momentum can be divided into two parts; parallel and

perpendicular components with respect to the barrier ($k^2 = k_\perp^2 + k_{//}^2$). Imposing the conditions that the final kinetic energy directed normal to the barrier ($\hbar^2 k_\perp^2 / 2m_1$) must be grater than zero and that the parallel momentum is conserved ($k_{//} = k'_{//}$), one obtains

$$\frac{\hbar^2 k_\perp^2}{2m_1} + \frac{\hbar^2}{2}\left(\frac{1}{m_1} - \frac{1}{m_2}\right) k_{//}^2 \geq E_F + \Phi \tag{2.4}$$

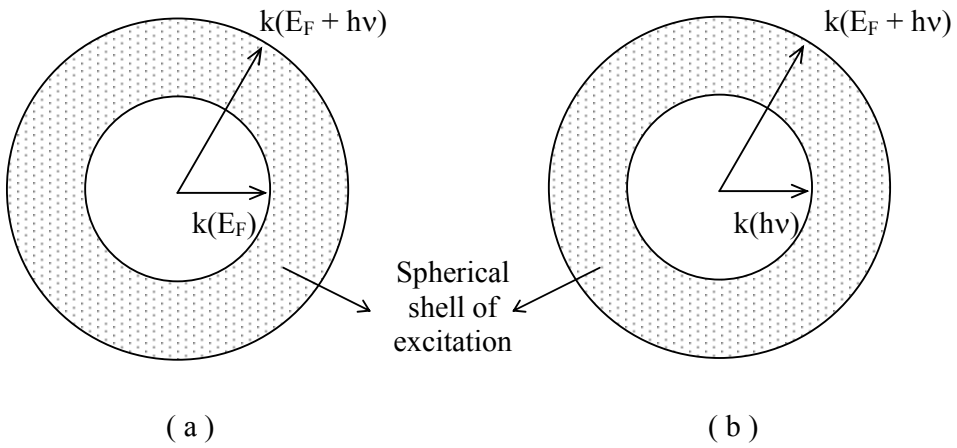

Fig. 2.2 Distribution of holes in momentum space for a spherical Fermi surface at 0 K. a) $h\nu < E_F$, b) $h\nu > E_F$.

For Eq. (2.4), magnitudes of the effective masses determine what kind of equality is satisfied in k-space:

i. *For $m_2 > m_1$*, an ellipsoid satisfies the equality with the equation

$$\frac{k_\perp^2}{a^2} + \frac{k_{//}^2}{b^2} = 1 \tag{2.5}$$

where

$$a^2 = 2m_1\left(E_F + \Phi\right)/\hbar^2 \qquad \text{and} \qquad b^2 = \left(2m_1\left(E_F + \Phi\right)/\hbar^2\right)\left|\frac{m_2}{m_2 - m_1}\right|^{1/2}$$

ii. *For $m_2 = m_1$*, a plane which is parallel to the interface satisfies the equality with the equation

$$\frac{k_\perp^2}{a^2} = 1. \tag{2.6}$$

iii. *For $m_2 < m_1$*, a two-sheeted circular hyperboloid oriented along the $k_\perp$ direction satisfies the equality with the equation

$$\frac{k_\perp^2}{a^2} - \frac{k_{//}^2}{b^2} = 1. \tag{2.7}$$

When the relative magnitudes of a and b compared, it is easy to see that $b > a$. So, the ellipsoid is longer in $k_{//}$-direction than $k_\perp$-direction. At this point, it is necessary to check whether the width of the ellipsoid in $k_{//}$-direction $b > k(E_F + h\nu)$ or not:

$$\left(E_F + \Phi\right)\left|\frac{m_2}{m_2 - m_1}\right| > \left(E_F + h\nu\right) \tag{2.8}$$

It is true especially for the photon energies close to the barrier height (i.e. $h\nu \sim \Phi$) since $\left| m_2 / (m_2 - m_1) \right| > 1$. Fig. 2.3, Fig. 2.4 and Fig. 2.5 show the 3D graphical representation of the carriers in momentum space for $m_2 > m_1$, $m_2 = m_1$, and $m_2 < m_1$, respectively. Note that these were drawn by keeping the effective mass in the Si region constant, $m_2 = 0.6\ m_0$, and changing that of in SiGe region, m_1. Considering Eq. 2.4 and the fact that only states in the spherical shell of excitation are excited, the states which are in between the ellipsoid (or plane, or hyperboloid, depending on the relative magnitudes of the effective masses) and the bigger sphere will emit

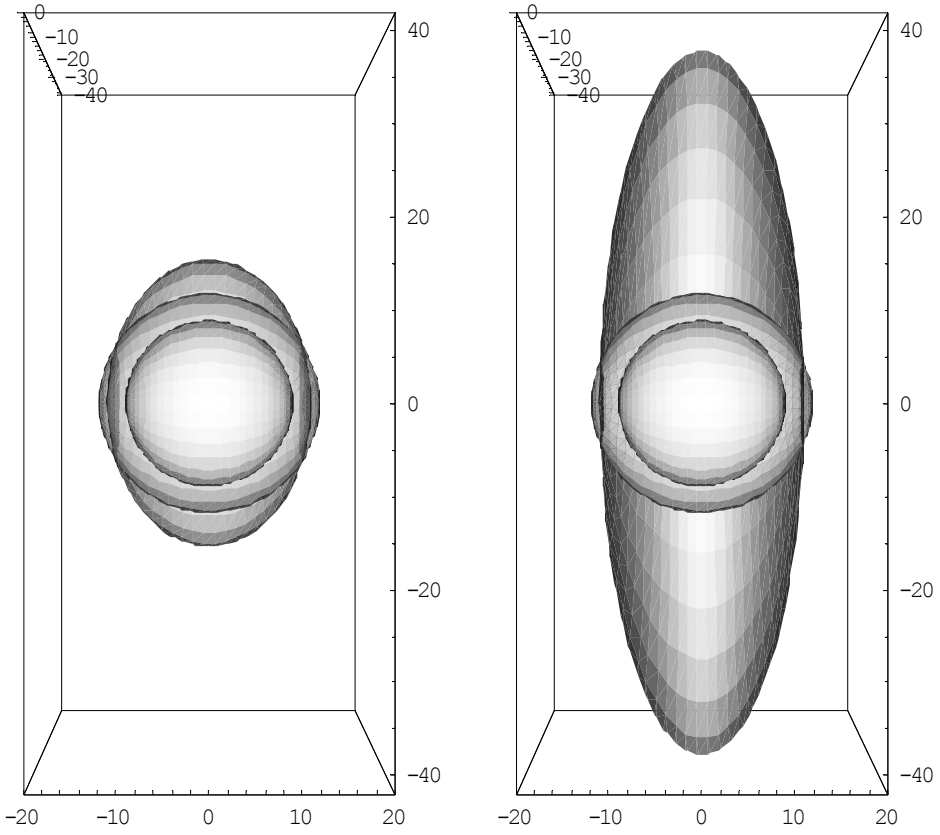

(a) (b)

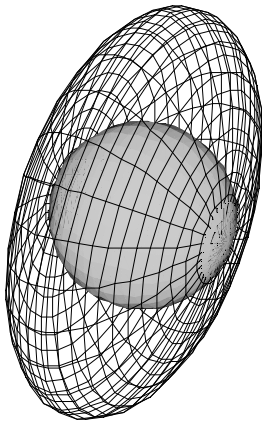

(c)

Fig. 2.3 3D graphical representation of the carriers in momentum space for m_2 (=0.6 m_0) > m_1. a) m_1 = 0.3 m_0, b) m_1 = 0.55 m_0, c) Floating 3D view of the system showing the intersection.

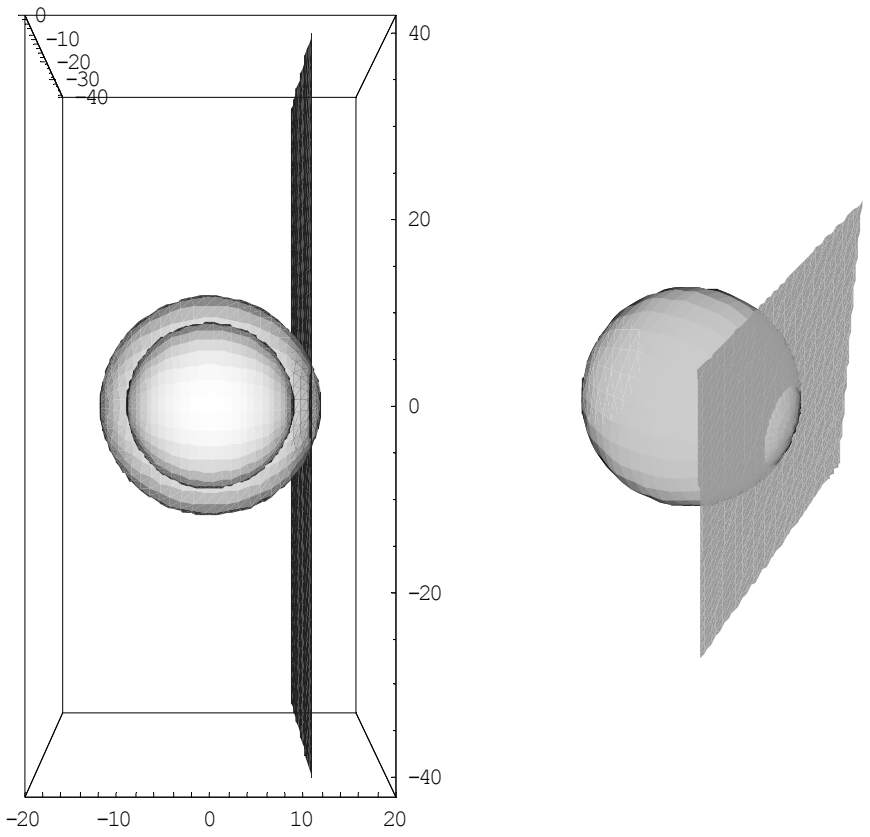

(a) (b)

Fig. 2.4 3D graphical representation of the carriers in momentum space for a) $m_2 = m_1 = 0.6\ m_0$, b) Floating 3D view of the system showing the intersection.

carriers into Si (see Fig. 2.6 for two-dimensional representation). As seen in Fig. 2.3 and Fig. 2.5, when m_1 approaches to m_2 from the left (right), ellipsoid (hyperboloid) gets bigger in $k_{//}$-direction, therefore, the curvature of the ellipsoid (hyperboloid) inside the Fermi sphere reduces. Thus, at first look one would say that since the above-mentioned volume between them will decrease (increase for hyperboloid) when the curvature gets smaller, the yield will increase. Then it can be concluded that, to reach high yield in a HIP, the difference between the effective masses must be as big as possible provided the effective mass of the active region is less than that of substrate. Nevertheless, this inference can only be valid for the constant effective masses. The effect of the effective mass to a HIP's yield will be discussed in the next section.

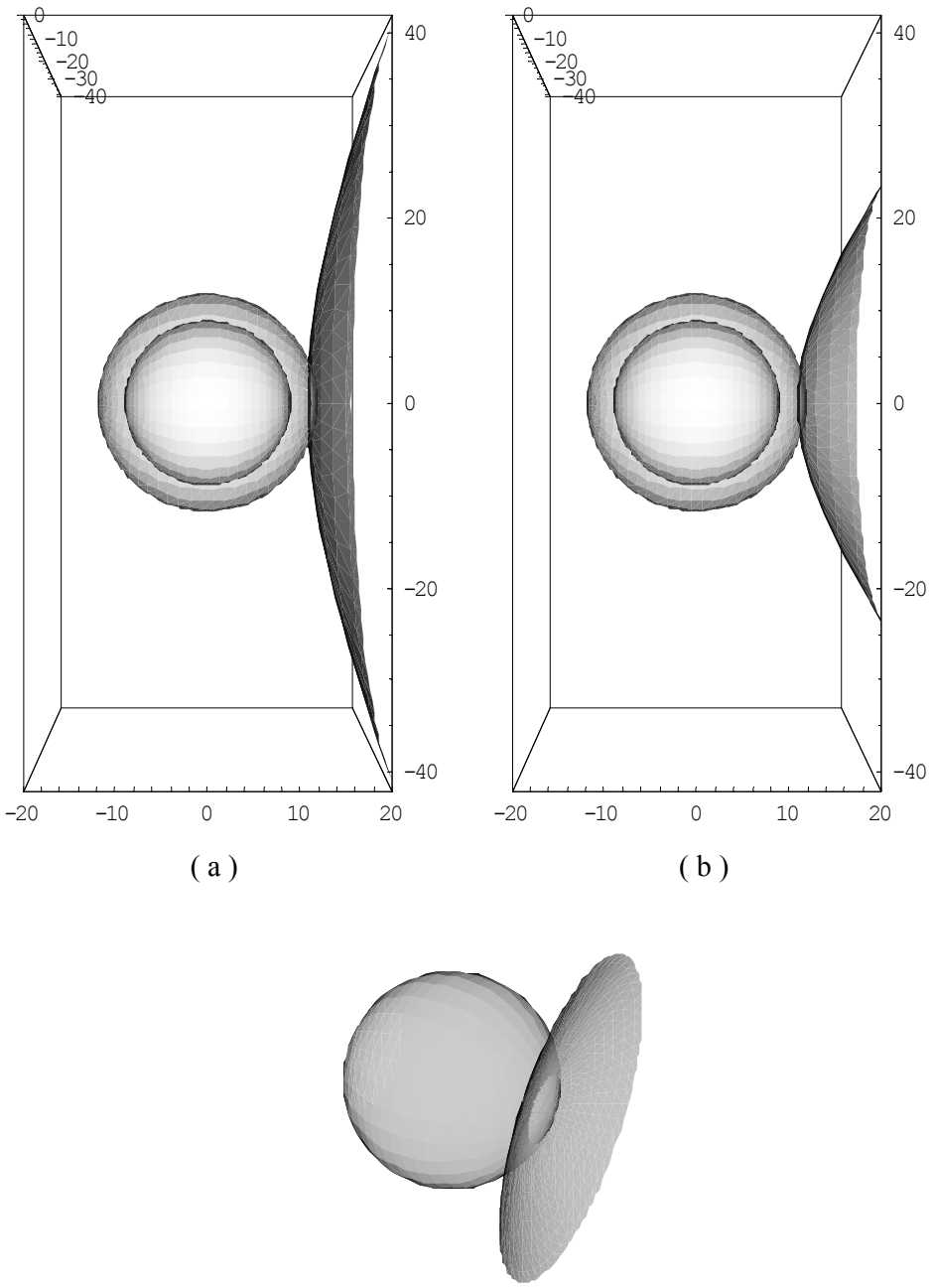

Fig. 2.5 3D graphical representation of the carriers in momentum space for m_2 (=0.6 m_0) < m_1. a) m_1 = 0.7 m_0, b) m_1 = 0.9 m_0, c) Floating 3D view of the system showing the intersection.

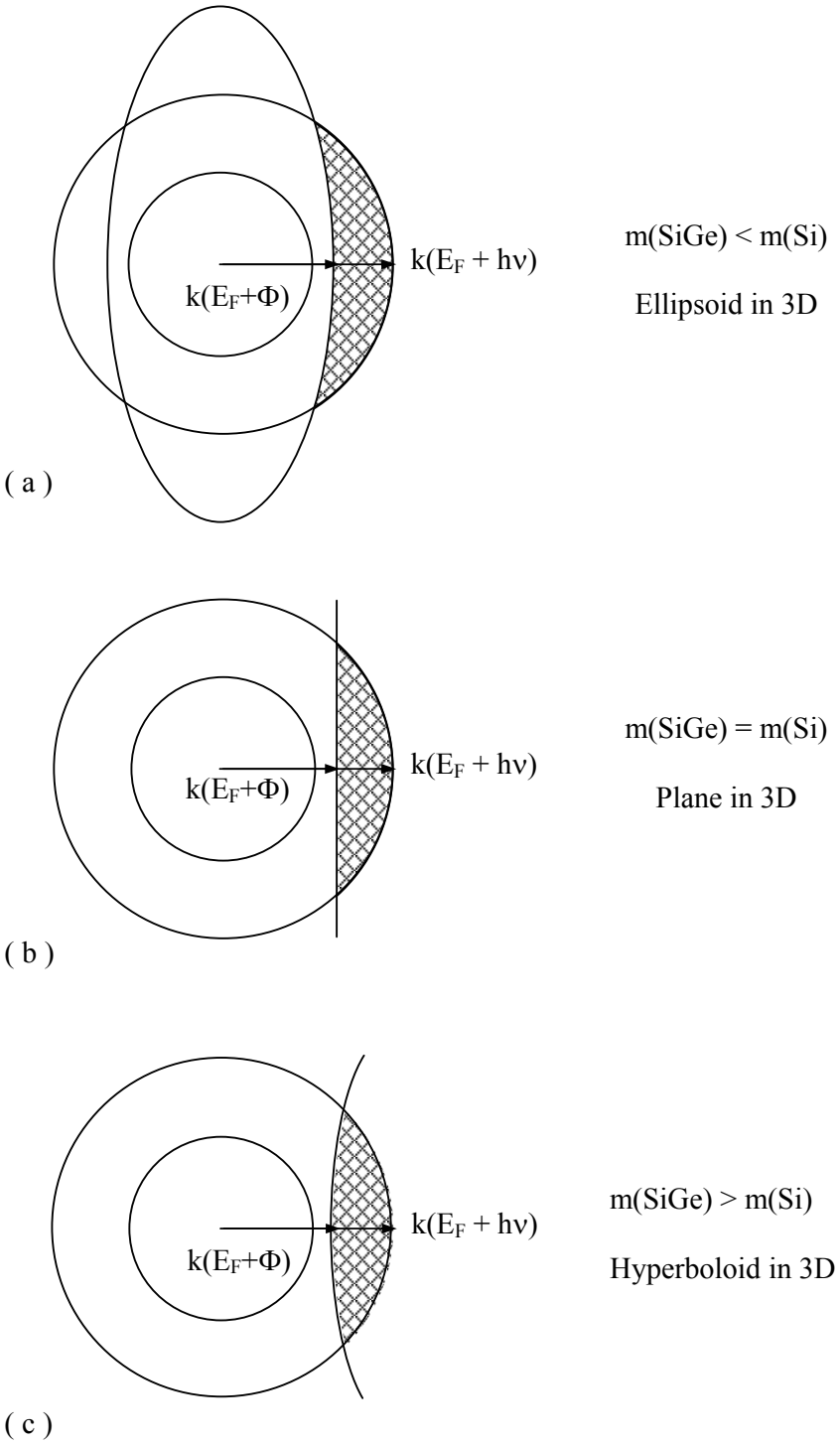

Fig. 2.6 Escape volume for holes in momentum space for three different cases (the hatched region corresponds to the holes that may escape over the barrier). a) m(SiGe) < m(Si), b) m(SiGe) = m(Si), c) m(SiGe) > m(Si).

Hatched region in Fig.2.6 shows the states which will emit. Assuming the density of states is uniform throughout *k*-space, the yield is obtained by dividing the volume of the hatched region by that of the spherical shell of excitation. The volume of the cap is given by

$$V_{hatched} = \int_{\phi=0}^{2\pi} \int_{k=k_{\min}}^{k_{\max}} \int_{\theta=0}^{\theta(k)} k^2 \sin\theta \, d\theta \, dk \, d\phi \tag{2.9}$$

θ(k) is the angle between the momentum vector of the hole and the normal (to the interface) component of it (see Fig.2.7). Using the known equations

$$\sin\theta(k) = \frac{k_{//}}{k} \tag{2.10}$$

$$k^2 = k_{//}^2 + k_{\perp}^2 \tag{2.11}$$

and the help of Eq. (2.4), the volumes can be written as follows for different regions depending on the relative magnitudes of E_F, Φ and $h\nu$:

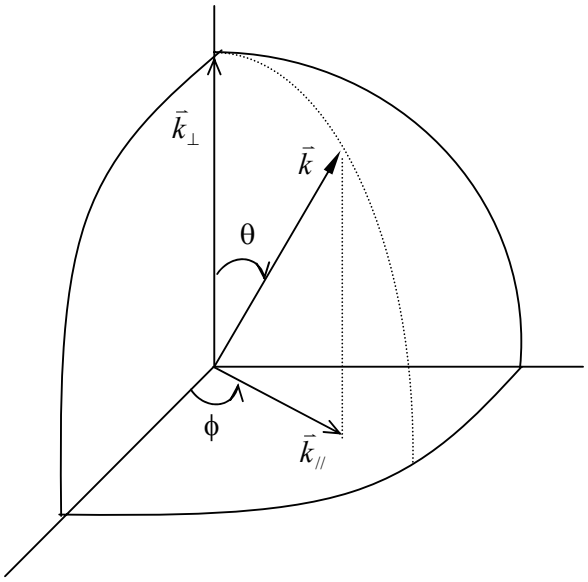

Fig. 2.7 Geometrical definitions of the parameters in momentum space.

Case1: $h\nu < E_F$

$$V_{shell} = \frac{4\pi}{3}\left(\frac{2m_1}{\hbar^2}\right)^{3/2}\left[\left(E_F + h\nu\right)^{3/2} - \left(E_F\right)^{3/2}\right] \tag{2.12}$$

$$k_{\min} = k(E_F + \Phi)$$

$$k_{\max} = k(E_F + h\nu) \tag{2.13}$$

$$V_h = \frac{4\pi}{3}\left(\frac{2m_1}{\hbar^2}\right)^{3/2}\left[\left(E_F + h\nu\right)^{3/2} - \frac{M\left(E_F + \Phi\right)^{3/2}}{M-1} + \frac{\left(E_F - (M-1)h\nu + M\Phi\right)^{3/2}}{M-1}\right] \tag{2.14}$$

where M is the ratio of the effective masses in the Si to that in the SiGe part (i.e. $M = m_2 / m_1$). Then the yield can be written by dividing Eq. (2.14) by Eq. (2.12) as

$$Y_F = \begin{cases} \dfrac{(M-1)\left(E_F + h\nu\right)^{3/2} - M\left(E_F + \Phi\right)^{3/2} + \left[E_F - (M-1)h\nu + M\Phi\right]^{3/2}}{2(M-1)\left[\left(E_F + h\nu\right)^{3/2} - \left(E_F\right)^{3/2}\right]} & M \neq 1 \\ \dfrac{\left(E_F + h\nu\right)^{3/2} - \left(E_F + \Phi\right)^{3/2}}{2\left[\left(E_F + h\nu\right)^{3/2} - \left(E_F\right)^{3/2}\right]} & M = 1 \end{cases} \tag{2.15}$$

Case2: $h\nu > E_F$ *and* $(E_F + \Phi) > h\nu$

$$V_{shell} = \frac{4\pi}{3}\left(\frac{2m_1}{\hbar^2}\right)^{3/2}\left[\left(E_F + h\nu\right)^{3/2} - \left(h\nu\right)^{3/2}\right] \tag{2.16}$$

Since the minimum and the maximum momentum values that define the limits of the hatched region are the same as that are in the Case1, V_h is the same as well (i.e. Eq. (2.14)). Therefore, with the same approach, yield can be written as

$$Y_F = \begin{cases} \dfrac{(M-1)\left(E_F + h\nu\right)^{3/2} - M\left(E_F + \Phi\right)^{3/2} + \left[E_F - (M-1)h\nu + M\Phi\right]^{3/2}}{2(M-1)\left[\left(E_F + h\nu\right)^{3/2} - \left(h\nu\right)^{3/2}\right]} & M \neq 1 \\ \dfrac{\left(E_F + h\nu\right)^{3/2} - \left(E_F + \Phi\right)^{3/2}}{2\left[\left(E_F + h\nu\right)^{3/2} - \left(h\nu\right)^{3/2}\right]} & M = 1 \end{cases} \tag{2.17}$$

<u>*Case3:*</u> $h\nu > E_F$ *and* $(E_F + \Phi) < h\nu$

For this region, V_{shell} is the same as that in Case2, however, the k_{min} is different;

$$k_{\min} = k(E_F + \Phi)$$

$$k_{\max} = k(E_F + h\nu) \tag{2.18}$$

Therefore,

$$V_h = \frac{4\pi}{3}\left(\frac{2m_1}{\hbar^2}\right)^{3/2}\left[\left(E_F + h\nu\right)^{3/2} - (h\nu)^{3/2} + \frac{\left(E_F - (M-1)h\nu + M\Phi\right)^{3/2}}{M-1} + \frac{\left(E_F - (M-1)h\nu + M\Phi\right)^{3/2}}{M-1}\right] \tag{2.19}$$

Then the yield,

$$Y_F = \begin{cases} \dfrac{1}{2} + \dfrac{\left[E_F - (M-1)h\nu + M\Phi\right]^{3/2} - \left[ME_F - (M-1)h\nu + M\Phi\right]^{3/2}}{2(M-1)\left[\left(E_F + h\nu\right)^{3/2} - \left(h\nu\right)^{3/2}\right]} & M \neq 1 \\ \dfrac{1}{2} & M = 1 \end{cases} \tag{2.20}$$

2.2 Band Correction over Effective Mass

While developing the model above, the spherical-parabolic band was considered for the holes at the SiGe and the Si layers: The density of states (DOS) at energy E is then given by

$$N(E)dE = \frac{1}{2\pi^2}\left(\frac{2m^*}{\hbar^2}\right)^{3/2} E^{1/2}dE \tag{2.21}$$

where $\hbar^2$ is Planck's constant divided by 2π and m^* is the constant effective mass found from the curvature of the band $E(k) = \hbar^2 k^2 / 2m^*$.

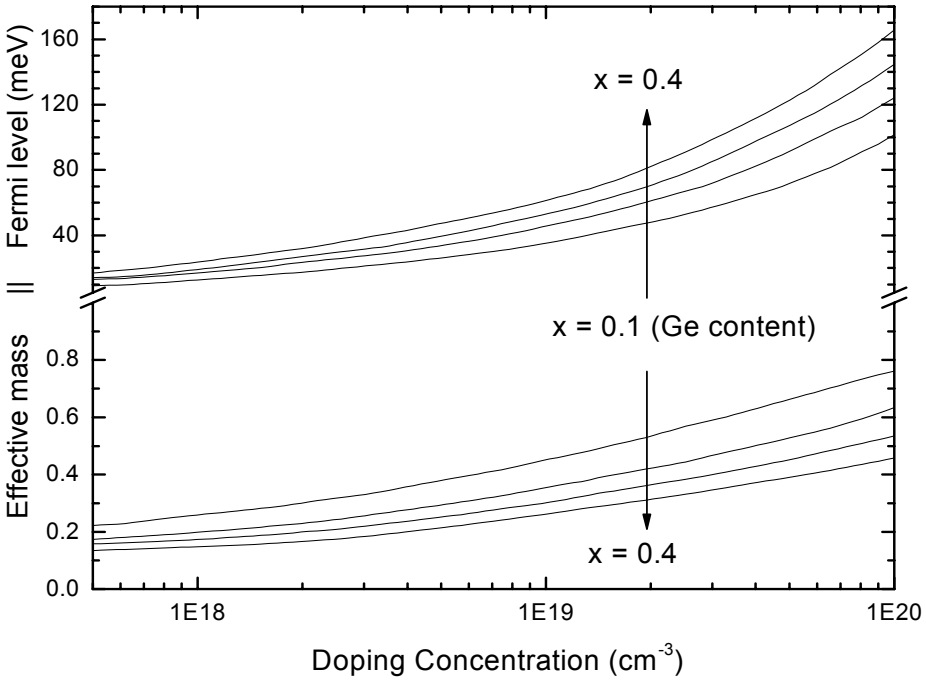

Fig. 2.8 Calculated effective mass and Fermi energy versus doping concentration graph for different x values at 4 K (from reference [69]).

For nonspherical-nonparabolic bands, Eq. (2.21) is still valid provided m^* is not a constant but a function of energy, $m(E)$. These energy dependent carrier concentration effective masses were calculated for heavily p-type doped Si and strained $Si_{1-x}Ge_x$ layers by Y. Fu *et al.* [69]. Fig. 2.8 shows the calculated effective

mass and Fermi energy values vs doping concentration graph for different Ge contents at 4K (from [69]). If the energy dependent effective mass is considered, as *m(E)* changes, not only the curvature but also the boundaries defining the escape volume changes (see Fig.2.2 and Fig. 2.6).

Analysis:

As discussed above for energy independent effective masses, yield increases when m_1 (the effective mass of the active region) decreases by keeping the effective mass of the substrate, m_2, constant (i.e. $M = m_2 / m_1$ in Eq. (2.15), (2.17) and (2.20) increases). Fig. 2.9 and Fig. 2.10 show the calculated yield versus photon energy graphs for different *M* values, and yield versus effective masses ratio *M* for different photon energies, respectively. During the calculations, Fermi energy and the barrier height have been taken as 80 meV and 40 meV, respectively. As expected from the energy independent effective mass approach, the yield increases both with increasing *M* and photon's energy.

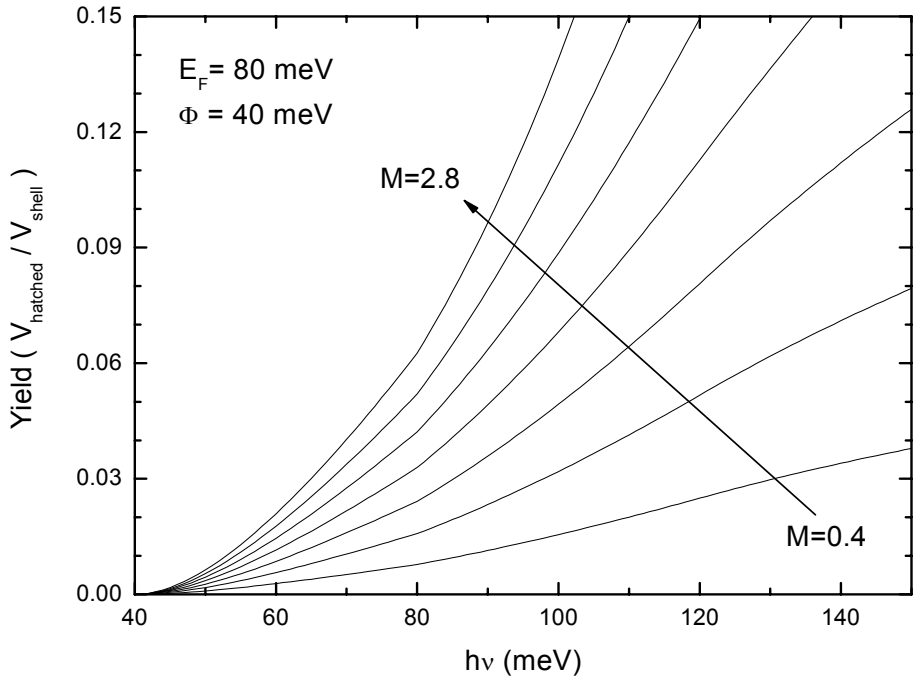

Fig 2.9 Calculated yields versus photon energy graph for different *M* values when the constant effective mass is considered.

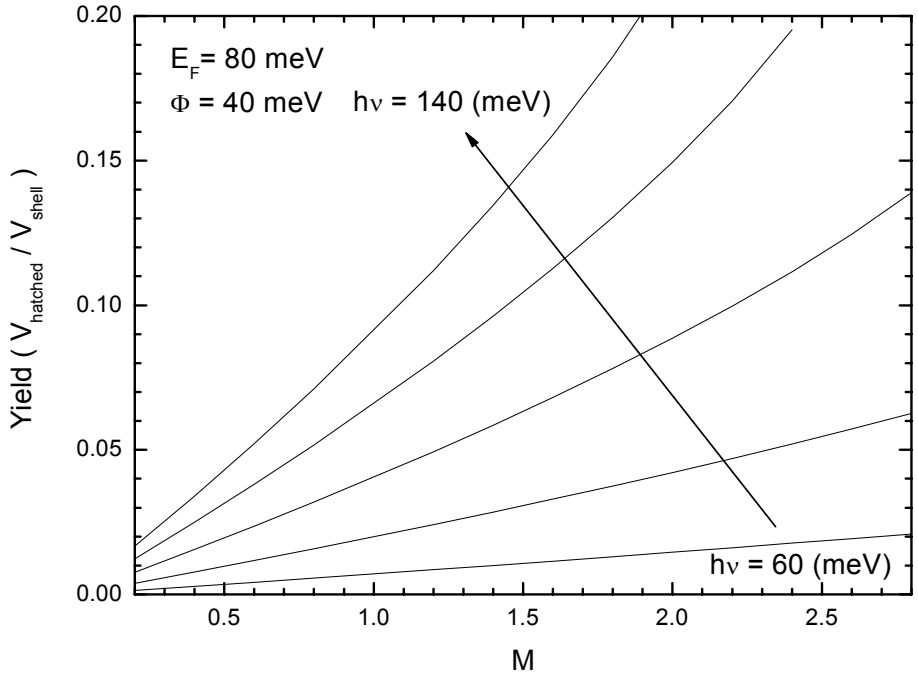

Fig 2.10 Calculated yields versus effective masses ratio *M* for different photon energies when the constant effective mass is considered.

In the case of constant structural parameters (except m_1), when the effective mass of the carriers reduces, i.e. *M* gets bigger, their resistance to the movement in the structure reduces as well. Thus, they can move more easily after excitation and this increases the yield. This concept would be clearer when the scattering mechanisms is investigated. On the other hand, when the energy dependent effective mass is considered, yield does not increase monotonically as seen in Fig. 2.11 and Fig. 2.12. If the valence band discontinuity, $E_F+\Phi$, is assumed to be depended only on the Ge content in the $Si_{1-x}Ge_x$ layer, yield decreases with decreasing m_1. Since the Fermi level decreases with m_1 (see Fig. 2.8), the effective barrier that must be passed by the excited carriers increases. This is especially dominant for the low energy region of the spectrum. Therefore, we can say that increase in *M* has two opposite impacts on the yield, which are effective in different regions of the spectrum and this is the reason for the crossover in Fig.2.11.

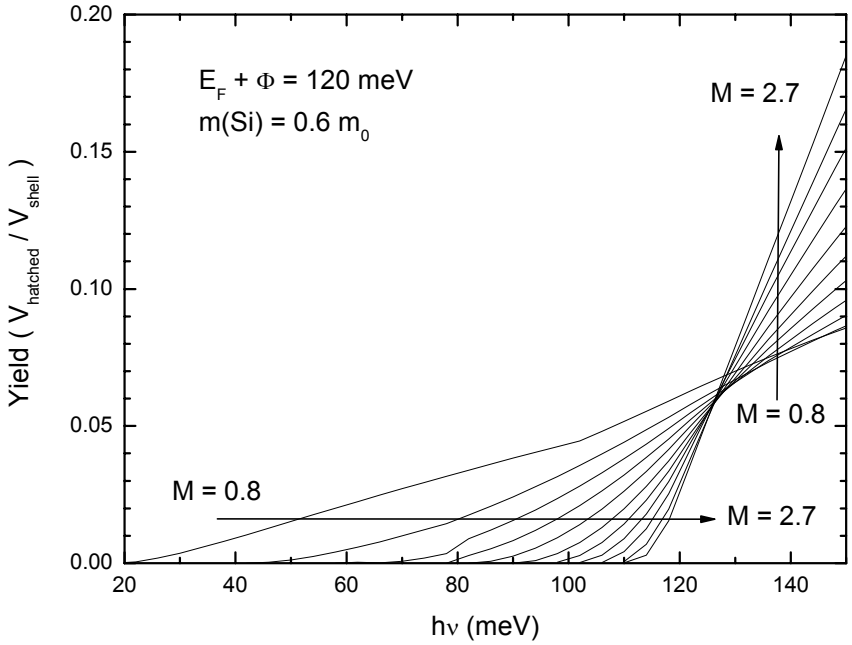

Fig. 2.11 Calculated yields versus photon energy graph for different *M* values when the energy dependent effective mass is considered.

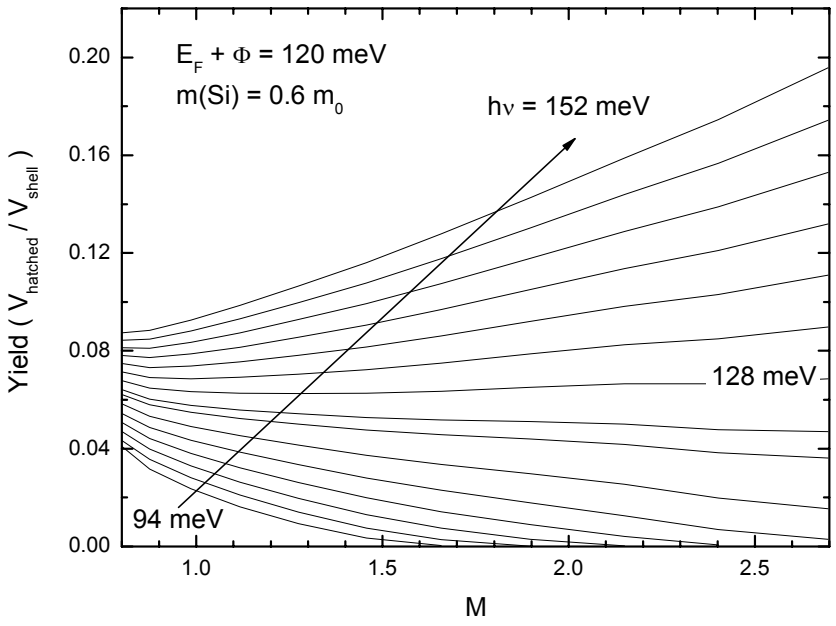

Fig. 2.12 Calculated yields versus effective masses ratio *M* for different photon energies when the energy dependent effective mass is considered.

Fig. 2.13a shows the 3-dimensional representation of the variation of the yield with respect to the effective masses ratio and the energy of the incident photons. The projections of the 3D surface on each plane are presented in Fig. 2.13b in the shaded form.

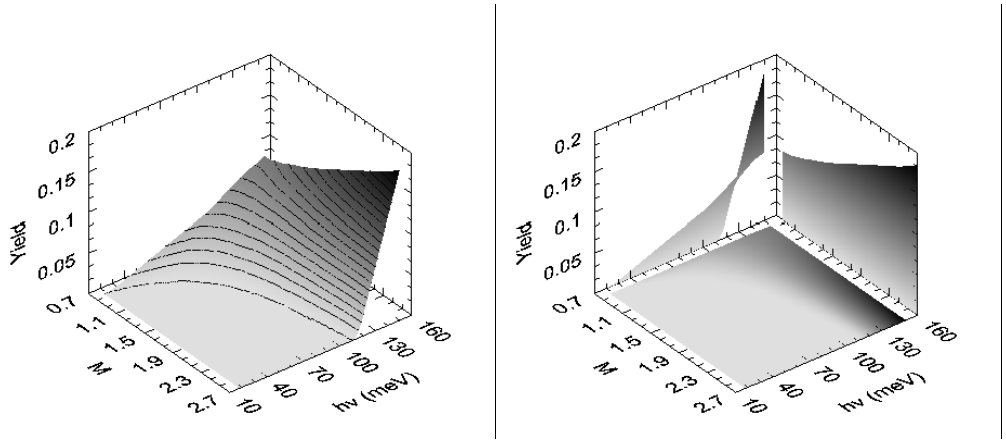

(a) (b)

Fig. 2.13 a) 3-dimensional representation of the variation of the yield with respect to the effective masses ratio and the energy of the incident photons. b) The projections of the 3D surface on each plane in the shaded form.

The effect of different substrate (Si in this case) effective masses on the yield is shown in Fig. 2.14. As seen in the figure, increase in the Si layer's effective mass causes increase in the yield as well.

2.3 Effects of Multiple Reflections and Scattering

Up to this section, we have calculated the escape probability (i.e. yield) for holes that experience no scattering events between excitation and reaching the interface. However, scattering affects the escape probability by redistributing the momentum of the excited carriers: multiple reflections of the excited holes from the surfaces of the active region as well as the collisions with phonons, imperfections and cold electrons can either increase the yield by directing carriers into the escape volume or decrease the yield by directing carriers out of the escape volume.

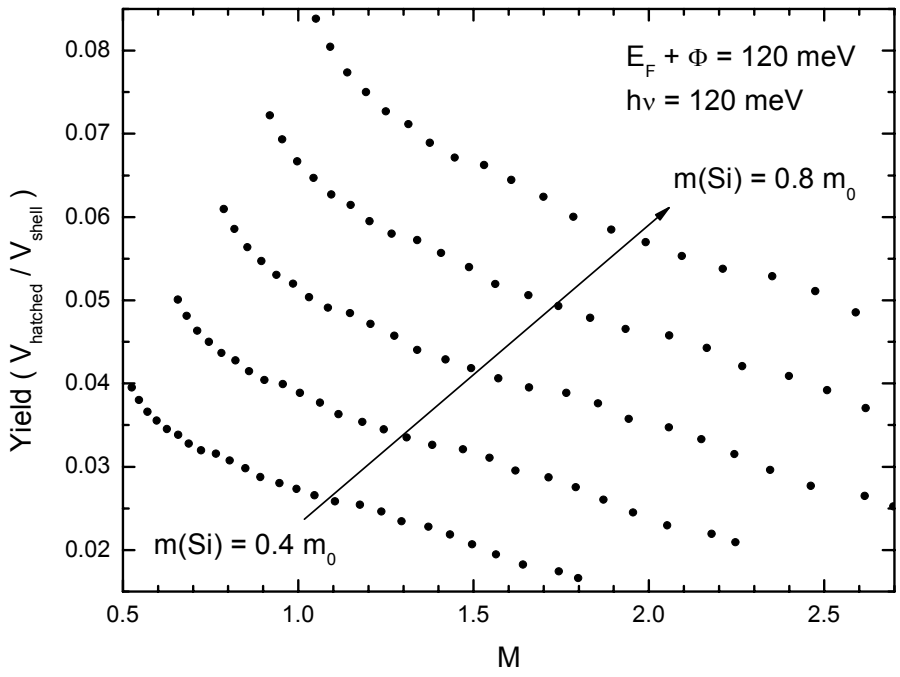

Fig. 2.14 The effect of different substrate (Si in this case) effective masses on the yield.

The scattering mechanism in such a structure junctions can be investigated in three groups:

1. *Interface scatter*: (Elastic scattering) This occurs when a hot-hole interacts with the walls of the active region (e.g. air/SiGe and SiGe/Si interfaces for Fig. 2.1) and is not emitted.

2. *Hot-hole / cold-electron scatter*: (Inelastic scattering) This mechanism is characterized by a mean free path L_e and the energy loss in such an event will be so great that the hot-hole can no longer get over the barrier.

3. *Hot-hole / phonon scatter*: (Semi-elastic scattering) This mechanism is characterized by a mean free path L_p and except for collisions with cold-electrons, all other bulk collisions such as collisions with phonons, grain boundaries, lattice defects etc. are in this group with the mean energy loss $\hbar\omega$.

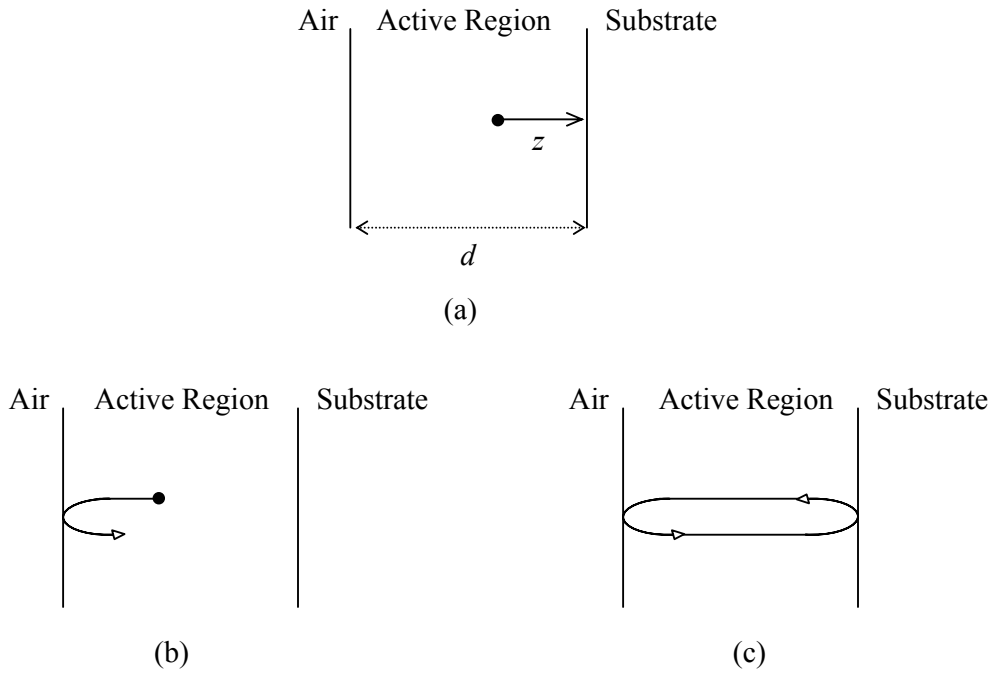

Fig. 2.15 Schematic diagram showing the different processes during the motion of an excited carrier before emission.

The probability of reaching the barrier without colliding in the bulk for a hole created at a distance *z* from the barrier is in the form *exp(-z/L)*. *L* is related to the specific scattering parameter of a hot carrier with cold electrons, phonons etc. Thus, the accumulated probability for escape without scatter for an excited hole, which is initially in the escape cap, can be found as (Fig.2.15-a)

$$\alpha = \frac{1}{d}\int_0^d e^{-z/L_e}\, e^{-z/L_p}\, dz$$

$$\alpha = \frac{1}{d}\int_0^d e^{-z/L^*}\, dz \qquad (2.22)$$

Notice that (*1/d*) term comes from the normalization where *d* is the thickness of the film. In addition to this, uniform absorption is assumed. For small photon energies, all states in the escape volume have momentum directed approximately normal to the barrier, and therefore, Eq. (2.22) can be written as $\alpha = \left(1 - e^{-d/L^*}\right) L^* / d$.

However, for higher photon energies, the momentum component of the excited carrier parallel to the interface increases the distance that the carrier must travel before reaching the interface, and *d* in Eq. (2.22) must be replaced with *d/cos(θ)*. For an excited hole, the probability of escape without being scattered can then be written as

$$\alpha = \frac{1}{d}\int_0^d \int_0^{\pi/2} \exp(-z/L*\cos\theta)\sin\theta\, d\theta\, dz \qquad (2.23)$$

If the holes are not initially in the escape cap, the accumulated probability of reaching one of the interfaces is given by (Fig.2.15-b)

$$\beta = \frac{1}{d}\int_0^d \int_0^{\pi/2} \exp(-(d-z)/L*\cos\theta)\sin\theta\, d\theta\, dz \qquad (2.23)$$

For multiple reflections, one can similarly calculate the probability δ that a hole, which is diffusely scattered off one surface, reaches the other surface without any collision as (Fig.2.15-c)

$$\delta = \int_0^{\pi/2} \exp(-d/L*\cos\theta)\sin\theta\, d\theta \qquad (2.24)$$

And now it is easy to calculate the total accumulated probability that a hot-hole will be emitted without colliding in the bulk. The probability that a hot-hole reaches the barrier prior to any collision in the bulk (Y_0) contains infinite number of terms including the effects of multiple scatters off the interfaces. For example,

$$Y_F \cdot \alpha \qquad (2.25)$$

is the probability that a hot-hole is initially in the escape cap and that it is able to reach the barrier (see Fig.2.15-a).

$$Y_F\, \beta\, e^{-d/L*} \qquad (2.26)$$

corresponds the probability that the hot-hole is initially directed toward the air/active region interface, is scattered into escape cap at the interface and is able to reach the barrier (see Fig.2.15-b).

If η is the probability that a hot-hole is not initially in the escape cap then the capture probability of it which has two scatters at the interfaces with the term considering hole which was initially directed toward the junction can be written as

$$Y_F\ \eta\beta\ \delta\ e^{-d/L^*} \tag{2.27}$$

And if this hole is initially directed to the back interface then probability becomes

$$Y_F\ \eta\beta\ \delta^2\ e^{-d/L^*} \tag{2.28}$$

In this way infinite number of terms can be written and consequently the sum of these terms (that is Eq. (2.37-40)) will give

$$Y_{i0} = Y_F\alpha + Y_F\beta e^{-d/L^*}\left(1+\eta\delta+\eta\delta^2+\eta^2\delta^3+\eta^2\delta^4+\cdots\right) \tag{2.29}$$

The term η may also be viewed as a counting loss correction term reflecting the number of times the carrier is scattered back from the barrier before ultimate capture and be written as

$$\eta = \left(1-\frac{2Y_F}{Y_\infty}\right) \tag{2.30}$$

Where Y_∞, the maximum quantum yield, is given by the volume ratio of the spherical shell (not hatched volume in Fig. 2.6) of potentially capturable holes to the shell of excitation (see Fig.2.16).

$$Y_\infty = \frac{V_{shell\ of\ emission}}{V_{shell\ of\ excitation}} = \begin{cases} \dfrac{(E_F + h\nu)^{3/2} - (E_F + \Phi)^{3/2}}{(E_F + h\nu)^{3/2} - {E_F}^{3/2}} & case1 \\ \dfrac{(E_F + h\nu)^{3/2} - (E_F + \Phi)^{3/2}}{(E_F + h\nu)^{3/2} - (h\nu)^{3/2}} & case2 \\ 1 & case3 \end{cases} \tag{2.31}$$

Notice that the yield and hence this probability has been normalized since only a portion of the excited states can potentially emit, and the population of the states which can emit is depleted, while that of the non-emitting states remains statistically unchanged.

Substituting Eq. (2.30) to (2.29) and simplifying it, Eq. (2.29) can be reduced to

$$Y_{i0} = Y_F \left[\alpha + \beta e^{-d/L^*} \frac{1 + (1 - 2Y_F / Y_\infty)\delta}{1 - (1 - 2Y_F / Y_\infty)\delta^2} \right] \tag{2.32}$$

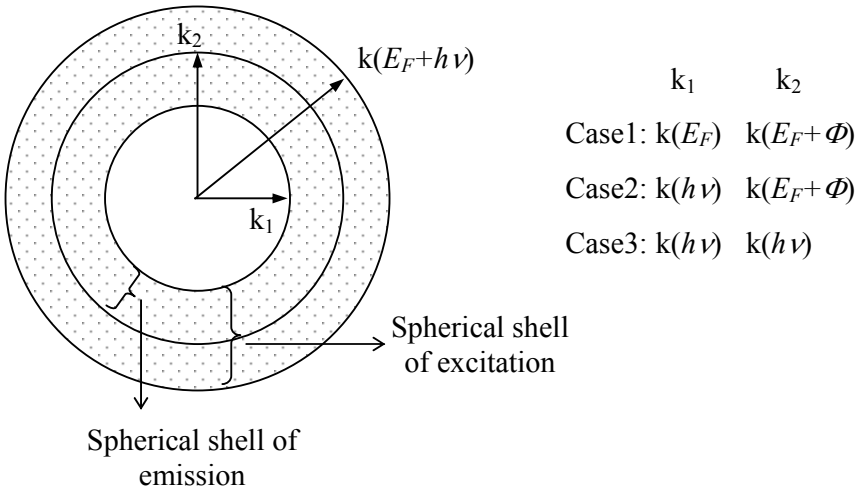

Fig. 2.16 Diagram illustrating the definition of the spherical shell of emission.

2.4 Quantum Mechanical Effects

After the hot-hole reaches the barrier there is a finite probability that it will be reflected at the barrier even though it is in the escape volume. If the probability that a hot-hole in the escape volume is transmitted across the barrier is τ, then the total yield for no collisions in the bulk is given by [62]

$$Y_0 = Y_{i0}\tau\Big\{1+\big[\ (1-\tau)\delta(1-\eta)e^{-d/L^*}\left(1+\eta\delta^2+\eta^2\delta^2+\cdots\right)\ \big]$$

$$+\Big[(1-\tau)\delta(1-\eta)e^{-d/L^*}\left(1+\eta\delta^2+\eta^2\delta^2+\cdots\right)\Big]^2+\big[\quad\big]^3+\cdots\Big\}$$

$$=\frac{Y_{i0}\tau}{1-\dfrac{(1-\tau)\delta(1-\eta)e^{-d/L^*}}{1-\eta\delta^2}} \tag{2.33}$$

The first term of the above equation (i.e. $Y_{i0}\tau$) generates the probability of emission without a quantum-mechanical reflection at the interface. The other terms comes from the probability of the possible future scenarios of the subset of hot-holes which approach the barrier with the requisite escape condition, i.e. would be captured in the classical model, but were quantum-mechanically reflected away from the interface uniformly in all directions.

2.5 Effect of e-p Collisions and Energy Losses

In the above sections, contributions of the scattering mechanisms to the yield have been taken into account, however, that of the phonon collisions and hence energy losses have not been incorporated. When this is done, the yield is viewed as a sum of partial yields, where the n^{th} partial yield represents the yield of the hot-holes that have suffered n phonon collisions. This means that hot-holes are divided into groups distinguished from each other by the number of phonon collisions. In terms of the geometry (see Fig.2.16), as the carriers lose energy, the spherical shell of excitation shrinks from outside to in for case1. Additionally, the inner sphere gets smaller as well for other cases but since the effect of the reduction in $h\nu$ to the

volume of the excitation shell is more prominent than that, the shell of excitation shrinks.

And now, it is necessary to find the probability γ that a hole will collide with a phonon before it collides with a cold-electron because this process leaves a hot-hole unable to overcome the barrier. The fraction γ can be calculated as follows:

The fraction undergoing a phonon collision over a path length *dz*, having traveled a total path length z, would be

$$e^{-z/L^*}\frac{dz}{L_p} \tag{2.34}$$

of these, only $exp(-z/L_e)$ would not have collided on the way with a cold electron and been removed from the process. Thus, one finds

$$\gamma = \int_0^\infty e^{-z/L_p}\, e^{-z/Le}\frac{dz}{L_p} = \frac{L_e}{L_e + L_p} \tag{2.35}$$

At this point, the yield including contribution of successive phonon distributions can be found by combining Eq. (2.31-33), and (2.35);

$$Y = Y_0 + \left(1 - \frac{Y_0}{Y_\infty}\right)\gamma Y_1 + \left(1 - \frac{Y_0}{Y_\infty}\right)\left(1 - \frac{Y_1}{Y_\infty}\right)\gamma^2 Y_2 + \cdots \tag{2.36}$$

where the effects of holes which have been emitted on previous distribution are appeared in terms like $(1-Y_n/Y_\infty)$. And Y_n (appropriate for the n^{th} phonon distribution) is the generalization of Eq. (2.33).

One can find Y_n by upgrading the Eq. (2.15), (2.17) and (2.20) for all three cases; if $n\hbar\omega$ is the energy loss for n^{th} phonon distribution, ($h\nu - n\hbar\omega$) is used instead of $h\nu$ in the numerator of these equations because the numerator corresponds to the escape volume. Thus Y_{Fn} can be found for $M \neq 1$

$$Y_{Fn}=\begin{cases}\dfrac{(M-1)\left(E_F+h\nu-n\hbar\omega\right)^{3/2}-M\left(E_F+\Phi\right)^{3/2}+\left[E_F-(M-1)(h\nu-n\hbar\omega)+M\Phi\right]^{3/2}}{2(M-1)\left[\left(E_F+h\nu\right)^{3/2}-\left(E_F\right)^{3/2}\right]} & case1\\ \dfrac{(M-1)\left(E_F+h\nu-n\hbar\omega\right)^{3/2}-M\left(E_F+\Phi\right)^{3/2}+\left[E_F-(M-1)(h\nu-n\hbar\omega)+M\Phi\right]^{3/2}}{2(M-1)\left[\left(E_F+h\nu\right)^{3/2}-\left(h\nu\right)^{3/2}\right]} & case2\\ \dfrac{1}{2}+\dfrac{\left[E_F-(M-1)(h\nu-n\hbar\omega)+M\Phi\right]^{3/2}-\left[ME_F-(M-1)(h\nu-n\hbar\omega)+M\Phi\right]^{3/2}}{2(M-1)\left[\left(E_F+h\nu\right)^{3/2}-\left(h\nu\right)^{3/2}\right]} & case3\end{cases}$$

(2.37a)

and for $M = 1$,

$$Y_{Fn}=\begin{cases}\dfrac{\left(E_F+h\nu-n\hbar\omega\right)^{3/2}-\left(E_F+\Phi\right)^{3/2}}{2\left[\left(E_F+h\nu\right)^{3/2}-\left(E_F\right)^{3/2}\right]} & case1\\ \dfrac{\left(E_F+h\nu-n\hbar\omega\right)^{3/2}-\left(E_F+\Phi\right)^{3/2}}{2\left[\left(E_F+h\nu\right)^{3/2}-\left(h\nu\right)^{3/2}\right]} & case2\\ \dfrac{1}{2} & case3\end{cases}$$

(2.37b)

Eq. (2.37) and/or (2.38) can then be used in Eq. (2.33) to generate ultimate yield Y_n.

The series is truncated when "thermalization" occurs, i.e.

$$n_{\max}=\frac{h\nu-\Phi}{h\nu} \tag{2.38}$$

2.6 Analysis: Effects of the Scattering Parameters on the Yield

In this section the results of the model developed above will be given by a series of graphs. For the calculations, all equations have been used as in the original form presented in the thesis; no approximations have been made except that the quantum mechanical transmission probability was taken to be $\tau = 1$. It can also be noted that since the model presented here does not include the temperature dependence, it can be thought that the device is operated at 0 K. In fact, for the model developed for the PtSi/Si Schottky type infrared photodetectors, we had the conclusion that the internal photoemission is expected to be almost temperature independent [70]. Unless otherwise stated, $\Phi = 40$ meV, $E_F = 80$ meV, $m_1 = 0.751\ m_0$ (corresponding to the Fermi level used, from reference [69]), and $m_2 = 0.522\ m_0$ have been used in the calculations. These values are close to the ones for a p-type highly doped SiGe/Si HIP operating for the mid-infrared region.

Fig. 2.17 shows the yield calculated from the Eq. (2.36) for different layer thicknesses with the following parameters: L_p = 50 Å, L_e = 1000 Å and $\hbar\omega$ = 1 meV. Note that it is hard to estimate and/or measure these parameters; the ones used here are within the ranges suggested by Mooney and Silverman [61,62] for Schottky IR technology ($L_p \approx$ 50-150 Å, $L_e \approx$ 500-5000 Å and $\hbar\omega \approx$ 1-10 meV). Strong *et al.* [65] used similar values for L_e and L_p for their SiGe/Si detectors; they extracted the elastic scattering length L_p of 10 Å from the relaxation time measurements in heavily doped material.

The upward curvature of the theoretical curves for low photon energies in the graph can be explained as follows: As the energy of the incident photon increases, the hot-hole can survive for more phonon collisions and have more chance to be redirected to the escape volume. But for higher photon energies, since the elimination of the previously emitted carriers becomes pronounced, the curves start to roll off from the linearity. So, one can say that this is more significant for the lower energy loss term (see Fig. 2.20 as well). Since the yield around the barrier height is quite small, in Fig. 2.17 the cut-off energy of the system looks like 50 meV although it is 40 meV. If the graph had been plotted in logarithmic scale, it would be seen that the cut-off

energy is what it should be. The effect of the film thickness can also be seen in Fig. 2.17. Decrease in the thickness of the active region causes an increase in the number of wall scattering and hence hot-holes are redirected to the escape volume. Therefore, the yield increases.

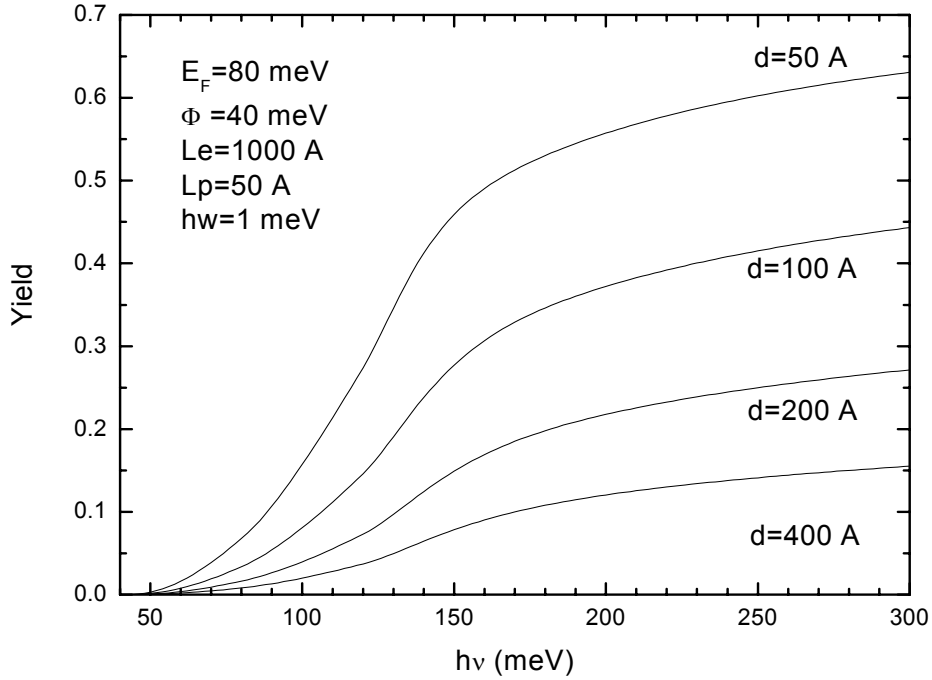

Fig. 2.17 Effect of the film thicknesses on the yield versus energy plots.

Fig. 2.18a and 2.18b show the effects of the different L_p values on the yield for $\hbar\omega$ = 1 meV and $\hbar\omega$ = 10 meV respectively. As seen here, the effect of the variation in the mean free path for semi-elastic collisions depends on the excitation energy, film thickness, and the energy loss value per collision. For low excitation energies, few phonon collisions suffice to thermalize the carrier, so shorter L_p values lead to lower yield. This effect is more pronounced for high energy loss case (Fig. 2.18b). On the other hand, at high excitation energies, the hot-hole is less easily thermalized and more probably redirected into the escape direction and hence phonon scattering tends to increase the yield for the small energy loss case (Fig. 2.18a).

In Fig. 2.19 L_e dependence of the yield is demonstrated. For a hot-hole, small mean free path of elastic collisions means high probability of collision with a cold-electron.

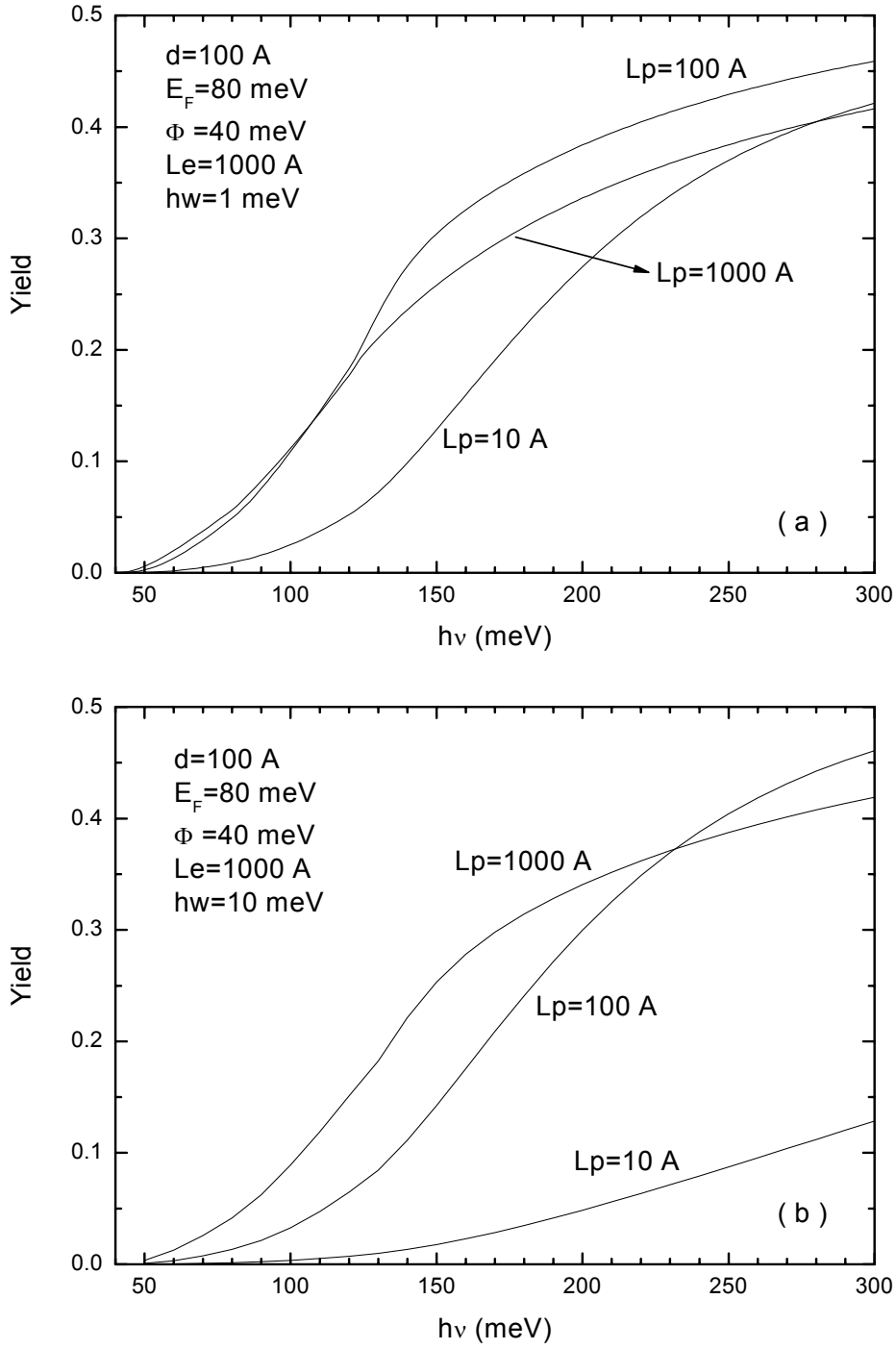

Fig. 2.18 Yield versus energy plots for several hot-hole/phonon scattering mean free paths (L_p) with an energy loss per collision ($\hbar\omega$) of a) 1 meV, and b) 10 meV.

Therefore, due to the fact that energy loss in hot-hole/cold-electron scattering is very big, the hot-hole can no longer get over the barrier. So, the yield reduces dramatically with decreasing L_e value.

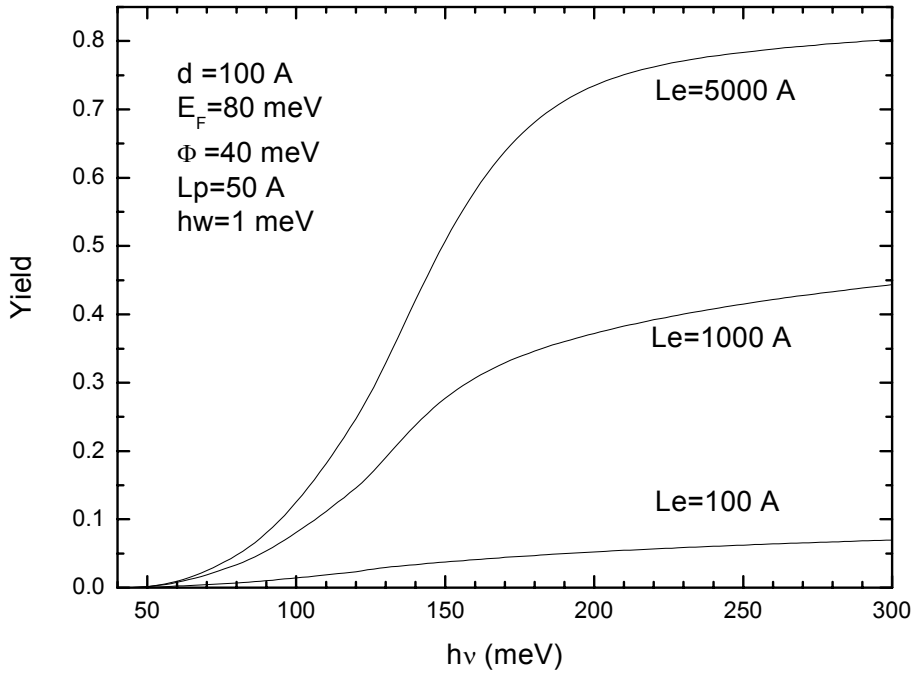

Fig. 2.19 Yield versus energy plots for several hot-hole/cold electron scattering mean free paths (L_e).

Fig. 2.20 shows the effect of the energy loss term on the yield. As we mentioned above when describing the other graphs, when the energy loss per collision decreases, carriers' chance to fall in the escape volume increases. Therefore, one can see the yield increases with a given excitation energy. This increase in the yield reduces for high photon energies because of the elimination of the previously emitted carriers. This is the explanation for the roll off at high energies in the graphs.

Effect of the Fermi level position in the active region to the yield is shown in Fig. 2.21. For the constant barrier height, there will be no change in the number of excited carriers as the Fermi energy decreases. They, however, will have relatively high energy and thus have more chance to be redirected into the escape volume

before collisions will thermalize the carriers. So, the yield increases with decreasing Fermi level.

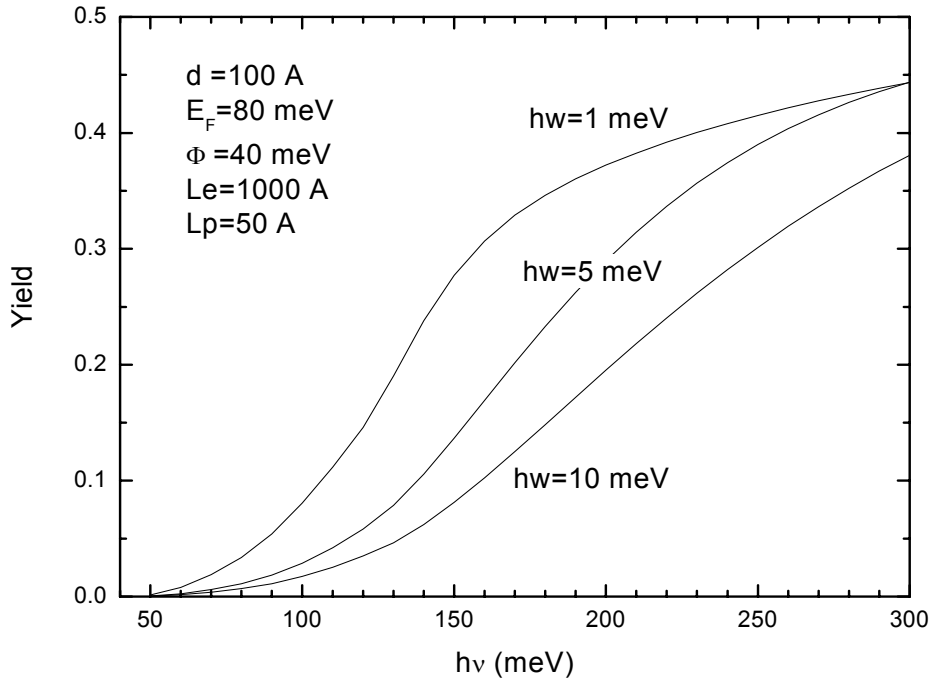

Fig. 2.20 Effect of the energy loss per collisions ($\hbar\omega$) term on the yield.

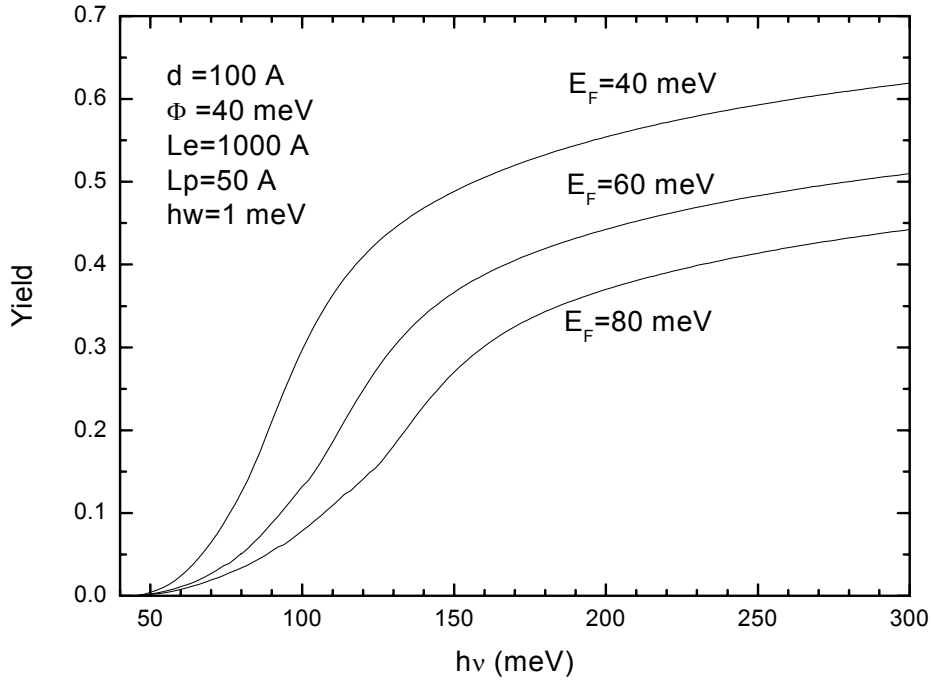

Fig. 2.21 Yield versus energy plots for different Fermi energies.

Finally, Fig. 2.22 shows the variation of the yield for different barrier height values. For constant Fermi level, when the barrier height gets smaller, there will be net increase in the number of carriers that can overcome the barrier. They can also be counted as relatively high energetic carriers. As a result, the yield increases with decreasing barrier height and the curves shift without changing their features.

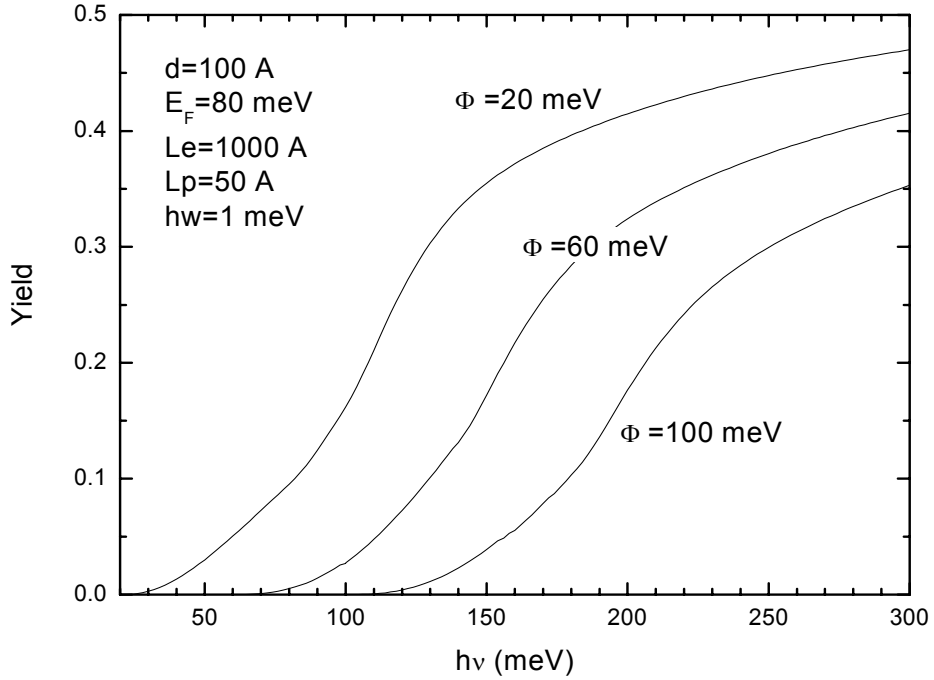

Fig. 2.22 Variation of the yield with different barrier height values.

2.7 Infrared Absorption

As it is stated at the beginning of this chapter, external yield is defined as the product of the optical absorption and the internal yield calculated above. Experiments showed that the incoming photons are absorbed in the film via free-carrier absorption [68,71,72]. Classically, free-carrier absorption results from the damped motion of carriers which are accelerated in the direction of the photon electric field (i.e. parallel to the wafer surface with normally incident illumination). The absorption coefficient (in cm^{-1} unit) is given [73]

$$\alpha = \frac{N_A q^2 \lambda^2}{8\pi^2 m^* n c^3 \tau} \tag{2.39}$$

where N_A is the doping concentration, q is the electronic charge, λ and n are respectively the wavelength of the incident photon and the index of refraction, m^* is the effective mass of the active region, c is the speed of light and τ is the relaxation time that reflects the influence of the scatterers. Since the optical absorption is the defined as the product of the absorption coefficient α and the film thickness d, then the external yield can be written as

$$Y_{ext} = \left(N_A\, d\, C^* \lambda^2\right) Y_{\text{int}} \tag{2.40}$$

where C^* is the collection of constant terms such as effective mass, optical constants, speed of light, etc. It is an unitless parameter whose order is around 10^{-10}. Fig. 2.23a shows the external yield versus photon's energy graph; the difference both in magnitude and shape can be easily seen when compared to the previous graphs (e.g. Fig. 2.17). Low yield values in the high energy part of the graph come from the wavelength dependent feature of the absorption process (Eq. (2.39)). In the calculations of the external yield, the following values were used for the parameters; $\Phi = 40$ meV, $E_F = 80$ meV, $d = 100$ Å, $L_p = 50$ Å, $L_e = 1000$ Å, $\hbar\omega = 1$ meV, $N_A = 5\times10^{19}$ cm^{-3} and $C^* = 1\times10^{-10}$. In Fig. 2.23b, same graph have been plotted in the form of Fowler plot since it is the traditional way of presenting the results.

In the analysis of our experimental results, this final form of the model was used and a good agreement was seen. Details of this analysis are given in chapter 3 and partly in chapter 4.

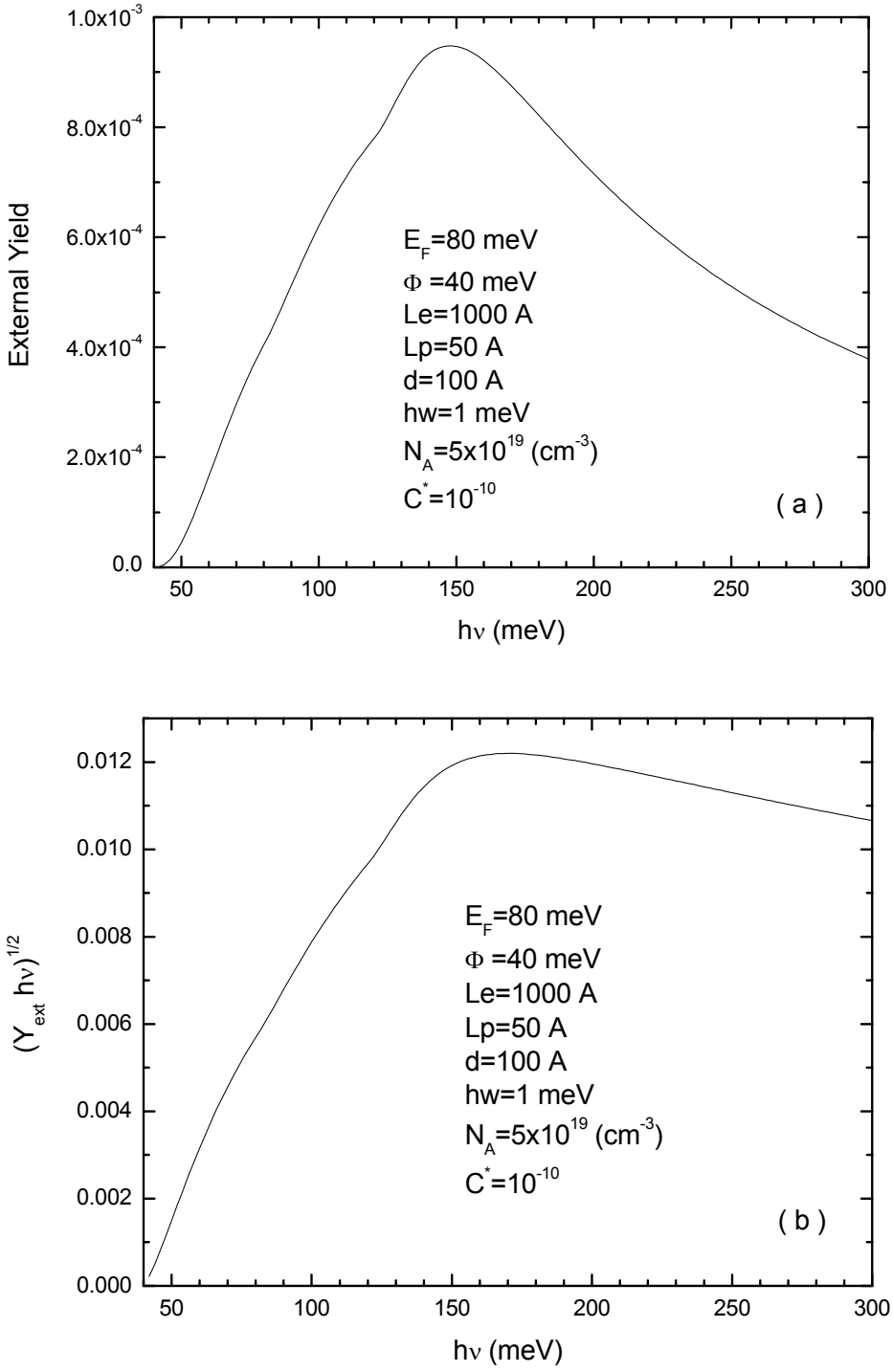

Fig. 2.23 a) External yield (product of the internal yield and the optical absorption) versus energy plot, b) same graph in the form of Fowler plot.

CHAPTER 3

MECHANISMS OF PHOTOCURRENT GENERATION IN SiGe/Si HIP INFRARED PHOTODETECTORS

$Si_{1-x}Ge_x$/Si heterojunction internal photoemission (HIP) infrared photodetectors have attracted a lot of interest in recent years [30,63,64,65,72,74,75]: Their cut-off wavelength adjustability over a wide infrared range, relatively high quantum efficiency at longer wavelength compared to silicide Schottky barrier detectors, and the compatibility with the existing Si technology make them attractive. The operation mechanism of the SiGe/Si heterojunction infrared photodetector is the same as that of the PtSi/Si Schottky barrier detector (discussed in chapter 5), which is the most popular and studied Schottky barrier detector [61,76]. The incident infrared radiation is absorbed via free carrier absorption in heavily doped $Si_{1-x}Ge_x$ layer and followed by the internal photoemission of photo-excited holes over the SiGe/Si heterojunction barrier into the Si collector layer. The cut-off wavelength λ_c of the HIP detector is determined by the effective barrier height Φ which is the energy difference between the $Si_{1-x}Ge_x$/Si valence band offset ΔE_v and the Fermi level E_F in the $Si_{1-x}Ge_x$ layer. Thus, the cut-off wavelength of a SiGe/Si HIP detector can be tailored over a wide infrared range by engineering the Ge content and the doping concentration of the $Si_{1-x}Ge_x$ layer.

The study on the mechanisms of the photocurrent generation can help us to obtain a clear physical understanding of the device operation. Although there have been many papers published on the detection mechanisms of HIPs, we feel that the basic current mechanisms have not been adequately addressed and clearly resolved. In

this chapter, physical effects governing the photocurrent generation process is studied, and therefore, the devices used here are not expected to have best performance for practical applications. As a matter of fact, for example, the responsivity values of our devices are less than that of similar ones. On the other hand, interesting experimental results were observed, such that they can be labeled as a "voltage tunable" infrared photodetector. Among infrared detector studies, multispectral detection and/or tunable cut-off wavelength properties have been paid special attention [34,36,77-81]. Schottky barrier [78], metal(silicide)-semiconductor-metal(silicide) [79,80], homojunction IPs [34,36], and especially quantum well structures [81, and references therein] have been the subject of these studies in recent years. In this chapter, we present a $Si_{1-x}Ge_x$/Si with x=0.11 HIP whose cut-off wavelength can be varied by the externally applied bias, and a qualitative model by identifying the photocurrent generation mechanisms in the structure to explain the experimental results. And finally, the experimental results of a set of samples with different parameters are presented. Part of this chapter has been published and can be found in [82].

3.1 Experimental Details and Device Operation

The samples used in this study were grown on 0.01-0.02 Ω cm Boron doped (3-8×10^{18} cm^{-3}) p-type Si (001) substrate by ultra-high-vacuum chemical vapor deposition (UHV-CVD). Details of the growth procedure have been given elsewhere [83]. A schematic layer structure and the valence band edge profile are shown in Fig. 3.1. Along the growth direction, the sample consists of 100 nm undoped Si layer, 38.2 nm p^+ -$Si_{1-x}Ge_x$ active layer with x = 0.11, and 5 nm p^+ -Si layer followed by a 197 nm p-Si top contact layer. $Si_{1-x}Ge_x$ active layer was doped to about 2.1×10^{19} cm^{-3} with boron to increase the amount of absorption and the top contact layer was doped to about 6×10^{18} cm^{-3} with B to act as a reservoir of charged carriers (holes). Layer thicknesses and the doping levels (also indicated in Fig. 1) were determined from x-ray diffraction (XRD) and Auger electron spectroscopy (AES). Doping levels were also verified by secondary-ion-mass-spectroscopy (SIMS) measurements. Similar structures with different Ge alloy fractions and layer thicknesses were also investigated and similar behaviors were observed.

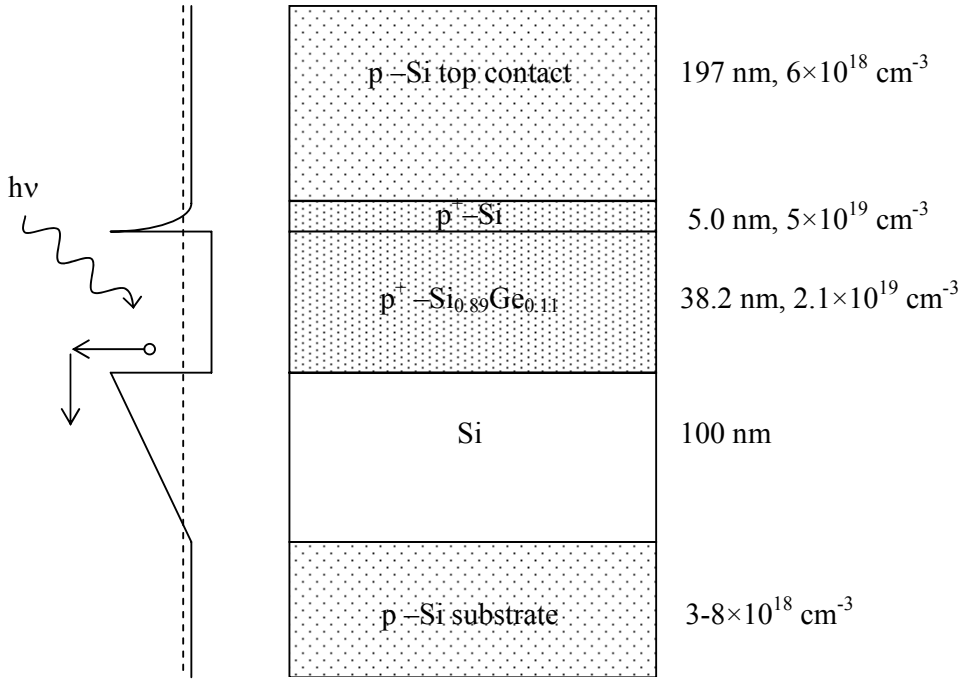

Fig. 3.1 Schematic device structure with layer thicknesses and the valence band edge profile showing the basic operation principle of the SiGe/Si HIP investigated here.

Mesa devices of 400x400 and 600x600 μm^2 in size were defined by wet etching, and top and bottom ohmic contacts were made by evaporating Al followed by rapid thermal annealing. The top Al contacts were ring shaped to allow normal incidence illumination. Fig. 3.2 shows the schematic representation of a device: in part (a) cross-section of the device and in part (b) the top view of the mesa with ring shaped Al ohmic contact are shown. Width of the square-shaped ring contact is 50 μm and the distance between the inner sides is 370 μm. For spectral photoresponse measurements, a closed cycle helium cryostat with KBr window and a Bomem MB100 Fourier transform infrared spectrometer with a globar source were used. Devices were illuminated from the top opening. The responsivity calibrations were done using a 1000-K blackbody infrared source, with the excitation wavelength selected by a variable narrowband filter. Fig. 3.3 shows the responsivity measurement setup.

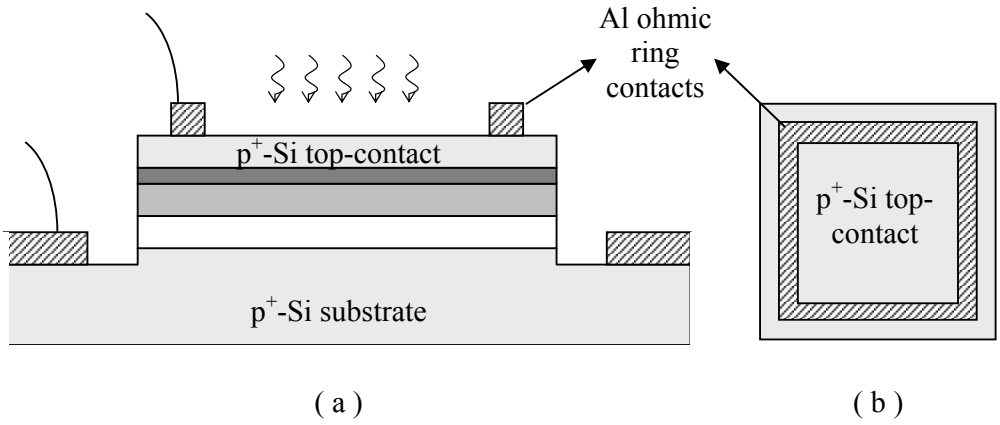

Fig. 3.2 The schematic representation of a device: (a) cross-section of the device and (b) the top view of the mesa with ring shaped Al ohmic contact.

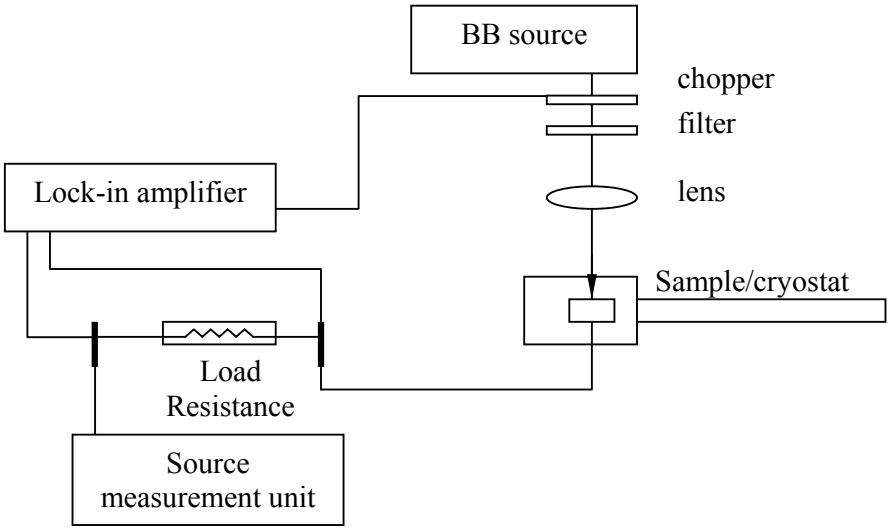

Fig. 3.3 Responsivity measurement setup.

3.1.1 Device Operation

The basic device operation (see Fig. 3.1) relies on the absorption (through free-carrier absorption) of the long wavelength infrared (LWIR) photons in a p-type heavily doped SiGe layer, followed by the collection of the photoexcited holes (i.e. internal photoemission) over the potential barrier formed by the SiGe-Si valence band offset, as demonstrated by Lin *et al* [30,84]. Our device design (Fig. 3.1),

which is first proposed by Liu *et al* [64], is similar but with some modifications for easier growth and fabrication. The undoped silicon layer forms a triangular barrier. $Si_{1-x}Ge_x$ active layer, which is doped heavily to enhance infrared absorption, is thick enough to ensure free carrier absorption and thin enough to increase the effect of multiple traversals through the SiGe film walls. To reduce the resistance from the heterojunction between SiGe and the p-Si layers (top contact) a heavily doped Si layer is added. The same structure with thin undoped SiGe layer inserted between i-Si and SiGe active layer has been used as a double-heterojunction Si-SiGe-Si unipolar transistor by fabricating a three terminal device [85].

Cut-off wavelength of our devices, unlike other HIPs in the literature having only SiGe/Si junction, have strong dependence on the applied bias. The voltage dependence of the photoresponse [86] and the quantum efficiency [66] have been presented before (in the literature) but this does not necessarily mean that the cut-off wavelength of the detector also depends on the voltage across the device. All SiGe/Si photodetectors, whose cut-offs change with the applied bias and showing the similar experimental results with ours, have a metal or a silicide layer to shape the potential barrier [35,77,79,87]. For the particular sample presented here, we obtained cut-off wavelength that can be tailored between 31 μm and 18.2 μm by changing the potential difference across the device. From the working region point of view, our devices can be compared with the Si based blocked impurity band (BIB) detectors even though the responsivity values obtained here are much less then that of BIB detectors [88-90]. Moreover, the structure presented here is superior to the BIB detectors in terms of the cut-off wavelength tunability.

3.2 Spectral Photoresponse and a Simple Model

Fig. 3.4 shows the spectral photoresponse curves for the SiGe sample under different potential differences across the device at 10 K. All voltage polarities are defined with respect to the bottom contact, i.e., the positive bias is defined as the top of the mesa biased positively with respect to the bottom. As seen in the figure, despite that the applied bias values are very small, dramatic changes were observed in the photoresponse of the device. When it is under illumination, the device has

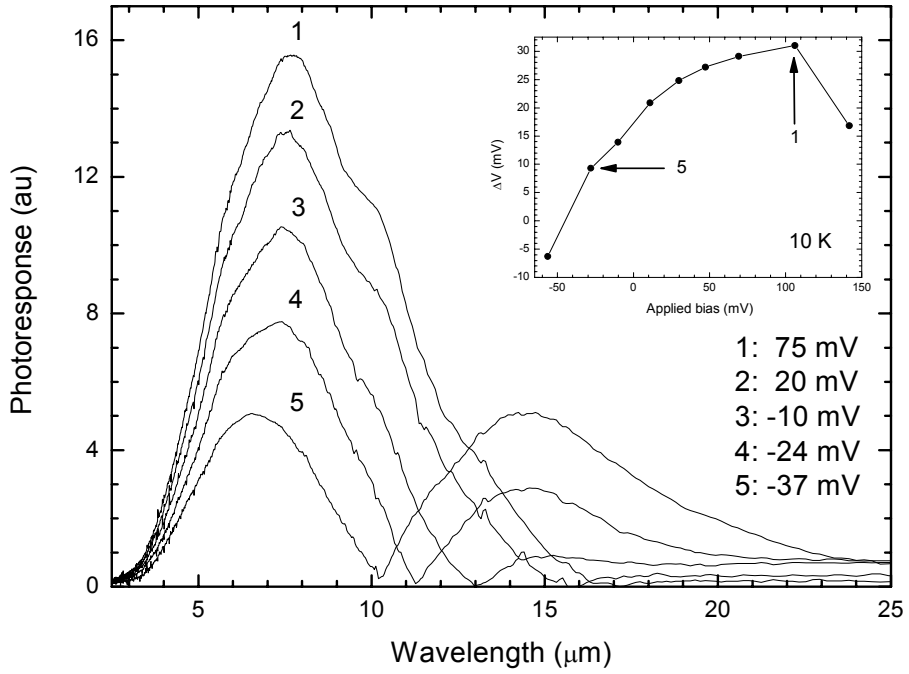

Fig. 3.4 Spectral photoresponse curves under different bias conditions at 10 K. The voltage values written in the legend are the potential differences across the device when it is illuminated by the light coming from the IR source. The inset shows the change in the photovoltage with the applied bias for 10 K measurements.

-37 mV offset voltage across its terminals and shows double peak feature in the photoresponse spectrum. As the device biased positively, the second peak appearing in the longer wavelength region of the spectrum starts to disappear while the first one becomes prominent. The first peak position shifts from ~6.5 μm to ~7.7 μm with the applied voltage whereas the second peak position remains unchanged. Note that the voltage values written in the legend are the potential difference values across the device when it is illuminated by the light coming from the IR source. The device has shown photovoltaic behavior. The inset in Fig. 3.4 shows the graph of the photovoltage, ΔV, versus applied bias for 10 K measurements. As shown here, as the applied bias is increased in positive direction, the photovoltage increases with decreasing increments. This means that the photocurrent produced in the structure increases with the applied bias and becomes almost constant at high voltages. Therefore, it can be concluded that there are other current mechanisms apart from the internal photoemission process in the structure or the internal photoemission is

somehow affected by the applied bias indirectly. The decrease in the final data is artificial because at that bias, it is difficult to sift the photocurrent due to the high dark current.

To interpret the observed results, we use the qualitative picture shown in Fig. 3.5. Under illumination, multiple photocurrents in opposite directions are generated in the structure: I_1 and I_2 are created by the photons absorbed in the SiGe well and directed towards the bottom contact and top contact, respectively. I_3 and I_4 are the photocurrents formed by the hot holes generated in the bottom and the top contact layers, respectively. The absorption in these layers together with the barriers leads to a net photocurrent. Depending on the p^+ -Si layer thickness and the device operating temperature, effects of the currents I_2 and I_4 to the net photocurrent can be significant. The model described here takes all possible current mechanisms into account. Due to different spectral responses and different positions along the light propagation path, their competition gives distinct outcomes in different spectral regions. As seen in Fig. 3.4, the second peak is not as strong (dominant) as the first one because most of the incident light is absorbed in the SiGe well before they reach the bottom contact and the absorption in p-Si region is not as high as that of in the SiGe region since the doping level is relatively low. According to this picture, I_1 and I_4 are responsible for the first peak while I_2 and I_3 are responsible for the second one. When the device is negatively biased, $V < 0$, valence band edge bends as shown in Fig. 3.5a. Therefore, the amount of current flowing towards the top contact (reverse direction) increases when compared to the equilibrium position, $V = 0$, and becomes comparable with the main current. Note that, at equilibrium there is a net photocurrent in the forward direction (towards the bottom contact) as considered in HIPs. We now discuss the reason of increase in the reverse current under negative bias: If the tunneling process from the SiGe/i-Si barrier is neglected, it can be said that I_1, the main current, is independent of applied bias, so it is constant. Due to the very thin barrier between the p^+ -Si and SiGe layers and the low operating temperature, the tunneling process can not be neglected for I_2, therefore, it increases. I_3 increases, too, because the apparent barrier for the carriers in reverse direction is reduced. As for I_4, since the generated holes see higher barrier

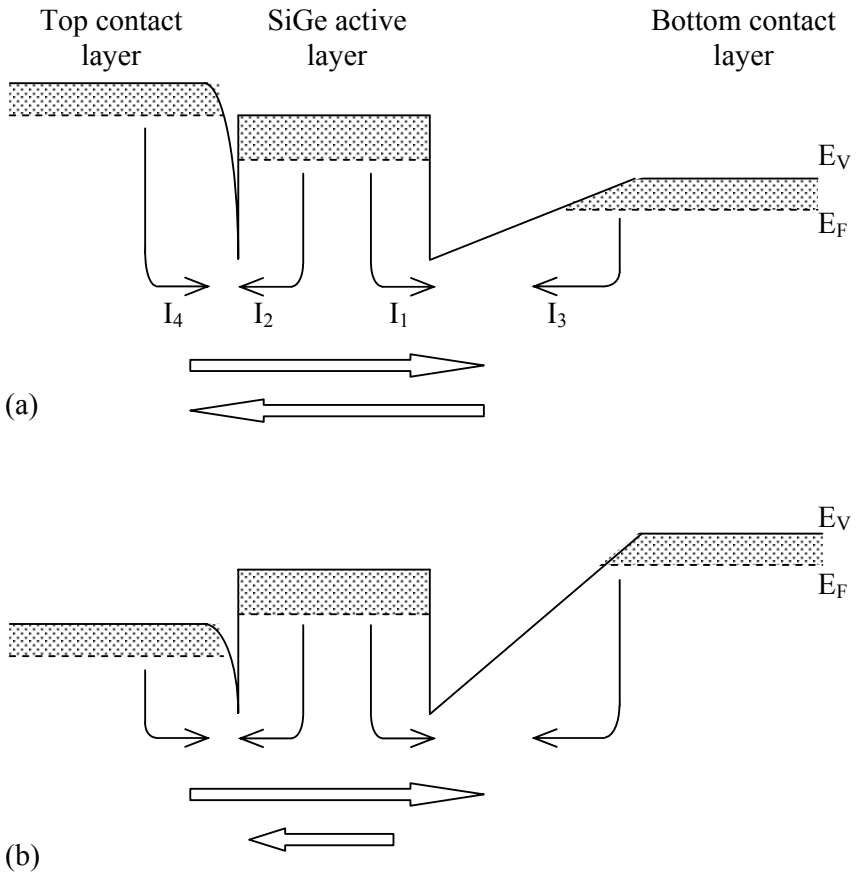

Fig. 3.5 Qualitative physical picture for interpreting the experimental results. The potential difference is negative for (a) and positive for (b). The bottom contact is the ground and arrows show the direction of the photoexcited holes' direction.

it decreases. Consequently, net current in the reverse direction increases with increasing reverse bias. In negative bias condition, since the potential barriers for the second and the third current mechanisms are less than that for the others, they show themselves in the long wavelength part of the spectrum. Thus, this second peak screens the main peak and therefore causes an artificial shift in the peak position as well as the decrease in the response as seen in Fig. 3.4. Moreover, since the cut-off wavelength of the device is determined by the smallest distinguishable barrier, the tale of the second peak stretch out in the longer wavelength as the potential difference across the device increase in the reverse direction. This feature is also clear in Fig. 3.4. On the other hand, when the device is biased positively, $V > 0$, band edge profile becomes as shown in Fig. 3.5b. In a similar approach with the

above discussion, the suppression of the reverse current and the increase in the net current in the forward direction can easily be explained. Briefly, the decrease in the tunneling probability for I_2, the increase in the potential barrier for I_3, and the decrease in the potential barrier for I_4 are responsible for this feature.

If the above qualitative interpretation is correct, we would expect a temperature change to simulate the effect shown in Fig. 3.4: The effect of the voltage increase (in the forward direction, i.e. from 5 to 1 in the Fig. 3.4) on the creek position should be similar to that of the temperature increase when the potential difference across the device under illumination is the same. But we would not expect the same increase in the response as in the figure. On the contrary, one can expect decline in the peak value because of the increase in the dark current. We then plotted the photoresponse versus wavelength graph (not shown here) for temperatures 10 K, 20 K and 30 K when V = -10 mV, and saw the same red shift in the creek's position. Additionally, it also met with the expectation of decrease in the maximum response value for higher temperatures. The effect of the temperature on the photoresponse curves of our devices when they are biased to obtain maximum signal can be found in the following chapter.

3.2.1 Fowler Analysis

As a result, our device acts as an infrared photodetector whose cut-off wavelength can be adjusted by applying different potential differences across the device. In order to demonstrate the change of cut-off wavelength with applied bias for this sample, the measured photoresponse data were converted to Fowler plots. Since the yield (or the quantum efficiency) can be written as the product of the responsivity (A/W) and the photon energy (eV), photoresponse data of the device (Fig. 3.4) were multiplied by a calibration constant in a way that the photoresponse value corresponding with the wavelength at which the responsivity measurement was performed will be the responsivity value obtained for that wavelength. Details of the responsivity measurements are given in section 3.3. For the conversion, we used the responsivity value obtained for the bias at which the spectral photoresponse measurements were done (see Fig. 3.7); 2.1 mA/W and 1.1 mA/W at 7.14 μm for

75 mV (curve 1 in Fig. 3.4) and 75 mV (curve 5 in Fig. 3.4) biases, respectively. Fig. 3.6 shows the experimental data and the theoretical fit (according to the model presented in chapter 2, Eq. 2.40) to the experimental data. The extracted barrier height values from the Fowler analysis are 68 meV and 40 meV that correspond to ~18.2 μm and ~31 μm cut-offs for curves number 1 and 5, respectively. In the fitting process, d = 382 Å, $N_A = 2.1\times10^{19}$ cm^{-3}, $C^* = 1\times10^{-10}$, M = 0.919 (=0.49/0.533), and corresponding E_F = 51 meV were used as unchanged parameters. Thus, for the results showed in Fig. 3.6, L_p = 38 (12) Å, L_e = 1200 (600) Å, $\hbar\omega$ = 1 (1) meV were obtained for curve 1 (5). These results also support the model presented in section 3.2: When the device is negatively biased (curve 5 case), since the currents I_2 and I_3 increases, the possibility of elastic and semi-elastic collisions increases. Therefore, the mean free paths for collisions decrease while the energy loss per collision term is constant.

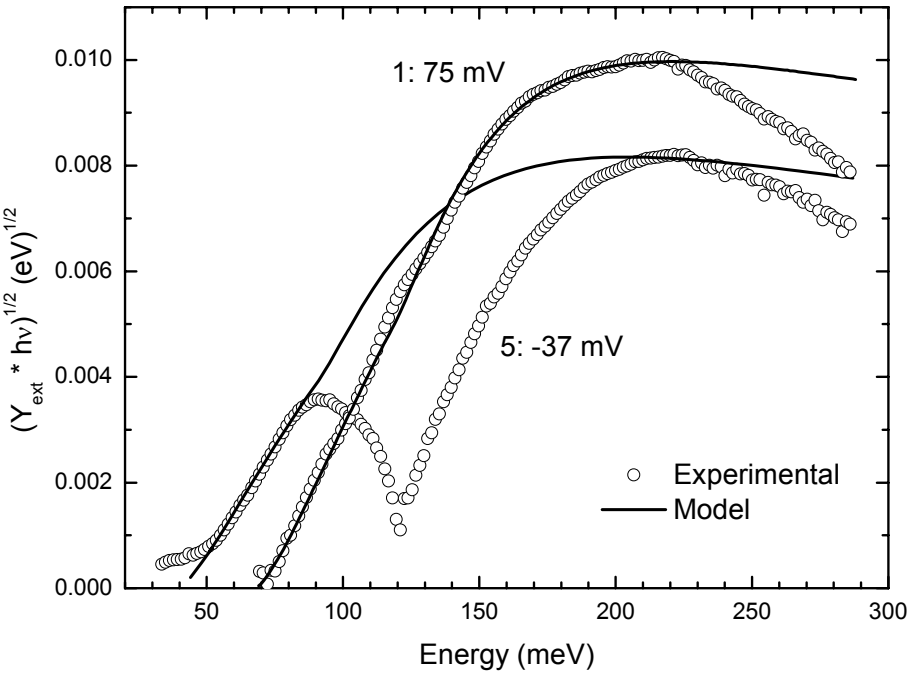

Fig. 3.6 Fowler plot of the experimental data (circles) and the theoretical fit (solid lines) for the device biased with 75 mV and -37 mV.

In the literature, the relation between the photoyield Y (or quantum efficiency) and the photon energy $h\nu$ is given by the equation [67]

$$Y = C_1 \frac{(h\nu - \Phi)^2}{h\nu} \tag{3.1}$$

because of the simplicity. Here C_1 is the emission coefficient depending on the absorptance and the Fermi energy level in the SiGe active region. In fact, Eq. (3.1) is the approximated form of the Eq. (2.15) ($\Phi < h\nu << E_F$), and does not include the scattering effects. Experimental data in Fig. 3.6 were also analyzed with this equation in order to show the differences between this model and the model presented in chapter 2. From Eq. (3.1), we obtained 17.8 μm and 28.3 μm cut-offs for curves number 1 and 5, respectively. As seen here, it then overestimates the barrier height of the junction.

3.3 Responsivity versus Voltage

The responsivity versus voltage characteristics of the device at different temperatures are shown in Fig. 3.7. Measurements were performed at the peak position of the spectral photoresponse curve, i.e. at 7.14 μm (see Fig. 3.4). As seen in the figure, responsivity of the device showed strange features that we do not fully understand, nevertheless, most of them can be understood by considering the model described in section 3.2. The general character of the curve is similar for all temperatures; therefore, we now talk on 10 K results (voltage values that will be given are different for different temperatures). The curve is in a complete harmony with the inset in Fig. 3.4 for the voltage region where the spectral photoresponse measurements have been performed, i.e., from about -50 mV to 150 mV. Change in responsivity values has a significant dependence on the voltage up to 0 mV, since the competition between currents is influential in that voltage range. The amount of currents flowing in opposite directions are the same at the turning point where the responsivity value is zero (non-zero for 30 K and 40 K because of the increase in the noise level arising from the high dark current and/or the lack of data at which both currents are equal). As for 0-170 mV region, responsivity is almost independent of the applied bias as expected from a HIP detector [66,86], so we call this region as “internal photoemission region”. However, at ~145 mV, there is a jump in the values and the graph makes a *nick* that we could not explain with a

negative slope. As the temperature increases, the nick's slope gets smaller and it covers a larger region. Starting from ~180 mV the increase can be attributed to the hole injection from the top to the SiGe layer, i.e., a nonequilibrium hole distribution is created in the center region (see Fig. 3.5b) [85,91]. Therefore, the hole current from the SiGe region to the bottom increases since the absorption in this region increases, too. Finally, the effect of the temperature to the graph can be explained as follows: Since the reverse currents (I_2 and I_3) are suppressed as the temperature increases, the main current mechanisms (basically I_1, and I_4) become dominant. Thus, the effect of the high voltage for the low temperature can be achieved with lower voltage at high temperature. As a result, all features seen in Fig. 3.7 (such as shift in zero point crossing and the position of the nick, etc) shift towards the small voltage region in the graph as the temperature goes up. Indeed, this is what we observed in the spectral photoresponse measurements at higher temperatures.

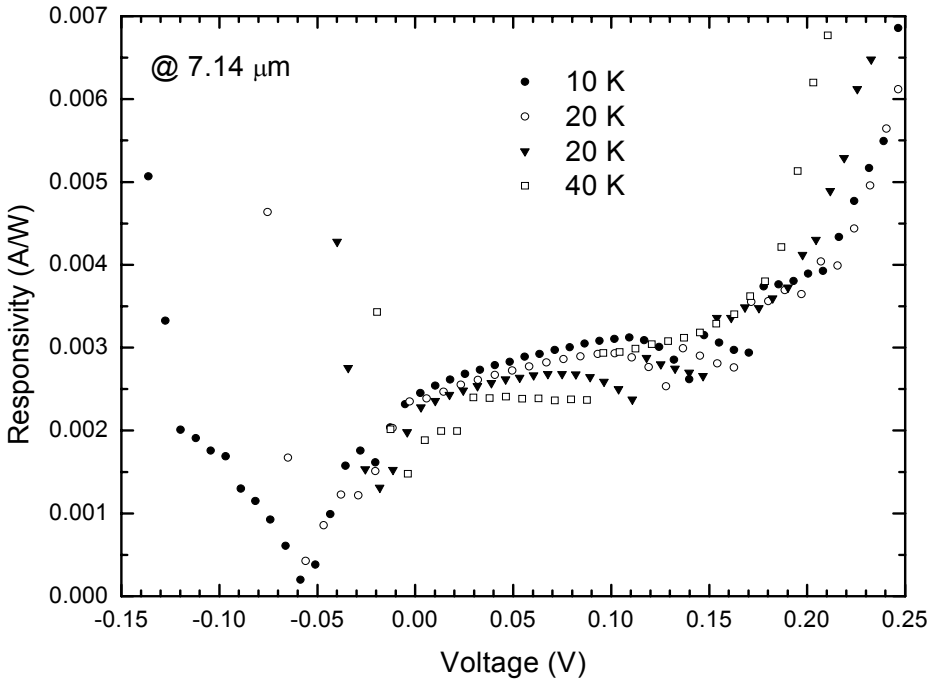

Fig. 3.7 Responsivity versus voltage characteristics of the device at different temperatures. Measurements have been performed at 7.14 μm.

For the sake of completeness, detectivity D^* values were obtained by using shot noise approximation. Since we could not read the dark current values below 100 pA due to the electrical noise limit of the measurement setup, the peak value of the detectivity was estimated; it is in the order of 10^{12} cm $Hz^{1/2}$ /W. This value is less than that of BIB detectors [88,89], but higher than SiGe HIP detectors' detectivity values presented in the literature [65,72,74].

3.4 I-V Characteristics and Activation Energy Analysis

To understand the carrier transport through the structure, I-V characteristics of the samples were studied under different experimental conditions. I-V curves of the sample, which were obtained when it is exposed to the light coming from the laboratory environment, are shown in Fig. 3.8. The dark current obtained at 10 K was also plotted for comparison. The graph is completely in agreement with the other measurements presented above. The excess current seen for low bias and temperature values is due the photo-generated carriers at or near the barriers. This current is composed of two components: the internal photoemission over the barrier and the band-to-band excitation in the intrinsic Si in which an electric field is set up. The band-to-band excitation is effective for photon energies greater than silicon bandgap at the measurement temperature. The photocurrent is observable at low temperatures where the dark current is suppressed sufficiently. The presence of the potential barrier manifests itself as a step feature in the photocurrent part of the I-V curves. Note that the voltage region where the step has been seen corresponds to the "internal photoemission region" excluding the nick part in Fig. 3.7. This step disappears as the temperature increases because the dark current through the barrier junction starts to dominate the current at relatively low temperatures. The dark current is an important issue when the device performance is considered.

It is well known that the temperature dependence of the dark current can be used to determine the barrier height of the device by using the thermionic current equation [92],

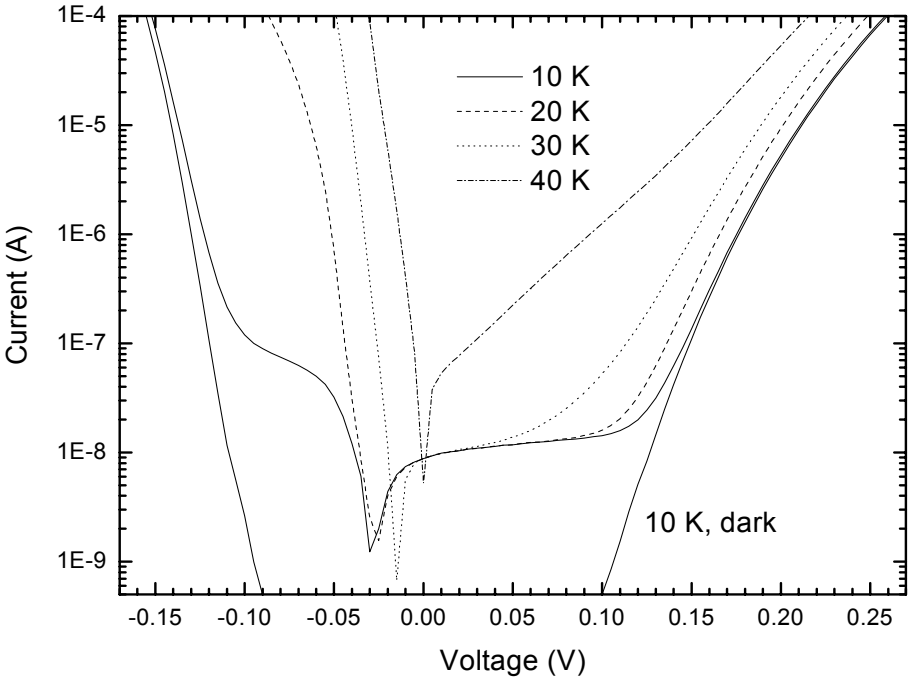

Fig. 3.8 Semilogarithmic plot of I-V characteristics of the sample under different experimental conditions.

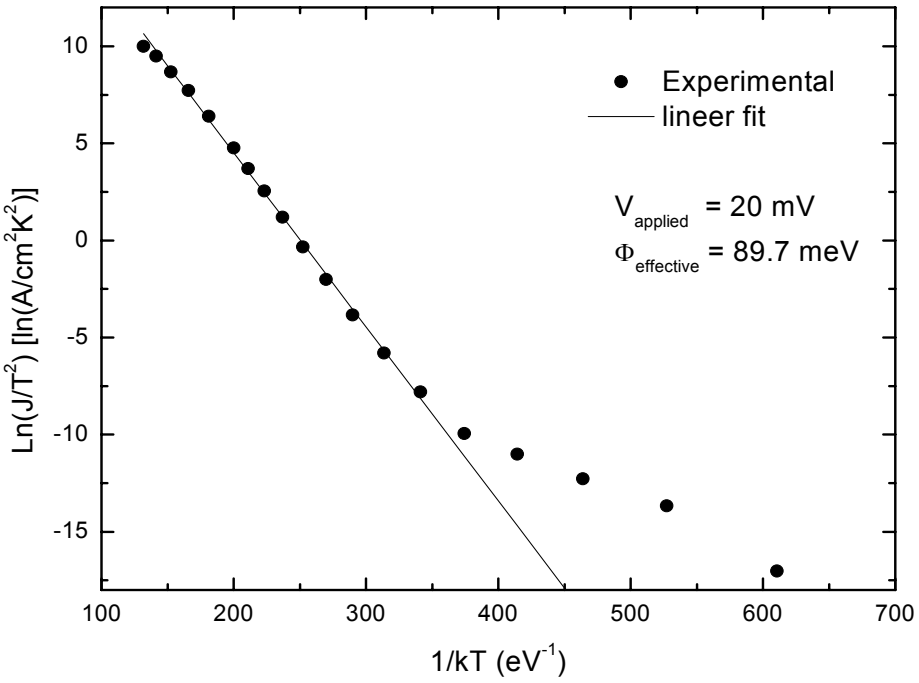

Fig 3.9 Activation energy plot for determination of barrier height.

$$I = AA^{*}T^{2}\exp\left(-\frac{\Phi - qV_a}{kT}\right) \tag{3.2}$$

where A is the device area, A^{*} is the Richardson constant, and V_a is the applied bias. As seen here, the slope of a plot of $\ln(J/T^2)$ versus $1/kT$ (known as Richardson plot) yields the activation energy (effective barrier height) $\Phi - qV_a$. Fig. 3.9 shows the activation energy plot of the forward current (20 mV) in our device for determination of barrier height. From the slope, 89.7 meV activation energy was obtained, which corresponds to 69.7 meV barrier height. This value is very close to barrier height value obtained from Fowler analysis, 68 meV. The discrepancy between the experimental data and the solid line (linear fit) at low temperatures comes from the fact that thermionic current is not the dominant current mechanism at very low temperatures. This is the region in which tunneling processes become more effective. Actually, this discrepancy for Schottky type junctions has been studied extensively as a part of current mechanism studies. Since this point is not within the main concern of this thesis, it is not discussed further. For more details, see [93], and references therein.

3.5 Samples with Different Parameters

The sample discussed in above sections in fact belongs to a set of samples with different parameters. Since each sample has the same structure and shows the same behavior in terms of the experimental results, we found that it is convenient to present all the results over only one of them. As in this section, details of the other samples and the experimental results are given in a very compact form.

Table 3.1 shows the structural parameters of the samples as determined by XRD, AES and SIMS. Note that the sample used in the previous sections is 1108. The spectral photoresponse curves of the entire set are shown in Fig. 3.10. For these spectrums, devices were biased with 75 mV except for sample 1105 which was biased with 20 mV. These are the values at which maximum signal was obtained. Besides, photoresponse values were normalized to 1 to make easy comparison between different samples. It is seen that the cut-off wavelengths changes in a range

of ~14 μm to ~27 μm depending on the Ge content and doping amount in the SiGe active region of that sample.

Table 3.1 Structural parameters of the samples.

	$Si_{1-x}Ge_x$			i-Si		Si contacts	
Sample	Thickness (nm)	x	Doping (cm^{-3})	Thickness (nm)	Doping (cm^{-3})	Thickness (nm)	Doping (cm^{-3})
1105	16.9	0.100	1.6E19	4.2	6.3E19	188	1.7E18
1107	31.2	0.093	1.5E19	4.0	4.5E19	201	6.0E18
1108	38.2	0.110	2.1E19	5.0	5.0E19	197	6.0E18
1109	18.9	0.135	2.5E19	4.0	3.3E19	198	4.5E18
1110	11.6	0.132	2.0E19	4.8	2.7E19	198	5.5E18

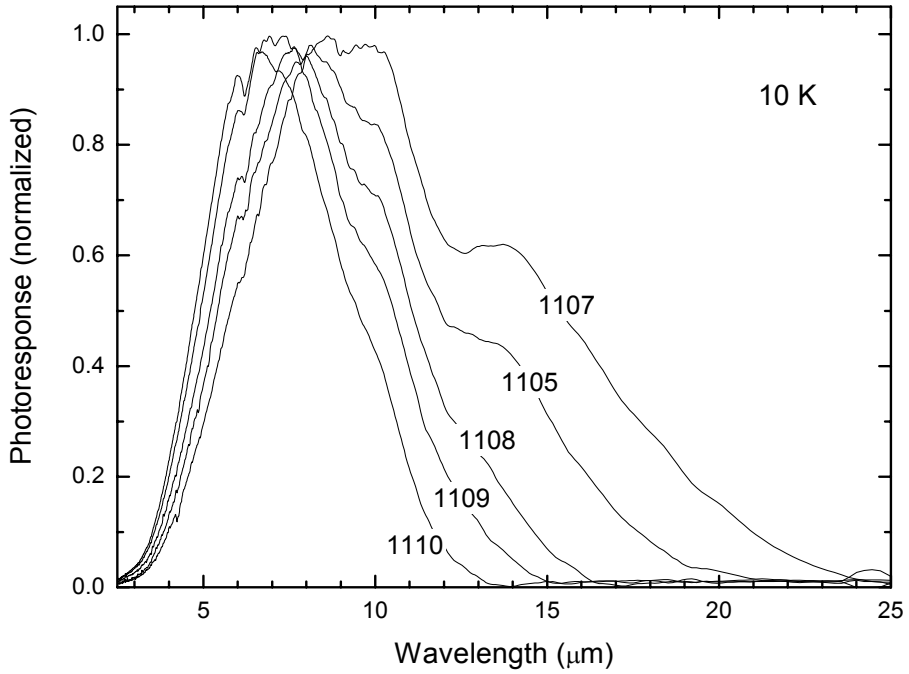

Fig 3.10 Spectral photoresponse curves for a set of samples. Samples were biased with 75 mV except 1105 which is biased with 20 mV.

Fowler and activation energy analysis also confirm the order in Fig.3.10. The Richardson plot for all the samples can be seen in Fig. 3.11. Parameters used in Fowler analysis and the extracted barrier height values both from Fowler and

Richardson plots are presented in Table 3.2. It can be seen that barrier height values obtained from Fowler plot and activation energy analysis are very close to each other. We should, however, note that the result of Fowler analysis is not unique because of too many adjustable parameters involved in the calculations such as L_p, $\hbar\omega$, and L_e. Even though there are no certain values available for these parameters, they are within the suggested range. The values given in Table 3.2 are from the best fit results. What is surprising in these analyses is that the very small difference in the Ge content (‰7) in samples 1105 and 1107 is distinguished by both methods (the doping values are almost the same). And finally, the responsivity versus voltage curves for the entire set are shown in Fig. 3.12.

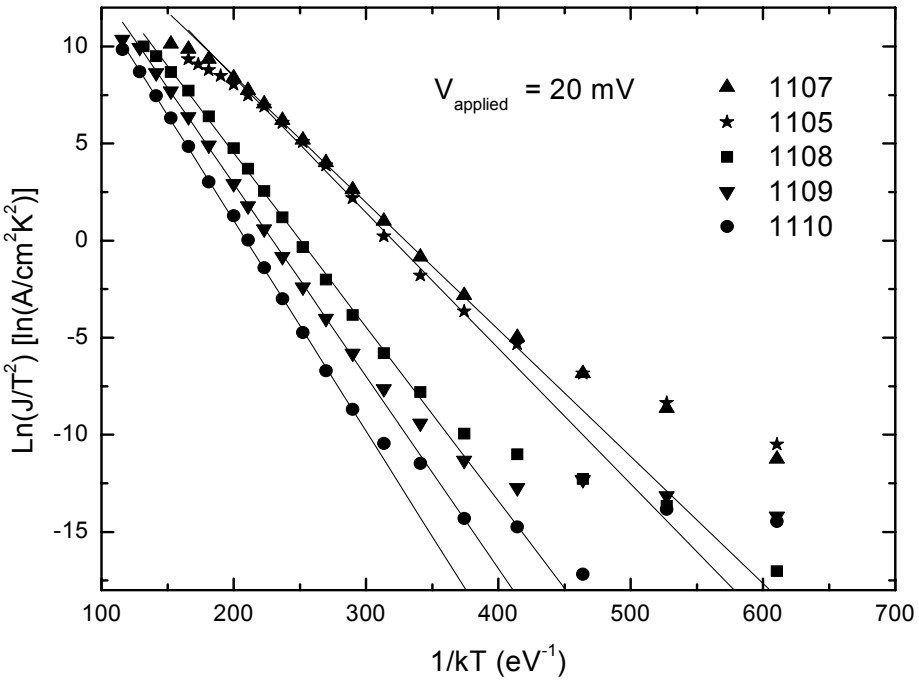

Fig. 3.11 Activation energy plots for determination of barrier height (for the entire set of samples).

Table 3.2 Parameters used in Fowler analysis and the barrier height values obtained from both electrical and optical measurements.

Sample	**1105**	**1107**	**1108**	**1109**	**1110**
M	0.974	0.978	0.919	0.959	1.010
C^*	1E-10	1E-10	1E-10	1E-10	1E-10
E_F (meV)	44	43	51	58	53
L_p (Å)	50	60	38	40	75
L_e (Å)	4200	2000	1200	1550	4000
$\hbar\omega$ (meV)	2	2	1	1	2
Φ_{Fowler} (meV)	52	46	68	75	86
$\Phi_{Act.}$ (meV)	49.9	45.4	69.7	79.1	88.4

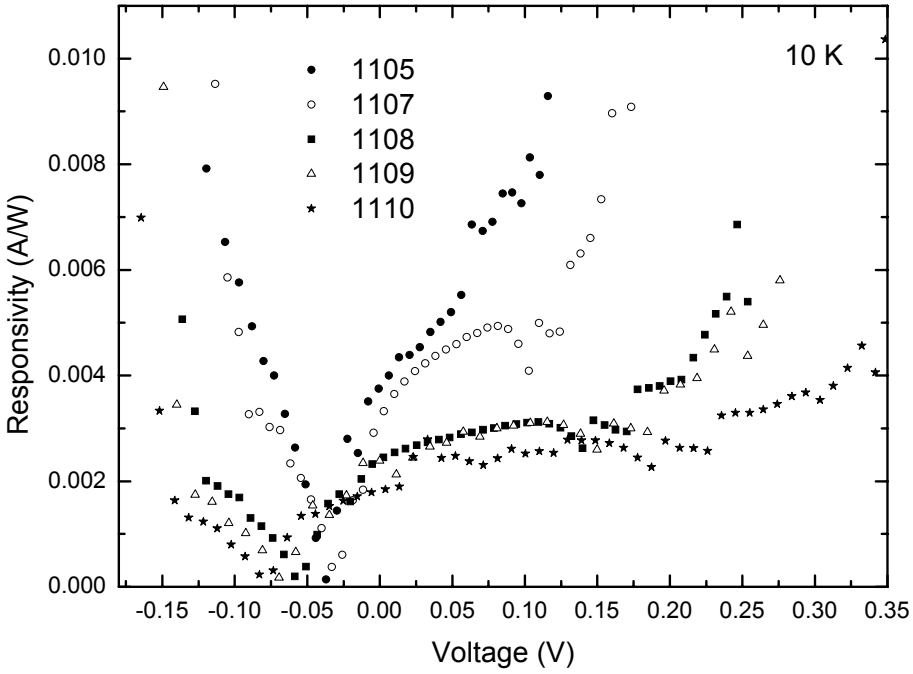

Fig. 3.12 Responsivity versus voltage characteristics of the devices at 10 K. Measurements have been performed at 8.06 μm, 8.06 μm, 7.14 μm, 6.67 μm, and 6.25 μm, respectively.

CHAPTER 4

DOUBLE-BARRIER LONG WAVELENGTH SiGe/Si HIP INFRARED PHOTODETECTORS

Among infrared detector studies, multispectral detection and/or tunable cut-off wavelength properties have been paid special attention [77,78,80,81,94]. Schottky barrier [78], metal-semiconductor-metal [80], and especially quantum well structures [64, 81 and references therein] have been the subject of these studies in recent years. At the beginning of chapter 3, the advantages and the operation principles of the $Si_{1-x}Ge_x$/Si heterojunction internal photoemission (HIP) infrared photodetectors were mentioned. Moreover, voltage dependence of our samples' responses has been presented with a qualitative model. As in this chapter, in addition to the samples presented in chapter 3, we present the temperature dependent cut-off wavelength of double barrier $Si_{1-x}Ge_x$/Si HIP infrared photodetector. Our proof of concept device, which has two $Si_{1-x}Ge_x$/Si junctions with x = 0.1 and x = 0.23, has the cut-off wavelength of 22.5 μm at 10 K and 12.6 μm at 50 K. As the temperature increases, the small barrier becomes invisible for the holes since they have enough thermal energy to overcome the barrier. Although the details of the sample 1105 were given in previous chapter, it will be mentioned again with the sample 1111 (new one) for the self-consistency. Part of this chapter has been published and can be found in [95].

4.1 Experimental Details

Two samples, labeled as 1111 and 1105, were grown on 0.01-0.02 Ω cm Boron doped ($3\text{-}8\times10^{18}$ cm^{-3}) p-type Si (001) substrates by ultra-high-vacuum chemical

vapor deposition (UHV-CVD) with nominally identical parameters except for the number of layers. Details of the experimental procedure have been given elsewhere [83]. The device structure and the valence band edge profile for sample 1111 are shown in Fig. 4.1. Sample 1105 only has the layers up to the first p-Si layer, which acts as the top contact. In other words, sample 1105 has only one $Si_{1-x}Ge_x$/i-Si junction, which determines the cut-off wavelength of the device, with x=0.1, whereas the sample 1111 has a second junction with x=0.23 in addition to this first junction also with x = 0.1. Therefore, the cut-off wavelength of this device will be determined by the combined effect of these two junctions depending on the operating temperature. The layer thicknesses for both samples are also given in Fig. 4.1. The top contact layers were doped to about 2×10^{18} cm^{-3} with B to act as a reservoir of charged carriers (holes). In order to increase the amount of absorption, $Si_{1-x}Ge_x$ active layers were doped to about 2×10^{19} cm^{-3} with boron. The doping was about 4×10^{19} cm^{-3} for thin p^+-Si layers inserted between the top contact and the SiGe active layers. As mentioned in chapter 2, layer thicknesses and the doping levels were determined from x-ray diffraction (XRD) and Auger electron spectroscopy (AES). Doping levels were also verified by secondary-ion-mass-spectroscopy (SIMS) measurements. Details of the mesa devices and the measurement techniques are the same as that mentioned in section 3.1.

Sample 1111 consists of two single HIP infrared photodetectors that have different cut-off wavelengths grown in a stack mode. Due to our mesa definition in the microfabrication process, it works as a single detector whose cut-off depends on the operating temperature. As the temperature decreases, the contribution of the small barrier to the photoresponse of the device becomes prominent. In fact, it determines the cut-off wavelength. This structure (sample 1111) can also be fabricated as a three terminal device by contacting the intermediate conducting layer (p-Si), which separates two HIP photodetectors grown in a multistack. This results in a separately readable and addressable multispectral HIP detector. This approach was first demonstrated by Köck *et al* [94] for GaAs/AlGaAs multi-quantum well structures.

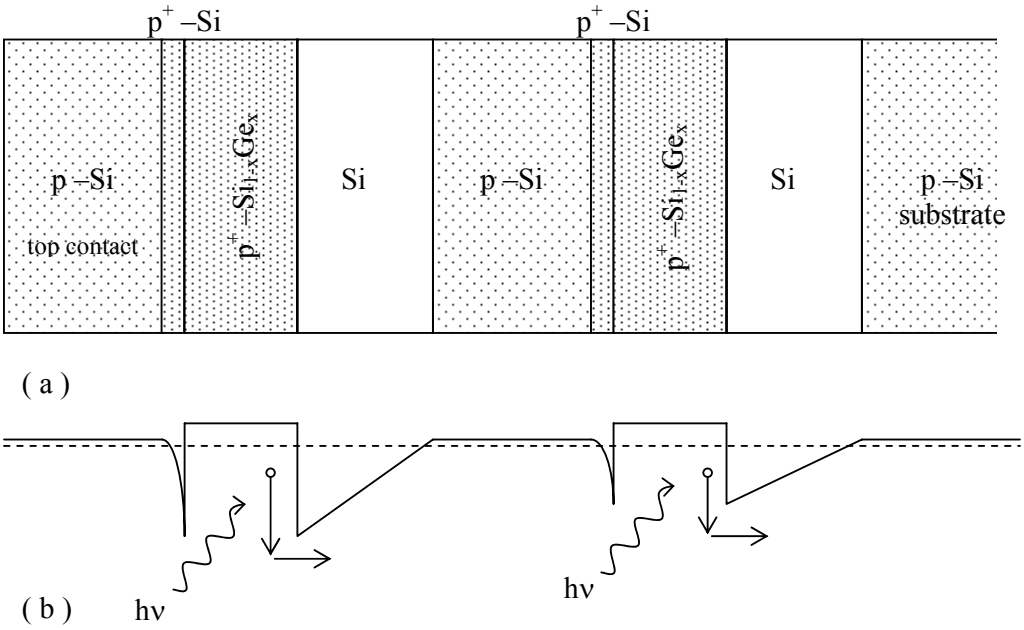

Fig. 4.1 Schematic device structure with layer thicknesses for both sample 1111 and sample 1105 (a) and the valence band edge profile showing the operation principle (b).

4.2 Experimental Results and Discussions on the Double-Barrier SiGe/Si HIP

4.2.1 Spectral Photoresponse

Figure 4.2 shows the spectral photoresponse curves for samples 1111 (a) and 1105 (b) at different temperatures under small positive bias. Positive bias is defined as the top of the mesa biased positively with respect to the bottom. Applied voltage values are given in the figure caption. These are the values at which maximum signal was obtained. Photoresponse values were normalized to 10 to make easy comparison between different temperature results and between different samples. As seen in Fig. 4.2a, the cut-off wavelength gets smaller as the temperature increases for the sample that has two barriers with different heights. At low temperatures, the effective cut-off wavelength of the device is mainly determined by the $Si_{0.9}Ge_{0.1}$/Si junction whose valence band discontinuity is smaller than that of the $Si_{0.77}Ge_{0.23}$/Si junction. In fact, the combined effect of the two barriers determines the cut-off wavelength of the device; for less energetic photons, the higher barrier (created by

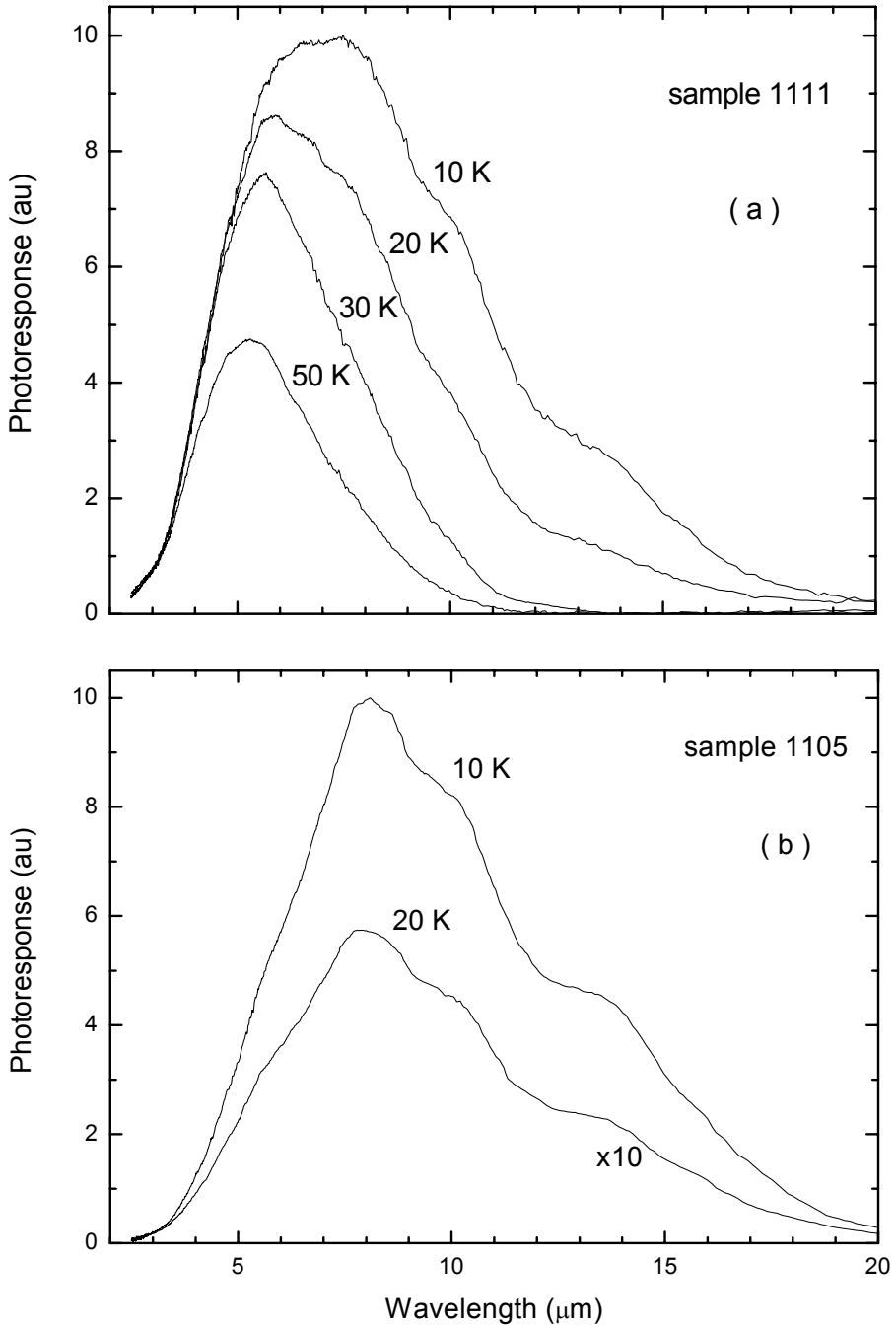

Fig. 4.2 Spectral photoresponse curves under positive bias at different temperatures for sample 1111 (a) and for sample 1105 (b) under small positive bias. Applied bias values are 250 mV (10 K), 200 mV (20 K), 125 mV (30 K), and 30 mV (50 K) for sample 1111. As for sample 1105, 20 mV was applied at both temperatures. Note that 20 K spectrum was multiplied by 10.

$Si_{0.77}Ge_{0.23}$, in which photons are expected to be absorbed, and Si interface) has a screening effect. This can be seen clearly when 10 K photoresponse curves of both samples are compared; in spite of having the same parameters, sample 1105 has slightly longer cut-off wavelength and higher response at 10 K than sample 1111 has, because some of the photons that have long wavelength are absorbed until they reach the $Si_{0.9}Ge_{0.1}$layer. The effect of double barrier is clearly seen in Fig. 4.2. As the temperature increases, the peak position of the photoresponse curves for sample 1111 shifts towards the lower wavelength region whereas that for sample 1105 does not change with the temperature. Note that the response of the sample 1105 for 20 K reduced remarkably (see Fig. 4.2b) although there is no change in the shape of the spectrum, i.e. when 10 K and 20 K spectra are normalized to the same value, it can be seen that they match well. As for temperatures 30 K and above, no signal from the sample 1105 was detected since the barrier height is small enough for thermally excited carriers (holes). Sample 1111, however, gives relatively a strong response to the light even at 50 K due to the presence of the large barrier. The decrease in the response at short wavelength region of the spectra is because of the fact that the free carrier absorption decreases as the wavelength of the light decreases [92]. The lack of response at around 9.5 and 12 μm (the wavy feature) seen in Fig. 4.2 is an instrumental effect.

4.2.2 Fowler analysis and Responsivity

The double barrier sample acts as a temperature tunable infrared photodetector. In order to demonstrate the change of cut-off wavelength with temperature for this sample, the measured photoresponse data were converted to Fowler plots by following the same way as described in section 3.3.1. For the conversion, we used the responsivity value obtained for the bias at which the spectral photoresponse measurements were done; 3.5 mA/W and 2.4 mA/W at 5.8 μm for 10 K and 50 K, respectively. The responsivity versus voltage graph of the device for both temperatures is presented in Fig. 4.3. It shows the same behaviors with the responsivity versus voltage graph for one barrier sample described in section 3.4 (see Fig. 3.7). As in current-voltage graph it shows the double-barrier feature on the curve.

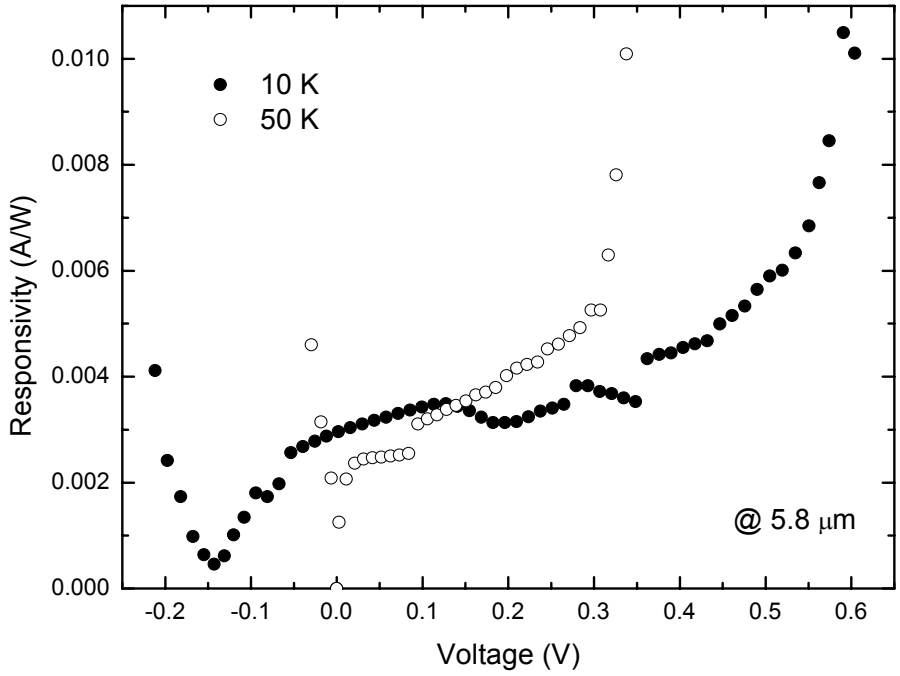

Fig. 4.3 Responsivity versus voltage characteristics of the sample 1111 at different temperatures; 10 K and 50 K. Measurements have been performed at 5.8 μm.

Fig. 4.4 shows the photoresponse of the double-barrier sample at 10 K and 50 K in the form of Fowler plot. The shift in the cut-off wavelength is clearly seen in this figure. The curves were analyzed by using both Eq. (3.1) and Eq. (2.40) and the fit lines were shown on the graph; dashed lines are for Eq. (3.1) and will be called as "modified Fowler" while the solid lines are for Eq. (2.40) and will be called as "the model" in this chapter. In fact, it might have not been proper to analyze these spectrums with "the model" described in chapter 2 since the sample has two barriers and model was derived for one junction. But, at least for the barrier height determination it must be more reliable than the modified Fowler. The extracted barrier height values from the solid (dashed) lines in Fig. 4.4 are 22.5 μm (19.9 μm) and 12.6 μm (11.7 μm) for 10 K and 50 K respectively.

For the sake of completeness, detectivity D^* values were obtained by using shot noise approximation. Obtained peak value, 2×10^{11} cm $Hz^{1/2}$ /W for sample 1111, is in agreement with the literature [65].

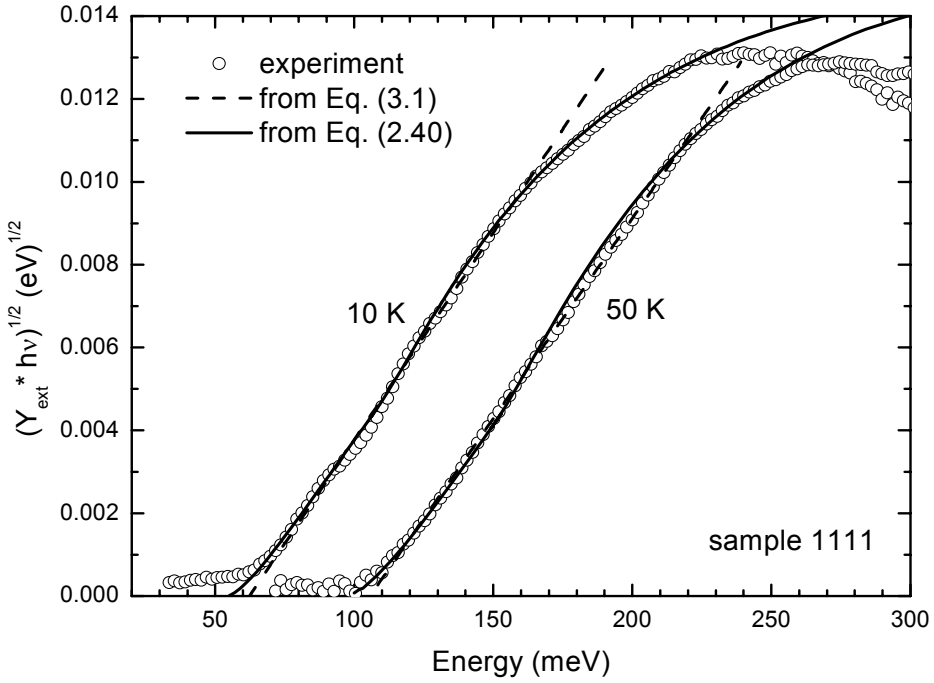

Fig. 4.4 Fowler plots of internal photoemission spectra for the sample 1111 at 10 K and 50 K.

4.2.3 I-V and Activation Energy Analysis

In order to understand the carrier transport through the double barrier structure, I-V characteristics of the samples were studied under different experimental conditions. I-V curves of the sample 1111, which were obtained when it is exposed to the light coming from the laboratory environment, are shown in Fig. 4.5a. The excess current seen for low bias and temperature values is due the photo-generated carriers at or near the barriers. This current is composed of two components: the internal photoemission over the barriers and the band-to-band excitation in the intrinsic Si in which an electric field is set up. The band-to-band excitation is effective for photon energies greater than silicon bandgap at the measurement temperature. The photocurrent is observable at low temperatures where the dark current is suppressed sufficiently. The presence of double potential barrier in the sample 1111 manifests itself as a double step feature in the photocurrent part of the I-V curves. This feature is not seen in the sample with single barrier as shown in Fig. 4.5b. The wider step seen in the I-V curves of sample 1111 for low voltage values is likely to result from

the larger barrier because the applied voltage drops mostly across the large barrier in this part of the I-V curve. The photocurrent due to the small barrier becomes observable as a second (higher) step at about 0.2 V only after the applied voltage is high enough to generate a significant effect from this barrier. This small step disappears first as the temperature increases because the dark current through the small barrier junction starts to dominate the current at relatively low temperatures. In Fig. 4.5b, a comparison between samples 1105 and 1111 is given. Sensitivity to the light is observable for small voltage values. This photocurrent component disappears in the dark current upon a small increase in the sample's temperature just like the small step in the I-V curve of the sample 1111 discussed above. Another effect of the presence of double barrier is the reduction of the dark current through the device. As clearly seen in Fig. 4.5b the dark current is reduced by many orders of magnitude when a second junction with a larger potential barrier is incorporated into the device. The irregularities below 100 pA in Fig. 4.5b are due to the electrical noise limit of the measurement setup. The dark current is an important issue when the device performance is considered.

Using the dark current values for different temperatures, the activation energy analysis was also done on sample 1111 and shown in Fig. 4.6. From the slope of the linear part of the experimental data, 120 meV effective barrier was obtained, which corresponds to 100 meV barrier height since the applied bias for Fig. 4.6. This value is again very close to value obtained from the Fowler analysis by "the model".

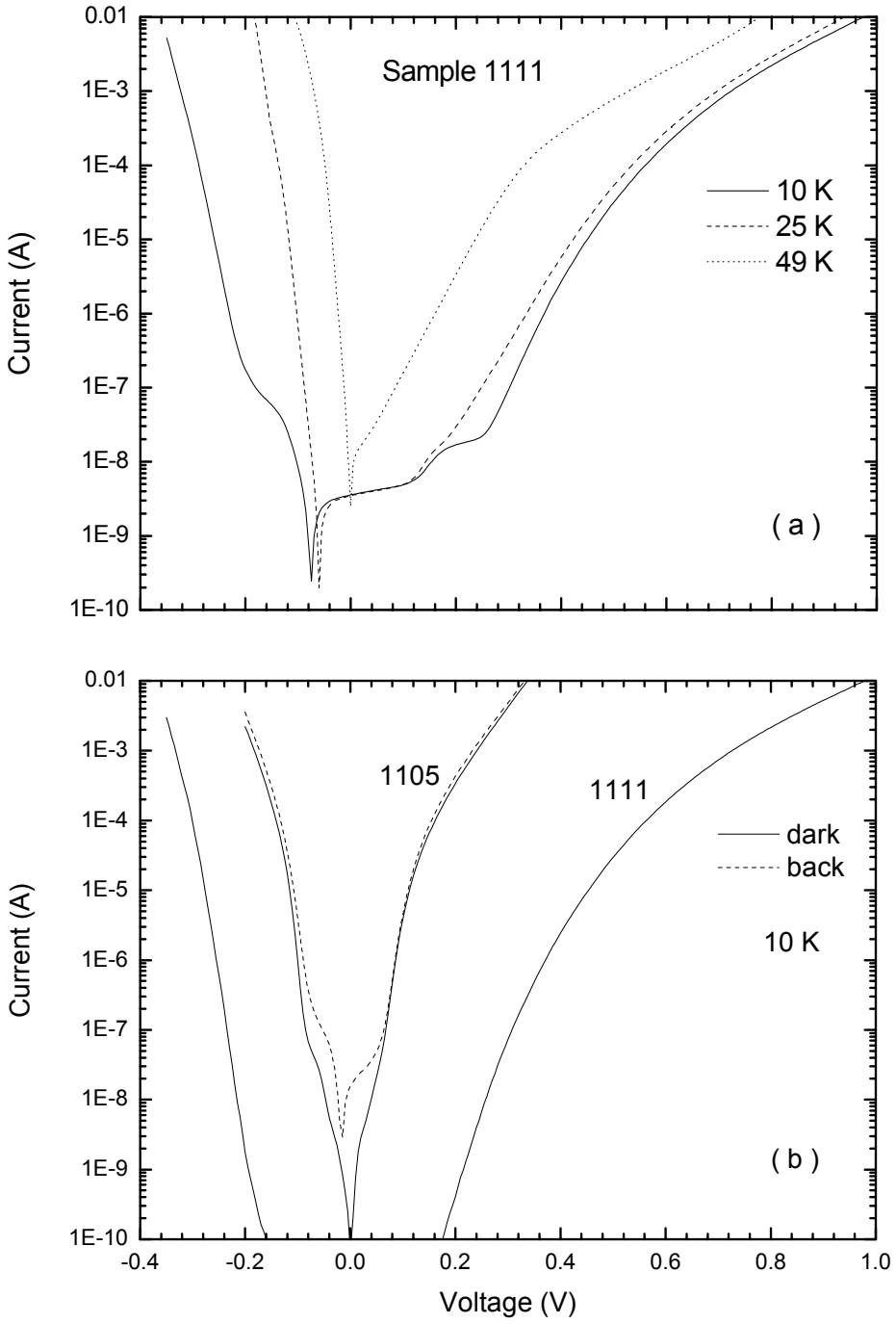

Fig. 4.5 Semilogarithmic plot of I-V characteristics of the samples 1111 and 1105 under different experimental conditions.

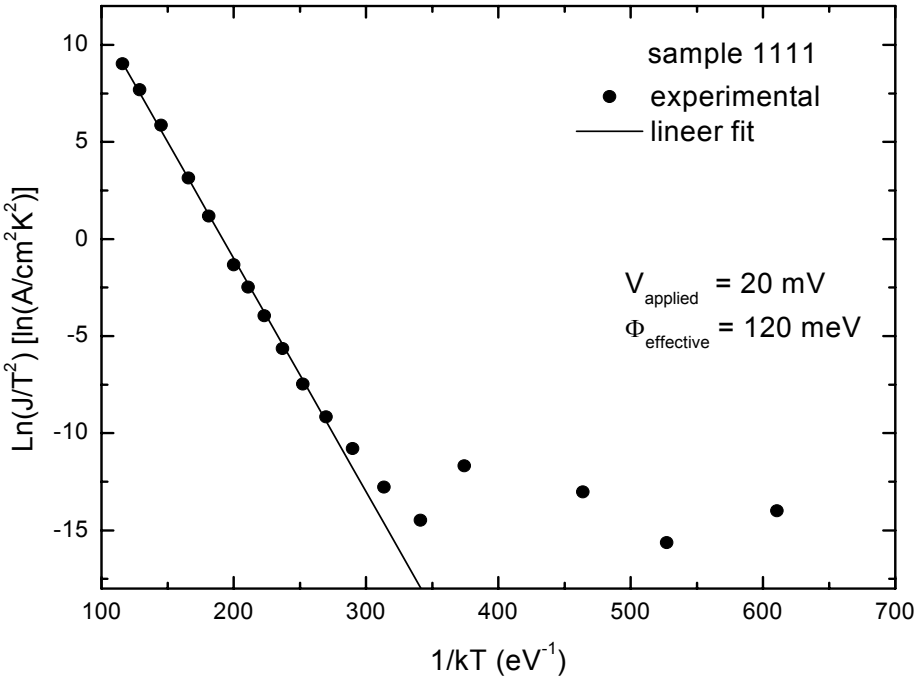

Fig. 4.6 Activation energy plot for determination of barrier height.

CHAPTER 5

INTERNAL PHOTOEMISSION SPECTROSCOPY FOR PtSi/p-Si INFRARED DETECTORS

Internal photoemission spectroscopy (IPS) is an efficient technique in studying the opto-electronic properties of a metal-semiconductor junction. The barrier height determined from an IPS measurement is more reliable than other techniques because it does not usually suffer from non-ideal contributions. On the other hand, the measurement procedure and the experimental setup are more complicated than others. Delicate instrumentation and careful light handling are required especially when the interested spectrum lies in the infrared region.

PtSi/p-Si Schottky diodes serve as infrared detectors in 3-5 μm atmospheric window. In spite of their low quantum efficiency, PtSi/p-Si junctions have been successfully used in the infrared imaging systems [96,97]. The process compatibility with the existing Si technology has made them possible to integrate PtSi-Si diodes to the existing microelectronic technology. Thus, the electrical [98] and optical [26,58,99-102] properties of PtSi/p-Si junctions have been subject of investigation. The modified Fowler theory is commonly used to find the Schottky barrier height (i.e. the cut-off wavelength of the detector) of these diodes. It is, however, known that this approach does not agree with the experimental results especially for photon energies close to the barrier height of the Schottky junction [61]. The barrier height values extracted by this approach are usually greater than the actual value [61]. Several studies have been reported on a complete theoretical formulation of the internal photoemission in metal-semiconductor junctions,

particularly in PtSi-Si diodes [59-61,103]. Mooney and Silverman [61] improved the modified model by taking all possible scattering mechanisms in the thin PtSi layer into account. However, this theoretical model has not been widely used due to the simplicity of the common form of the Fowler approach. A comparative study is then needed to test the validity of the extended model. Additionally, the features of the internal photoemission spectrum of PtSi-Si diodes in the whole range of the atmospheric window (3-5 μm) are not well studied. A loss of photoresponse is usually observed in the high-energy side of the window (~3 μm -0.4 eV-) [26,101,103,104]. This loss was attributed to parasitic barrier heights present at the junction [104]. The same behavior was also observed for other detector structures such as SiGe/Si heterojunctions [30,86], GaAs quantum wells [105] and $IrSi_3$/Si Schottky diodes [106].

This chapter presents the properties of internal photoemission in PtSi/p-Si. Theoretical model and the results were discussed in chapter 2 for heterojunctions. The model is adapted to metal/semiconductor systems and its comparison with the experimental results is given in this chapter. The effects of various experimental conditions are also reported. Part of this chapter has been published and can be found in [76].

5.1 Internal Photoemission in Metal/Semiconductor Systems

In this section, instead of setting up the model for metal(silicide)/semiconductor internal photoemission infrared detector systems from the beginning, different points from the HIPs will be introduced to the model presented in chapter 2, since the operation mechanism in both structures is the same.

Fig. 5.1 shows the detailed energy levels in metal/p-semiconductor band structure. Since the 0 eV energy reference point is different (bottom of the conduction band of the metal film), and the energy of the absorbed photon ($h\nu$) is less than the Fermi energy (E_F), distribution of excited electrons can be written in momentum space only as

$$k(E_F - h\nu) < k < k(E_F) \tag{5.1}$$

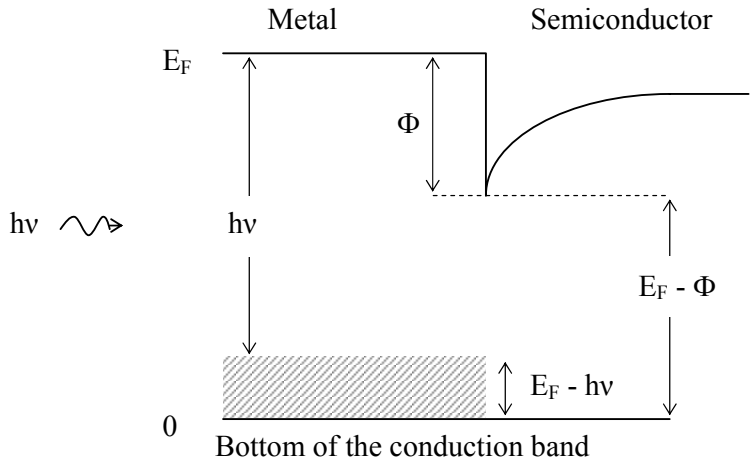

Fig. 5.1 Energy levels in metal-semiconductor band structure.

From the conservation of total energy, the equivalence of Eq. (2.4) which determines the escape volume in momentum space is written as

$$\frac{\hbar^2 k_\perp^2}{2m_m} + \frac{\hbar^2}{2}\left(\frac{1}{m_m} + \frac{1}{m_s}\right)k_{//}^2 \le E_F - \Phi \tag{5.2}$$

where m_m and m_s are the effective masses in the metal film and the Si substrate respectively. As seen from Eq. (5.2), the equality is satisfied for an ellipsoid of revolution in k-space no matter what effective masses' magnitudes are. Thus, the states which will emit are shown as hatched region in Fig. 5.2. This region is known as the 'escape cap'. For the escape cap

$$k_{\min} = k(E_F - h\nu)$$

$$k_{\max} = k(E_F - \Phi) \tag{5.3}$$

The yield can then be written from the volume ratio of the escape cap and the shell of excitation as

$$Y_F = \frac{V_c}{V_{shell}} = \frac{M\left(E_F - \Phi\right)^{3/2} + \left[E_F - \left(1+M\right)h\nu + M\Phi\right]^{3/2} - \left(1+M\right)\left(E_F - h\nu\right)^{3/2}}{2\left(1+M\right)\left[E_F^{3/2} - \left(E_F - h\nu\right)^{3/2}\right]} \tag{5.4}$$

In the limit that $E_F >> h\nu >> \Psi$ the yield is approximately

$$Y_F = M^{1/2}\frac{\left(h\nu - \Phi\right)^2}{8E_F h\nu} \tag{5.5}$$

Eq. (5.5) is known as the modified Fowler equation and traditionally used in the analysis of the junction.

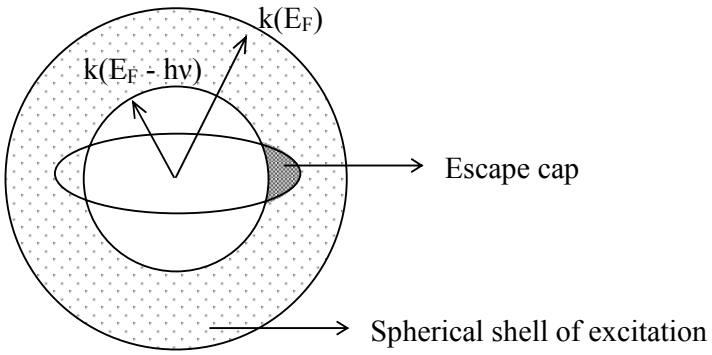

Fig. 5.2 Escape cap for holes in momentum space. The hatched region corresponds to the holes that may escape over the barrier.

This model only differs from the model presented in chapter 2 in the calculation of the maximum yield while incorporating the scattering mechanisms into it. By using the fact that $E_F > \Phi$ and $E_F > h\nu$, the maximum yield is written as

$$Y_\infty = \frac{h\nu - \Phi}{h\nu} \tag{5.6}$$

As a result, for M = 1, $E_F >> h\nu > \Phi$, and neglecting the quantum mechanical reflections, the partial yield Yn term in Eq. (2.36) is reduced to

$$Y_n = \frac{L^* U(d/L^*)}{8dE_F h\nu}\left(h\nu - n\hbar\omega - \Phi\right)^2 \tag{5.7}$$

where

$$U(d/L^*) = \left[\ \alpha + e^{-d/L^*}\beta\left(1 + \delta + \delta^2 + \delta^3 + \cdots\right)\ \right]/L^* \tag{5.8}$$

5.2 Experimental Details

PtSi/Si diodes were fabricated on p-type (100) Si substrates with a resistivity of 25-30 Ωcm. The samples were first cleaned by using a standard RCA cleaning process. Then they were immediately loaded into a vacuum chamber for the Pt evaporation process. A 50 Å thick Pt film was deposited on the sample's surface by e-beam evaporation at a rate of 1.5 Å/sec (UNIVEX 450 system with an e-beam gun ESV4). In this process a metal shadow mask with circular openings of a diameter of 1 mm was used to define the active regions. The base pressure of the chamber before the evaporation was $1x10^{-6}$ Torr; it dropped to $1x10^{-5}$ Torr during evaporation. The PtSi film was formed by annealing the samples at 675 °C for 30 minutes under N_2 atmosphere. This high annealing temperature was used to reduce the oxygen related problems in the PtSi film formation [107]: Under this temperature the reaction between Pt and Si can be too rapid to trap both unreacted Pt and Pt_2Si in the PtSi lattice. And it is also known that high annealing temperature does not cause the film of poor quality [108]. The samples were finally fixed on a sample holder that can be mounted into a closed cycle He cryostat with a special window which allows infrared light to reach the sample surface. The electrical contacts to the samples were taken from the implanted guard ring and from the backside as shown in Fig. 5.3.

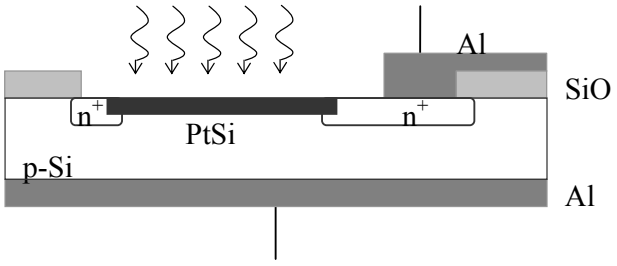

Fig. 5.3 Cross-section of the PtSi/p-Si diodes.

The experimental set-up for the internal photoemission measurements is shown in Fig. 5.4. A globar IR source is used for illuminating the sample. Before entering the monochromator (ORIEL, MS257) the light is filtered with a long pass filter with a cut-on wavelength of 2.35 μm. By using a mirror system a small fraction of the monochromatic light at the exit of the monochromator is directed onto a pyroelectric reference detector. The undeflected part of the light illuminates the photodiode mounted on the sample holder in the cryostat (Cryophysics). The signals from the pyroelectric detector and from the PtSi/p-Si diode are measured by using a radiometer (ORIEL, Merlin) and an electrometer (Keithley, 6517), respectively. The measurements are controlled and recorded by a personal computer.

The yield of a photodiode is defined as the ratio of the number of photoelectrons to that of incident photons. While the number of photoelectrons was determined directly from the measured photocurrent, that of incident photons was estimated by measuring the light falling on the sample from a calibrated pyroelectric detector. The amount of light transmitted through the sample was determined by measuring the transmission spectrum through the sample. The ratio between the reflected and absorbed light was estimated from previously reported results [62].

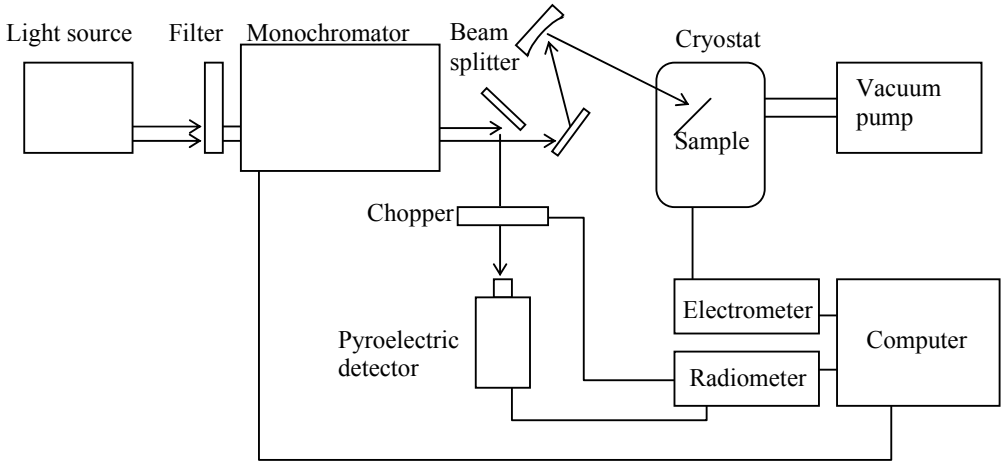

Fig. 5.4 Optoelectronic spectrum measurement system.

5.3 PtSi/p-Si Spectrum

Fig. 5.5 shows the internal photoemission spectrum of a PtSi/p-Si diode at 70 K. The dip seen at 0.4 eV (~3 μm) results from the absorption of the incident light by the thin ice layer formed on the sample during the cooling process and will be discussed in the following section. When a straight line (dashed line in the graph) is fitted to the linear portion of the curve, the barrier height is found to be 0.274 eV. This value of the barrier height is higher than what is usually obtained from I-V measurements (~0.25eV) [98]. The traditional Fowler theory (Eq. (5.5)) relies on ballistic transport of photo-excited carriers and ignores their interaction with phonons, other carriers and film walls. It then overestimates the barrier height of the junction [61]. As seen in Fig. 5.5 the experimental points do not follow the straight line of Eq. (5.5) especially for energies close to the barrier height. This commonly observed feature of the curve is due to the effect of multiple reflections of the excited holes from the surfaces of the silicide film and that of collisions with phonons, imperfections and cold electrons. The solid line in the graph represents the theoretical internal yield of Eq. (2.36) with Eq. (5.7). In the calculations, Eq. (5.8) was approximated by $[1 - \exp(- d/L^*)]^{1/2}$ [59]. Scattering by phonons and electrons and by the film walls, and the energy lost during electron-phonon collisions are thus taken into account. In the fitting process, L_p, L_e, and $\hbar\omega$ were used as adjustable parameters. For the result showed in Fig. 5.5, L_p=60 Å, L_e=2000 Å, $\hbar\omega$=0.006 eV. These values are within the ranges suggested for holes in PtSi [61]. As shown in Fig. 5.5, a perfect fit to the experimental data was obtained for the whole spectrum except for the dip region. The nonlinear part below 0.35 eV is well accounted for by this model. The barrier height used in this fitting is 0.244 eV which is consistent with the reported values for PtSi-Si junctions [98]. One can then conclude that the extended theoretical approach that takes the scattering mechanisms into account provides a more consistent explanation for the internal photoemission process. We should, however, note that the result of extended theory is not unique because of too many adjustable parameters involved in the calculations such as L_p, $\hbar\omega$, and L_e. Unfortunately, reliable values for these parameters are not available, and they are not easily measurable quantities. Some speculative estimations are available in the

literature. We used these estimations in our calculations and obtained consistency in the results.

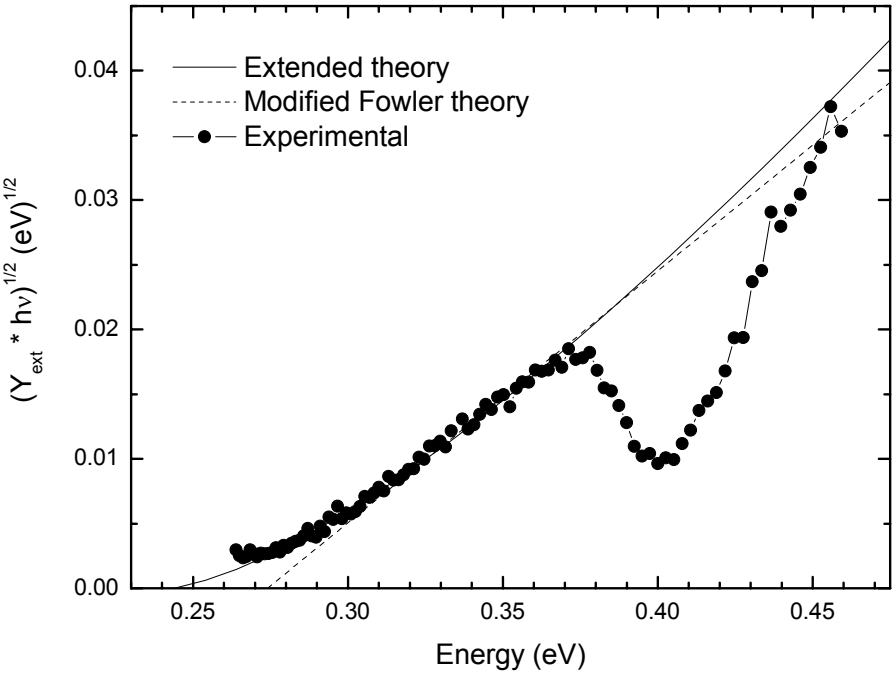

Fig. 5.5 Internal photoemission spectrum of the PtSi/p-Si diode. Curves fitted by modified Fowler theory and extended theory are also shown.

5.4 Effect of the Ice Formation on the Detector's Response

In the internal photoemission spectrum of a PtSi/p-Si diode shown in Fig. 5.5 a dip is seen at about 0.4 eV (~3 μm). The position of the dip along the horizontal axis is same in all measurements but its depth varies under different experimental conditions. The same dip was also observed in similar experiments by others [26,30,86,101,103-106]. However, either they ignored the presence of the dip because this would not affect the results of their work [26,30,86,101,103,106] or speculated on the reason for the incongruity [104,105]. The same spectral dip at around 3 μm is seen in many devices having different materials and structures. Among them there are Schottky devices using Pd_2Si [26,104], $IrSi_3$ [106], SiGe/Si heterojunction infrared detectors [30,86] and GaAs based quantum wells [105]. We have shown that the foregoing dip in the spectrum is due to the formation of thin ice layer on surface of the detector during the cooling process.

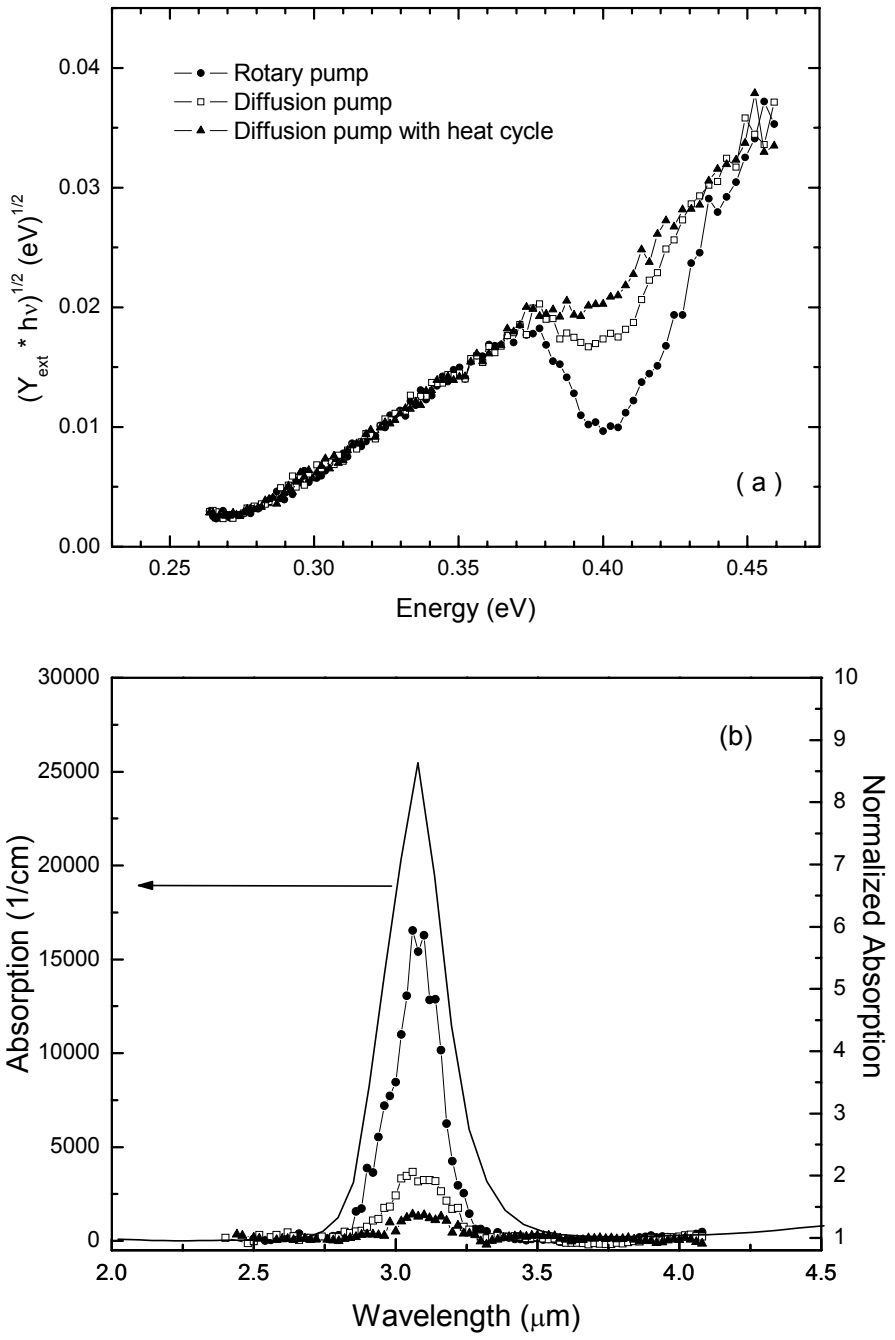

Fig. 5.6 a) Effect of different vacuum conditions on the internal photoemission spectrum of the PtSi/p-Si diode. b) Direct comparison of the observed dip to the spectrum of the ice taken from Ref. [109]. (Experimental data are normalized against the theoretical response curve). The solid line (ice's absorption spectrum) belongs to the left axis and the others (experimental data) belong to the right axis. Marker types are same as (a).

In order to see how this loss in the photoresponse is related to the detector's ambient, the experiment was repeated by using different vacuum conditions. For the case in which a mechanical (rotary) pump was used, the starting pressure during the cooling down process was about $1x10^{-2}$ Torr. In the other case a diffusion pump with a liquid N_2 trap, which provided a starting pressure of $1x10^{-4}$ Torr, was used to evacuate the system. The internal photoemission spectra obtained for these conditions are displayed in Fig. 5.6a. It is seen that the depth of the dip is considerably reduced when a diffusion pump is employed. In the last experiment, the sample was first cooled down to 70 K and then heated quickly up to 300 K and cooled down again without breaking the vacuum created by the diffusion pump. In this cycling process, the sample is locally heated while the cryostat's body is still at very low temperature. The water condensed on the sample's surface is then expected to be evaporated from the sample and captured by the cryostat's cold body which acts as an effective cryopump. The internal photoemission spectrum of the diodes obtained after this cycling process is shown in Fig. 5.6a. It is seen from this spectrum that the dip at 0.4 eV is further reduced with this heat-cool cycle. In addition, when the position of the dip is compared with the absorption spectrum of the ice, a correlation between the spectra is clearly seen. Fig. 5.6b shows the comparison of the ice's absorption spectrum [109] with the detector's response normalized against the theoretical curve fitted nicely to the experimental data (see Fig. 5.5). It is seen that the spectrum of the ice has a strong absorption peak at 3.078 μm and this coincides exactly with the observed dip in our experiments. This indicates that the observed loss in the photoresponse resulted from the absorption in the ice layer formed on the detector's surface. The incident light is partly absorbed in this ice layer before reaching the surface of the diode. Taking the peak absorption coefficient as $k=2.5x10^{-4}$ cm^{-1}, the thickness of the ice layer can roughly be estimated to be 0.1-0.8 μm from the normalized curves shown in Fig. 5.6b. The amount of the ice would of course depend on the quality of the vacuum and the relative speed of the cooling process for the parts of the cryostat's cold stage.

We proved the presence of the same ice effect on the detector's spectrum for GaAs-based quantum well systems in another study [110]. It was shown that the

speculated double peak behavior was not actually two peaks but one peak and one dip superimposed on each other. It was again seen that when the detector Dewar was evacuated more effectively, the dip was almost disappeared.

5.5 I-V Characteristics of PtSi/p-Si Diodes

Even though it has several drawbacks, determination of the Schottky barrier height from the I-V measurements is a widely used technique in this area. We have mainly focused on the internal photoemission of the PtSi/Si Schottky junction in this work. I-V measurements provided supplementary results on the electronic structure of PtSi/Si interface.

Fig.5.7 shows both forward and reverse bias characteristics of the PtSi-Si diode. The overall characteristics of the diode are consistent with what is expected for this diode. Due to the low Schottky barrier height PtSi/Si junction is an ohmic contact with a low junction resistance at room temperature. In order to see its rectifying properties and the diode action, it should be cooled down to a certain temperature below which the carriers do not have enough thermal energy to surmount the barrier from the metal side to the semiconductor side. This is why the PtSi/Si infrared detectors should be cooled down to observe their detector action. An exponential dependence and a rectification were observed below 100 K in the diodes used in this work. The barrier height and ideality values were determined below this temperature only.

In the extraction of the barrier height and the ideality factor, the thermionic emission theory was used and all other current mechanisms were ignored. The thermionic emission current is given by

$$I_{th} = AA^{*}T^{2} \exp\left(-\frac{\Phi}{kT}\right) \exp\left(\frac{qV}{nkT}\right)$$

$$I_{th} = I_{sat} \exp\left(\frac{qV}{nkT}\right) \tag{5.9}$$

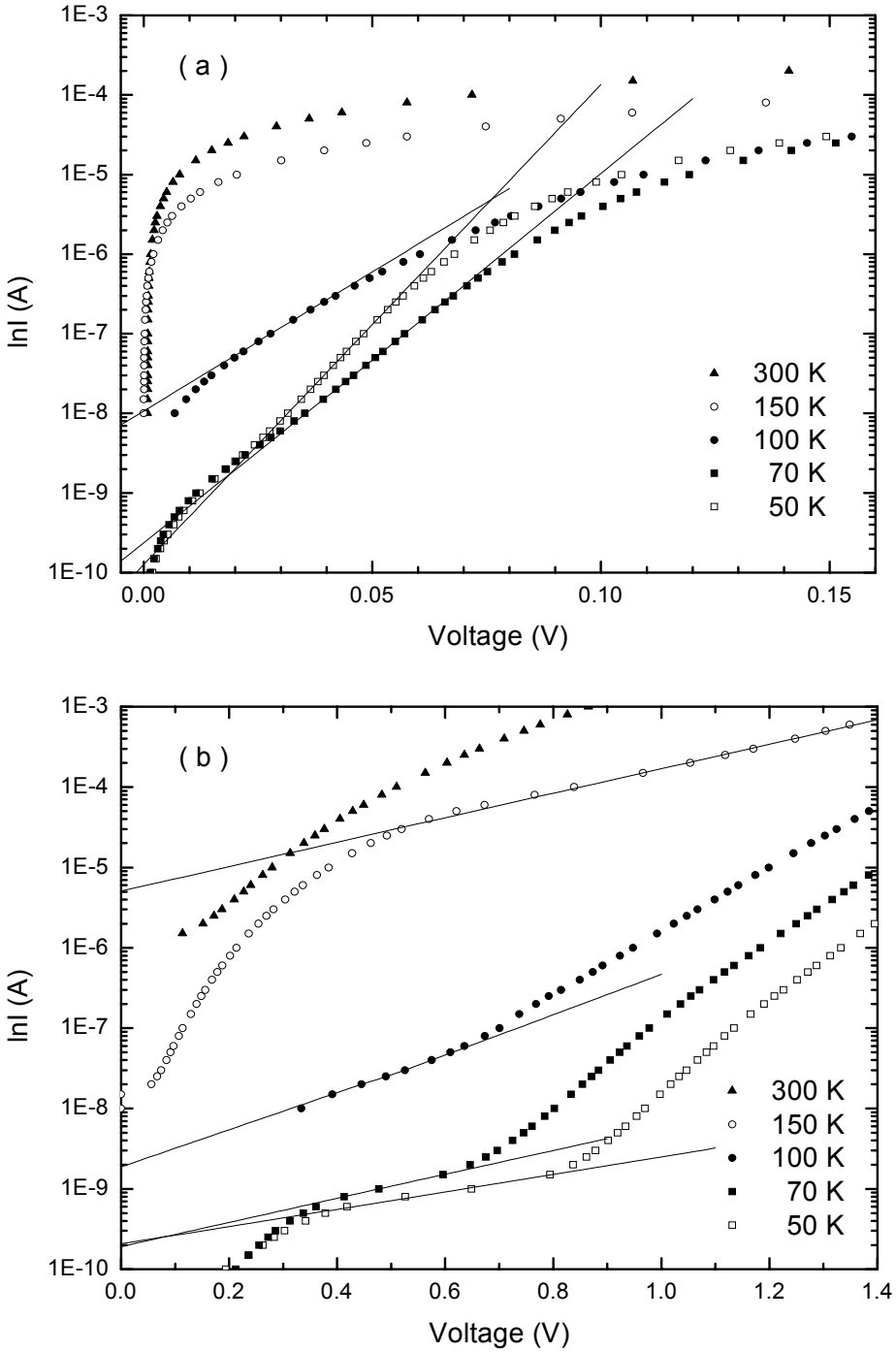

Fig. 5.7 I-V characteristics of the PtSi/p-Si diode at different temperatures for (a) forward and (b) reverse bias. Fitted lines for the extraction of the barrier height and the ideality factor are also shown.

where V is the applied voltage, A is the diode area, A^* is the effective Richardson constant and n is called the ideality factor accounting for other current mechanisms. In the analysis of the reverse I-V characteristics, the equation

$$I'_{sat} = I_{sat} \exp\left(\frac{cV^{1/4}}{kT}\right) \tag{5.10}$$

was used and done by plotting lnI vs $V^{1/4}$ plot as shown in Fig.5.7b. The results are displayed in Table 5.1. We see that the Schottky barrier height values determined both from reverse and forward characteristics at 100 K are close to what is expected for a PtSi/Si junction. Also the ideality factor is close to unity for this temperature. The barrier height decreases and the ideality factor gets higher values as temperature decreases. This behavior is typically observed in the non-ideal Schottky junctions. The reason is that other current mechanisms such as tunneling and recombination current become more important as the temperature is reduced and the thermionic current is suppressed. It is then reasonable to assume that the Schottky barrier height determined at higher temperatures are closer to the true value. This is consistent what we have obtained in the I-V measurements.

Table 5.1 Barrier height and ideality factor (n) values extracted from I-V analysis of PtSi/p-Si diodes at various temperatures.

	FORWARD			REVERSE		
Temp (K)	100	70	50	100	70	50
BH (eV)	0.24	0.186	0.132	0.253	0.189	0.130
n	1.285	1.546	1.66	-	-	-

The barrier height values of PtSi/p-Si obtained by I-V analysis and internal photoemission spectroscopy (IPS) analysis are displayed in Table 5.2. The difference between the barrier heights found by using the Modified Fowler theory and using the extended theory is due to the multiple reflections of the excited holes from the surfaces of the metal film and the collisions with phonons and imperfections as discussed before. As a result of these processes, hot holes, which

have initially no chance to be captured, are redirected to the interface and pass through the barrier. Thus, the yield increases. This increase in the yield makes the aforementioned difference in the analysis.

When one compares the optical and the electrical barrier heights, it is obvious that there is an excellent agreement between them. And consequently it can be concluded that the analysis of the internal photoemission spectroscopy by using the extended model yields the most accurate values for the barrier height.

Table 5.2 Barrier height values of PtSi/p-Si obtained by I-V analysis and internal photoemission spectroscopy (IPS) analysis.

	I-V		**IPS**	
	Forward	Reverse	Extended	Modified
BH (eV)	0.24	0.253	0.244	0.274

CHAPTER 6

InGaAs/InP QUANTUM WELL INFRARED PHOTODETECTORS

Modern growth techniques allow the fabrication of low-dimensional semiconductor heterostructures of almost any desired design: from two- and one-dimensional (quantum wells and wires) down to zero-dimensional (quantum dots). These structures are of high interest due to their technological potential, ranging from commercially available devices such as solid-state lasers and detectors based on quantum wells, up to more advanced goals such as using quantum dots to build a quantum computer.

A common feature of all these systems, which makes them different from the structures mentioned in the previous chapters, is their quantization of valence and conduction band into discrete levels. This causes an effective confinement of charge carriers within the structures. In quantum wells, for instance, carriers can move freely within a plane, but the motion perpendicular to it (i.e. the growth direction) is quantized into so-called subbands. Note that, there was no restriction on the carriers in SiGe/Si and PtSi/Si structures mentioned before; they were free to move in all directions. As in the extreme case of a quantum dot, all degrees of freedom are quantized, and the system has an atomic-like density of states. The density of states (DOS) is an important concept in the device performance since the optical response is affected fairly by the number of carriers in the structure. Fig. 6.1 shows the density of states for 0, 2, and 3-dimensional carries.

Leaving the discussion of the 0-dimensional structures' application as an infrared photodetector to the next chapter, 2-dimensional case is discussed in this chapter.

After giving the basic principles of quantum well infrared photodetectors (QWIP) in section 6.1, some experimental observations of InGaAs/InP dual-band quantum well photodetectors and their theoretical discussions are given for the rest of the chapter. Part of this chapter has been published and can be found in [111].

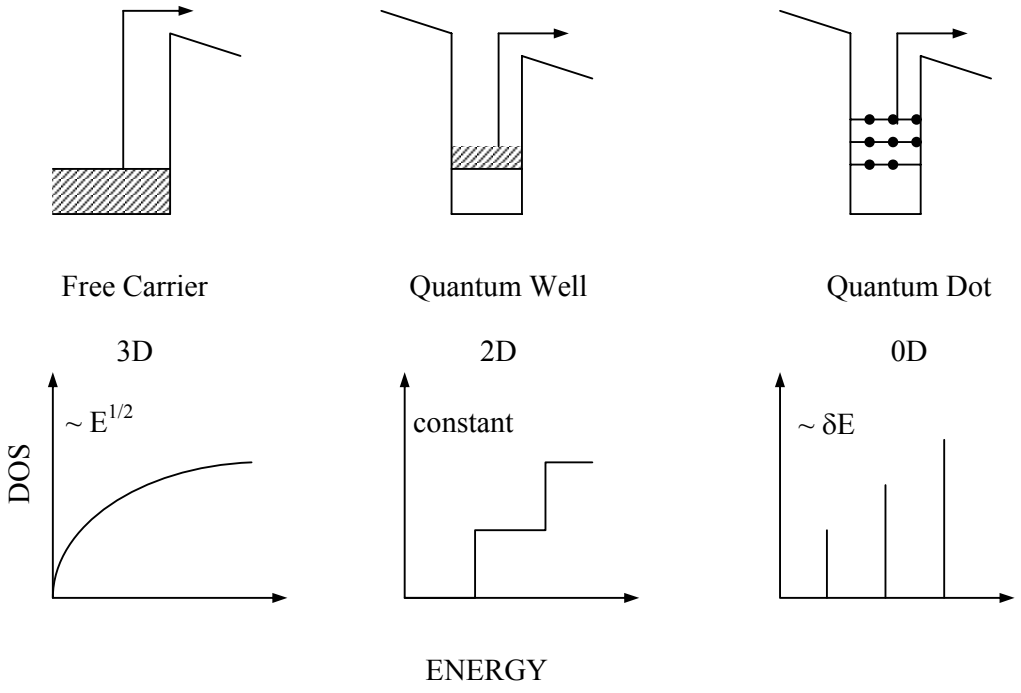

Fig. 6.1 Density of states versus energy for 0, 2, and 3-dimensional carries.

6.1 Basic Principles of QWIPs

The idea of using multiple quantum well structures to detect infrared radiation can be explained by using the basic principles of quantum mechanics. The quantum well is equivalent to the well-known particle in a box problem in quantum mechanics, which can be solved by the time-independent Schrödinger equation. The solutions to this problem are the eigenvalues that describe the energy levels inside the quantum well in which the particle is allowed to exist. The positions of the energy levels are primarily determined by the quantum well dimensions (height and width). For infinitely high barriers and parabolic bands, which is the simplest model to describe the physics, the eigenstate wavefunction and the energy levels are given by

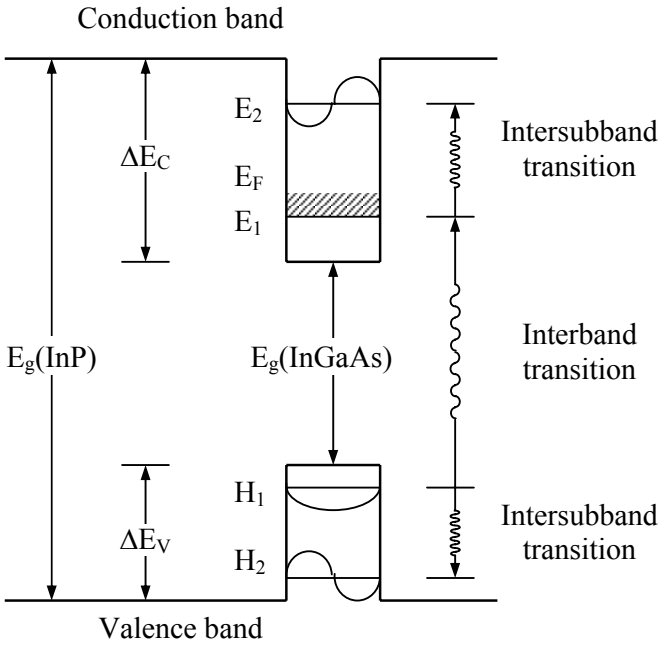

Fig. 6.2 Schematic band diagram of a quantum well showing the basics of infrared absorption: Intersubband absorption can take place between the energy levels of a QW associated with the conduction or valence band while the interband absorption is between the bands.

$$\psi_n(z,\vec{k}_{xy}) = \sqrt{\frac{2}{L_w A}} \sin\left(\frac{n\pi z}{L_w}\right) \exp\left(i\vec{k}_{xy}\cdot\vec{x}\right) \tag{6.1}$$

$$E_n(\vec{k}_{xy}) = \frac{\hbar^2\pi^2 n^2}{2m^* L_w^2} + \frac{\hbar^2 k_{xy}^2}{2m^*} \tag{6.2}$$

where L_w is the well width, A is the normalization area in the x-y plane, n is a positive integer, $\vec{k}_{xy}$ is the in-plane wave vector, and m^* is the effective mass in the well. The well is situated from $z = 0$ to $z = L_w$. For a given quantized state, one can put many electrons occupying different in-plane momenta, which leads to a Fermi energy determined by 2D quantum well density of states. Therefore, a QWIP utilizes the photoexcitation of an electron (hole) between the ground state and the first excited state in the conduction (valence) band (see Fig. 6.2). It can also utilize

the transition between the bands. Depending on the position of the first excited states, transitions are labeled as bound-to-bound (B-B), bound-to-quasi bound (B-Q), and bound-to-continuum (B-C) when the excited state is within the well, at the well and pushed out the well, respectively.

6.2 InGaAs/InP Dual-Band QWIP

Quantum well infrared photodetectors (QWIPs) [43,81] have become a standard technology for infrared detection and imaging applications over the past decade [112]. As the band structure of a QWIP can be accurately designed and controlled, some multicolor and multispectral devices have been implemented [81]. Most of these devices cover mid-infrared (MIR) and far-infrared (FIR) spectral regions. For some applications, it is desirable to have a detector working not only in MIR or FIR but also in the visible and near infrared (NIR) regions. In this regard, InGaAs/InP [113] and GaAs/AlGaAs [114] based dual-band quantum well photodetectors for the detection of NIR/MIR and visible/MIR radiation, respectively, have been reported. The idea of *dual-band* operation is straightforward: While the intersubband electron (or hole) transitions are used for MIR detection, visible/NIR radiation is detected by means of interband transitions. In this chapter, the dual-band detection with the intersubband part having both bound-to-bound and bound-to-continuum transitions for the InGaAs/InP materials system are further demonstrated. Therefore, it has been determined that the parameters for designing optimal QWIPs for this materials system, completing the original demonstration on an un-optimized InGaAs/InP structure [113]. In addition, regarding the device physics of QWIPs, most issues have been adequately resolved [81]. However, we don't yet fully understand the responsivity versus voltage characteristics especially for high-applied fields. The observed responsivity saturates for some samples (for example in [114]) while increases exponentially-like for other samples (for example in [113]). Early results were attributed to an avalanche multiplication process due to intraband impact ionization [43]. As another point of the study, experimental results of both responsivity and noise measurements and analyze the data using the theory in [115] are presented.

6.3 Experimental Details

Two samples, labeled as 235 and 236, were grown on semi-insulating InP substrates by chemical beam epitaxy. Both consist of 20 periods of InGaAs wells and InP barriers with InP top and bottom contacts of 500 and 800 nm, respectively. The targeted In content is 53%, i.e., the InGaAs is lattice matched to InP. The contacts were doped with Si to $1.5x10^{18}$ cm^{-3}. Sample 235 (236) has 6.6 nm (6.0 nm) n-type InGaAs wells and 31.2 nm (30.2 nm) undoped InP barriers. The wells were doped with Si to $3x10^{11}$ cm^{-2} by center δ doping. X-ray and photoluminescence measurements were done on the two wafers. The layer thicknesses given above have been slightly refined according to the X-ray result. The PL measurement indicates that sample 235 probably has a lightly lower In content than that for 236, by about 2%. A schematic energy band diagram of the device under bias is shown in Fig. 6.3a. Mesa devices of 400x400 and 600x600 μm^2 in sizes were fabricated with NiGeAu top ring contacts to allow normal incidence illumination for NIR detection. A 45^o edge facet was polished for light coupling to the intersubband transitions [42] (Fig. 6.3b). For spectral photoresponse measurements a closed cycle helium cryostat with KBr window and a Bomem DA8 Fourier transform spectrometer were used. For the MIR region a globar infrared source and a KBr beamsplitter were used, while for the NIR region a quartz halogen source and a quartz beamsplitter were used. All photoresponse measurements were performed at a cryostat temperature of 77 K. The MIR responsivity calibrations were done using a 1000-K blackbody infrared source, with the excitation wavelength selected by a variable narrowband filter. A quartz halogen source and a grating monochromator with a long pass filter were used to make NIR responsivity calibrations. Noise measurements have been performed using the method of [116].

6.4 Spectral Photoresponse

Fig. 6.4 shows the normalized spectral photoresponse curves for both MIR and NIR regions. MIR curves correspond to the transition from the confined quantum well state E1 to confined state E2 for sample 235 (i.e. bound-to-bound:B-B) and to the continuum states for sample 236 (i.e. bound-to-continuum:B-C). The spectral width

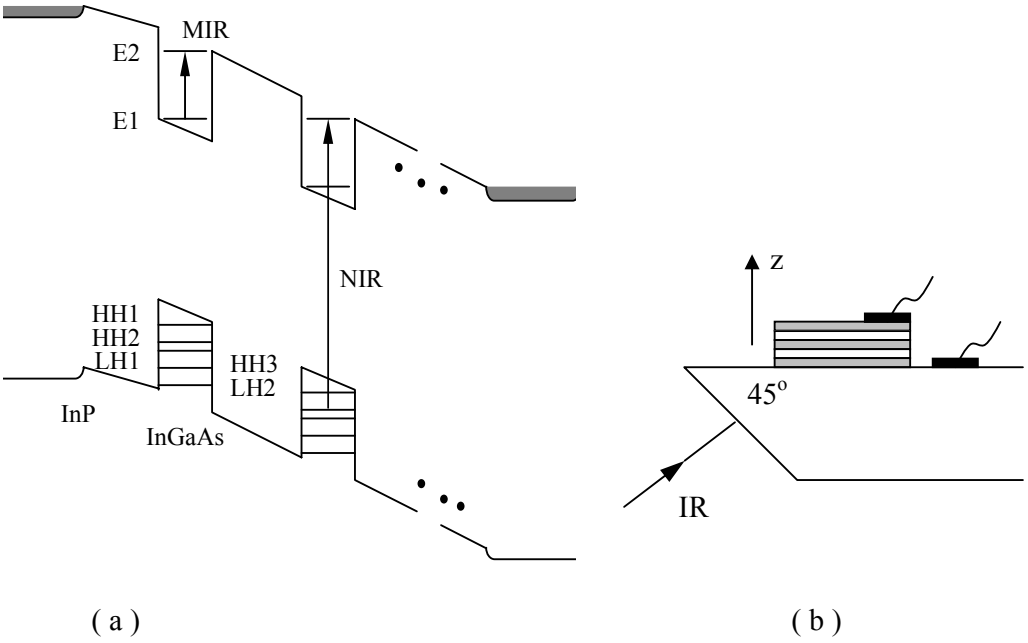

Fig. 6.3 a) Schematic energy-band diagram of the device used here under bias. The arrows indicate the processes for dual-band detection. b) 45° facet measurement geometry for the light coupling.

of B-C transitions (sample 236) is substantially wider than that of B-B transition (sample 235) and the peak position is shifted to a higher energy [117,118]. The MIR response band centered at about 9.4 μm (0.132 eV) and 8.6 μm (0.144 eV) for samples 235 and 236, respectively. By considering the confined quantum well states in both conduction and valence bands, labeled as HH1 and HH2 for the heavy hole, and LH1 and LH2 for the light hole valence band, all features in the NIR part of the graph can be accounted for [113]. The large turn-on at about 1.01 eV for sample 235 and 1.06 eV for 236 is due to the onset of HH2 to E2 transition. The small step below 0.9 eV is due to the weak signal of HH1 to E1 and LH1 to E1 transitions. The sharp cut-off at 1.4 eV is due to the absorption of the incident light in the InP substrate because of the backside illumination measurement geometry through the 45° facet. Under normal incidence through the top window, for NIR detection, spectra are broader in the higher energy region (with a drop coming from the InP top contact at ~1.4 eV) because of the contribution of the photoexcited carriers within the barrier region. Moreover, one could replace the InP top contact with

wider band-gap materials such as InAlAs or InAlAsSb, leading to a wider spectral response in the shorter wavelengths.

We can make a simple effective mass calculation to compare with the spectral features in Fig. 6.4 [117,119]. The following parameters are used: InGaAs/InP electron effective mass m_e = 0.041/0.08, InGaAs/InP heavy hole effective mass m_{HH} = 0.45/0.6, InGaAs/InP light hole effective mass m_{LH} = 0.052/0.089, conduction/valence band offset $\Delta E_{C/V}$ = 0.21/0.38 eV, and the bandgap of InGaAs (at 77 K) $E_{g,InGaAs}$ = 0.82 eV. We concentrate on sample 236 because 235 may be slightly lattice mismatched. The results of the calculation are indicated in Fig. 6.4 by arrows pointed to the expected transition positions. Note that the effect of the non-parabolic conduction band is included in the calculation with the non-parabolicity parameter α = 1.24 eV^{-1}. Note also that E2 is a virtual state in resonance with the top of the barrier.

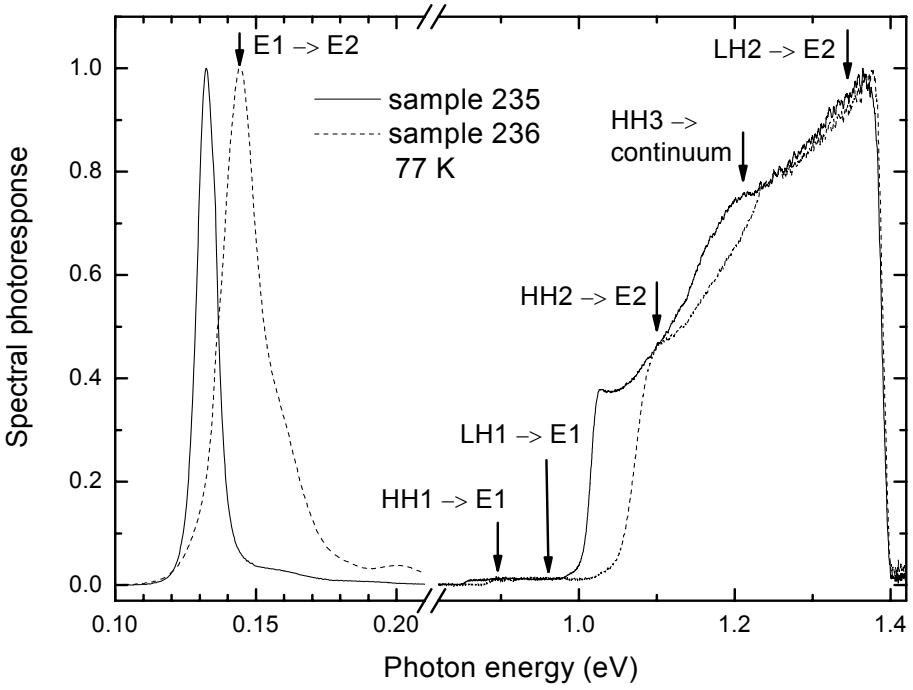

Fig. 6.4 Spectral photoresponse curves for samples 235 and 236 at device temperature of 77 K. The two parts are separately normalized. The spectral shapes are insensitive to the bias values and voltages in the range of 2 – 3 V are used for the curves shown.

6.5 Responsivity versus Voltage

The responsivity-voltage characteristics of both devices are shown in Fig. 6.5. Measurements in MIR were performed at the peak positions of the spectral photoresponse curves, i.e. at 9.4 μm for sample 235 and at 8.6 μm for sample 236 (see Fig. 6.4). For NIR calibration 0.96 μm (1.3 eV) light was used for both devices. As shown in Fig. 6.5 both devices display the same trend: a higher responsivity in MIR than that for NIR and a rapid increase in high voltage region, reaching up to 26 A/W at –3.5 V for sample 235 and 12 A/W at 3.1 V for 236. The obtained responsivity values are much higher than those for typical GaAs/AlGaAs QWIPs [118]. Since sample 235 uses bound-to-bound transitions in both spectral regions, a clear delay in the turn-on of the photoresponse as a function of voltage was observed [118]. Consistent with this assignment, sample 236 shows nearly no turn-on delay in responsivity versus voltage plot since the transitions are bound-to-continuum (Fig. 6.5b). Moreover, comparing Figs. 6.5a and 6.5b it can be seen that the absolute responsivity values for B-C transitions (sample 236) are higher than those for B-B transitions (sample 235) up to about ±3V (~23 kV/cm) because of the relatively high photoexcited escape probability. On the other hand, at higher electric fields the responsivity for sample 235 exceeds that for sample 236. This may be caused by the higher peak absorption quantum efficiency in this B-B sample than that for a B-C situation [117].

6.6 Noise and Avalanche Multiplication

The high responsivity values observed here, similar to the ones in [113] and much higher than those in standard GaAs/AlGaAs QWIPs [118], are attributed to two factors. (I) The InP barriers used here have a higher mobility than that for AlGaAs. (II) There is an avalanche multiplication process due to intraband impact ionization of electrons out of the quantum wells [43]. To quantitatively identify the contribution of the avalanche process, we performed noise measurement and carried out analyses according to the theory described in [115]. The avalanche process is described by a multiplication factor *M*, and can be taken into account by replacing

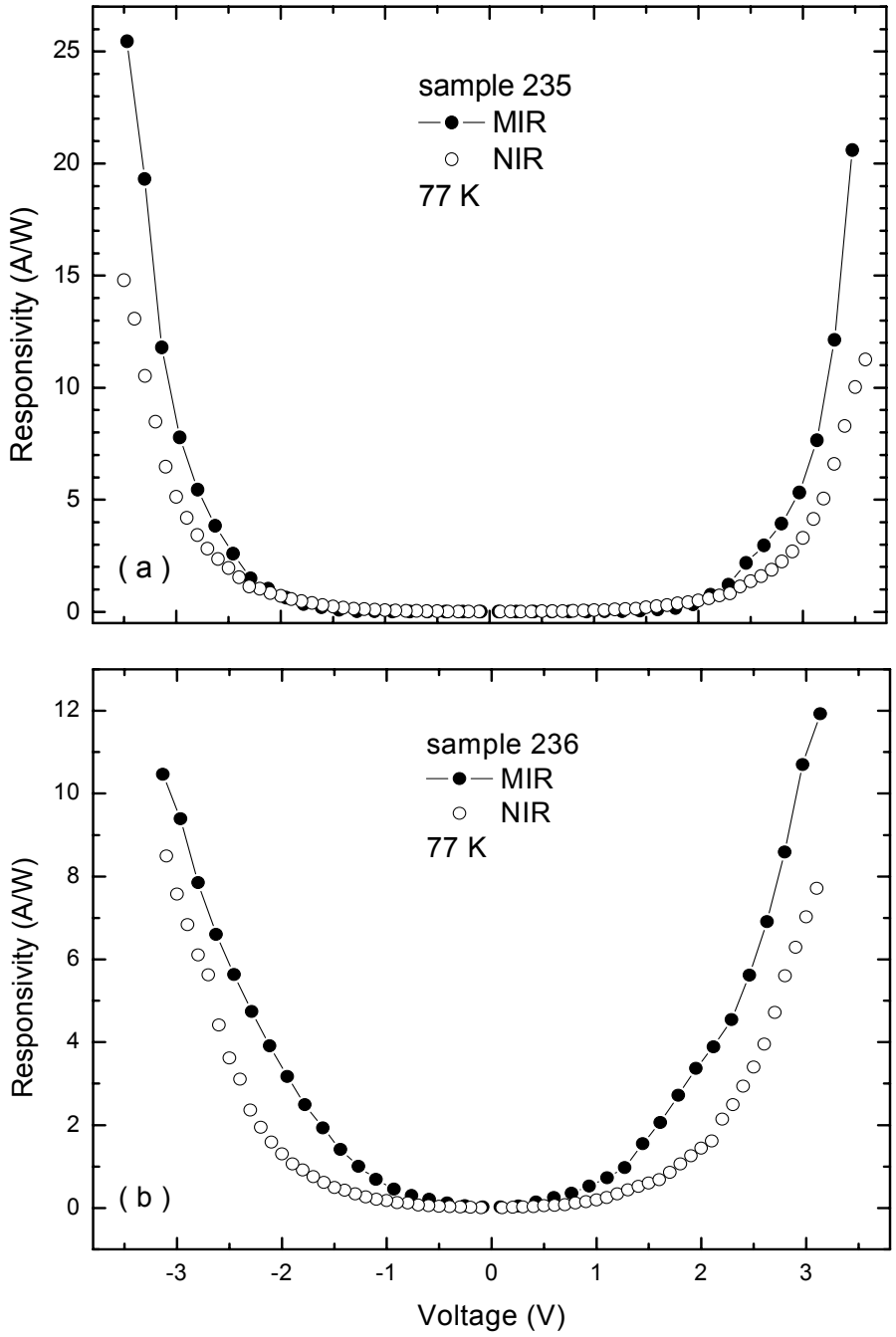

Fig. 6.5 Responsivity versus voltage characteristics of (a) sample 235 and (b) sample 236 at device temperature of 77 K. Measurements in MIR were performed at 9.4 and 8.6 μm for samples 235 and 236, respectively. For NIR calibration 0.96 μm light was used for both devices.

the photoconductive gain g_{ph} by gM. Therefore, the detector current responsivity is written as [115,116]

$$R = \frac{e}{hv}\eta g M \tag{6.3}$$

where g is the "*net*" gain that the QWIP would have in the absence of the avalanche process. Similar to [115,116], the generation-recombination noise current in the presence of avalanche multiplication is written as

$$I_{n,g-r}^2 = 4eI_d Bg MF \tag{6.4}$$

where the noise gain g_n is replaced by gMF, I_d is the dark current, B is the measurement bandwidth, and F is the *excess* noise factor. From Eq. (6.3) and Eq. (6.4), the photoconductive gain $g_{ph} = gM$ and noise gain $g_n = gMF$ differ by the noise factor F. Note that the definition of F used here differs from [115] by a factor of two.

For sample 236 the deduced photoconductive gain g_{ph} and the noise gain g_n by means of Eq. (6.3) and Eq. (6.4) are shown in Fig. 6.6, together with the dark current versus voltage characteristic. For the photoconductive gain calculation $\eta = 5\%$ was used. Up to a voltage ±1.8V (~14kV/cm) where there is no multiplication process both gain values are the same $g_{ph} = g_n = g$, and then noise gain increases more rapidly than photoconductive gain, confirming the existence of the excess noise factor *F*. The ratio of the two gains (i.e. *F*) is also plotted in Fig. 6.6. To relate the noise factor *F* to the avalanche multiplication *M* for the present unipolar photoconductor, we follow the model in [115]: $F = M - p(M - 1 + 1/2M)$, where p is the capture probability. In the limit of $p << 1$, which is true here, we have $F \approx M$. The curve in Fig. 6.6 for *F* therefore represents the magnitude of *M*. It is then implied that for low voltages ($|V|$<2 V) there is no multiplication (M=1) and at high voltages ($|V|$>2 V) the multiplication factor reaches approximately two ($M \approx 2$). It is not understood why *M* and *F*

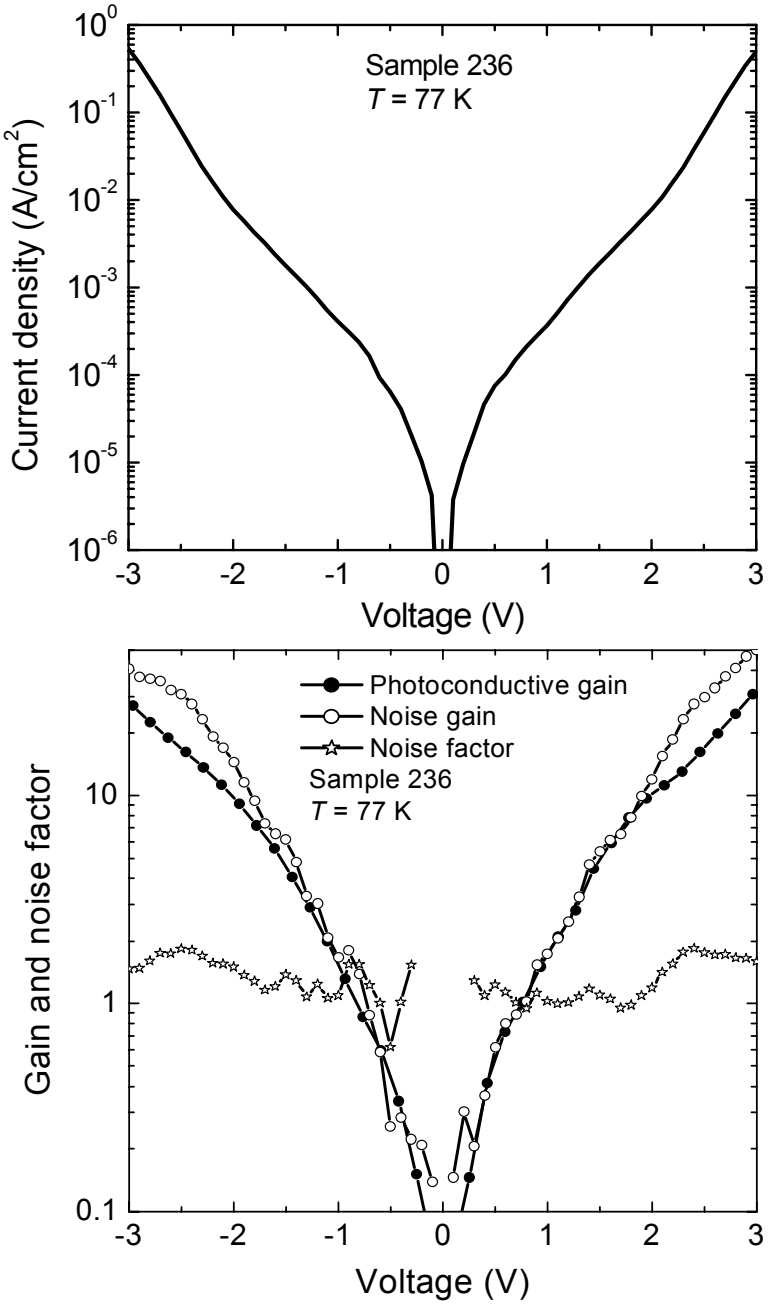

Fig. 6.6 a) Dark current (density) versus voltage characteristic, and b) photoconductive gain g_{ph} and noise gain g_n, and the ratio (g_n / g_{ph}) of the two gains versus voltage for sample 236. The latter is the excess noise factor *F* which approximately equals the multiplication factor *M*.

saturate rather than keep increasing with bias. A larger observed M and F values would have provided a stronger evidence of avalanche multiplication. It is also interesting to get a feeling of the magnitude of the impact ionization probability for an electron traversing one quantum well, labeled as q. Using the expression derived in [115] $M = p/(p-q)$, for a multiplication of $M = 2$, we have $q/p = 1/2$. We point out that the observed M of our InP-based devices is in the same range as found in InGaAs/GaAs QWIPs [116], whereas g_{ph} is about one order of magnitude higher. InGaAs/InP QWIPs thus enable high photoresponse without penalty from excess noise. The multiplication process also influences the dark current. Fig. 6.6 shows a more rapid increase in dark current for voltages larger than about $|V|>2$ V. Note that for the device sizes used here (400x400 and 600x600 μm^2) the dark current does not exceed 2 mA. In this low current regime, the measurements of responsivity and noise are reliable and are not affected by series and contact resistances.

CHAPTER 7

DETAILED CHARACTERIZATION OF A SYSTEMATIC SET OF QUANTUM DOT INFRARED PHOTODETECTORS

With the successful usage of quantum well structures for infrared photodetectors, sensors and imaging systems [43,81], the quantum dot infrared photodetector (QDIP) has attracted a lot of interest in recent years [48-50,120,121]. Among QDIPs, the most widely studied ones are made of self-assembled InAs dots on GaAs substrate.

In general, QDIPs are similar to QWIPs but with the quantum wells replaced by quantum dots. Different from quantum wells, quantum dots have size confinement in all spatial directions. Fig. 7.1a shows the schematic layers of a QWIP and a QDIP. In both cases, the detection mechanism is based on the intraband photoexcitation of electrons from confined states in the conduction band wells or dots into the continuum. The potential profile at the conduction band edge along the growth direction for both structures would have a similar shape as shown in Fig. 7.1b. In fact, it would be exactly the same if the dots were aligned in the growth direction. In practice, since the dots investigated here are self-assembled and the barriers are made thick to suppress dark current, they are not correlated between layers.

An ideal QDIP is expected to be substantially superior to QWIP. Therefore, the area of QDIP research is very active in the last couple of years. Although there have been many papers published on self-assembled QDIPs, some critical issues have not been adequately addressed and clearly resolved. In the following section, the

anticipated advantages of QDIPs with simple theoretical basis are enumerated. Then, some of the issues such as the polarization behavior and the effect of the number of electrons occupying the dots are discussed by studying a systematic set of samples with varying the doping density and hence the number of electrons. We address these issues using the simplest physical picture and neglect higher order effects such as the effect of wetting layers and the effect of random (modulation) doping and dot distributions on the photoconductive transport properties. Note that some of this chapter's content have been published and can be found in [122,123].

7.1 Anticipated Advantages of QDIPs

"*QDIPs allow normal incidence*". A limitation of QWIPs is that, due to the transition selection rules, they are not sensitive to normally incident light, and they typically only have a narrow response range in the infrared [43,124]. Note that, "normally incident light" is the light which is normal to the wafer along the growth direction. On the other hand, QDIPs do not suffer from this normal-incidence limitation because of the geometry with the carrier confinement in all three directions. The normal incidence property is advantageous because it avoids the need of fabricating a grating coupler in the standard QWIP imaging arrays [112]. Furthermore, QDIPs can have a broader infrared response range because the self-assembled dots have several discrete states [125,126]. Although normal incidence response of QDIPs has been reported in the literature [50,127-130], most of the publications do not show polarization dependence of the photocurrent spectra, and some [131-133] show dominant P-polarized response in the 45-degree facet geometry (see Fig. 6.3b). In one publication [134] on absorption measurements clear evidence of absorption features due to in-plane confined quantum dot levels was reported. The possible reason of this problem is discussed in section 7.3.

"*QDIPs have lower dark current*". Another potential advantage of QDIPs over QWIPs is the theoretical prediction of lower dark currents in QDIPs [135]. The simplest way to estimate the dark current is by the following expression [81]

$$J_{dark} = e\upsilon n_{3D} \tag{7.1}$$

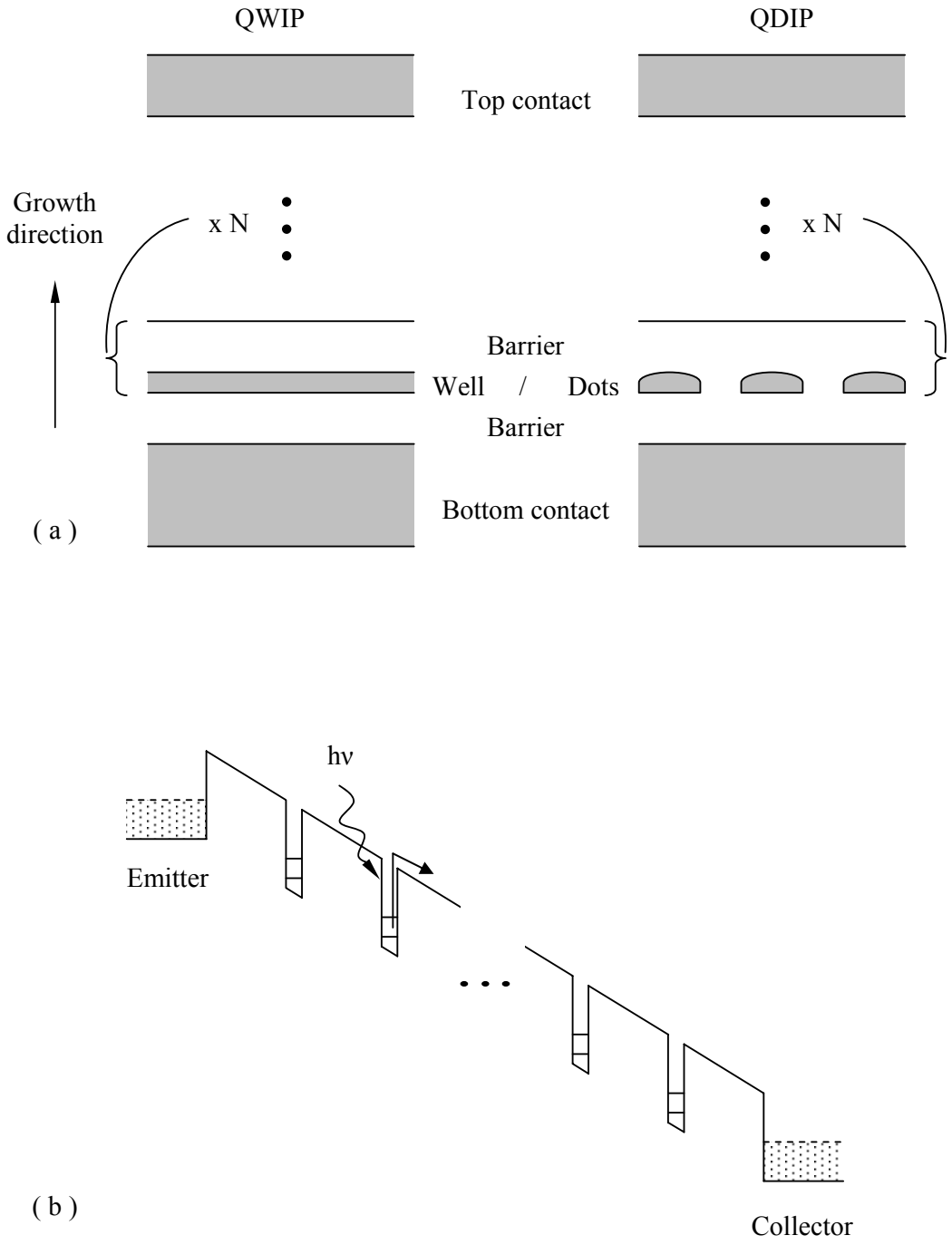

Fig. 7.1 Schematic (a) layers of a QWIP and QDIP and (b) potential profile for both structures under bias.

where υ is the drift velocity for the electrons in the barrier and n_{3D} is the three-dimensional electron density in the barrier. Note that the diffusion is neglected in Eq. (7.1). The electron density can be estimated by [81]

$$n_{3D} = 2\left(\frac{m_b k_B T}{2\pi\hbar^2}\right)^{3/2} \exp\left(-\frac{E_a}{k_B T}\right) \tag{7.2}$$

where m_b is the barrier effective mass and E_a is the thermal activation energy which equals the energy difference between the top of the barrier and the Fermi level in the well or dot. The difference in the dark current for similar barriers in a QWIP and a QDIP (i.e. υ and m_b are comparable) is then determined by the difference in E_a. If the field induced barrier lowering effect in E_a is neglected (valid for low applied fields), the activation energy relates to detection cut-off wavelength (λ_c) by

$$E_a^{QWIP} = \frac{hc}{\lambda_c} - E_F \tag{7.3}$$

for a QWIP with a bound-to-continuum detection scheme, and for QDIP

$$E_a^{QDIP} = \frac{hc}{\lambda_c} \tag{7.4}$$

where E_F is the Fermi level in the well. Thus, it can be seen from the Eq. (7.3) and Eq. (7.4) that for the same cut-off wavelength and barrier material, there is a reduction in the dark current in QDIP versus QWIP.

"*QDIPs have higher responsivity*". The final advantage relates to the potentially long excited electron lifetime, τ_{life}. It has been anticipated [136] that the relaxation of electrons is substantially slowed when the inter-level spacing is larger than phonon energy – "phonon bottleneck" [137]. If the phonon bottleneck can be implemented in a QDIP, the higher responsivity values are obtained. Because a photoconductor responsivity is given by [81]

$$R = \frac{e}{h\nu}\eta g \tag{7.5}$$

where η is the absorption efficiency and g is the photoconductive gain [81]

$$g = \frac{\tau_{life}}{\tau_{trans}} \tag{7.6}$$

where τ_{trans} is the transit time across the device. Thus, a long τ_{life} directly drives the large responsivity R.

7.2 Experimental Details

Using molecular beam epitaxy, four samples with nominally identical parameters except for the modulation delta-doping densities in the GaAs barriers were grown. Starting with semi-insulating GaAs substrates, the layers are (in growth sequence): an undoped 300-nm GaAs buffer layer, a 760-nm n^+-GaAs bottom contact layer, a 5-nm GaAs spacer layer, QDIP active region, and a 400-nm n^+-GaAs top contact layer. The active region consists of 50 layers of self-assembled InAs QDs separated by 30-nm GaAs barriers that are center modulation delta-doped with Si to populate the QDs. The top and bottom contact layers were doped to 1.2×10^{18} cm^{-3} with Si to act as reservoirs of charged carriers (electrons). Mesa devices were made using standard GaAs microfabrication techniques. The mesas were defined by wet chemical etching, and the top and bottom contacts were made by depositing Ni/Ge/Au followed by annealing.

Doping levels per QD layer for samples used in this study are: 1×10^{10} cm^{-2} (due to the background doping) for sample A, 1.5×10^{10} cm^{-2} for sample B, 2×10^{10} cm^{-2} for sample C, and 3.5×10^{10} cm^{-2} for sample D. By estimating the QD density from structural observations (from atomic force microscopy and plan-view transmission electron microscopy) on the three samples grown under the same condition, the average number of electrons per dot was calculated as 2, 5, 7 and 12 for the four samples, respectively. Table 7.1 shows the structural parameters used for

estimation. For the photoresponse measurements, 400×400-μm^2 devices were mounted in a closed-cycle helium cryostat. A Bomem DA8 Fourier transform infrared spectrometer with a globar source was used. Devices were illuminated through the 45^o polished edge facets. Data were taken with two sets of beamsplitters and windows, and corrected by background spectra. To obtain a complete spectrum, two parts were joined together by superimposing the overlapped region. The responsivity calibrations were done using a 1000-K blackbody infrared source, with the excitation wavelength selected by a variable narrowband filter. All photoresponse measurements were performed at a cryostat temperature of 6 K and no qualitative differences were seen up to ~30 K, except an increase in the noise level.

Table 7.1 Structural parameters obtained from atomic force microscopy and plan-view transmission electron microscopy observations to estimate the number of the electrons per dot.

Sample	**QD Density** (10^{10} cm^{-2})	**Doping per period** (10^{10} cm^{-2})	**Electrons per dot** (10^{10} cm^{-2})
A	0.5	1	2
B	0.3	1.5	5
C	0.3	2	7
D	0.3	3.5	12

7.3 Physical Picture

The electronic shell structure and the level separations of InAs/GaAs self-assembled QDs are determined by the dot size and shape [138,139]. In general, these self-assembled QDs are wide in the in-plane direction (~20 nm) and narrow in the growth direction (~3 nm). Therefore, the strong confinement is in the growth direction while the in-plane confinement is weak resulting in several levels in the dots [45]. Samples used in this study have disk-shaped QDs with a diameter of about 18 nm and a height of about 2.5 nm. Then, in cylindrical coordinates the Schrödinger equation can be written as

$$-\frac{\hbar^2}{2m}\left[\frac{1}{r}\frac{\partial}{\partial r}r\frac{\partial}{\partial r}+\frac{1}{r^2}\frac{\partial^2}{\partial\theta^2}+\frac{\partial^2}{\partial z^2}+V(r,z)\right]\Psi(r,\theta,z)=E\,\Psi(r,\theta,z) \tag{7.7}$$

To clearly illustrate the physical picture and as an approximation, we view the confining potential in the growth direction (chosen as the *z* coordinate) and the in-plane directions (*x*-*y*) as being separable. The former is the familiar quantum well problem. Since the height of the QDs is much smaller than its radii, the electron motion in the growth direction is strongly confined. Therefore the wavefunction of an electron may be written as [140]

$$\Psi(r,\theta,z)=\frac{1}{\sqrt{2\pi}}e^{il\theta}\psi_l^n(r)\psi_r^n(z) \tag{7.8}$$

where *n* represents the distinct subbands related to the vertical motion (n = 0,1,…). In our case the disks support only one confined level in the growth direction (ground state, n = 0) [140]. The in-plane circular shape leads to the *z*-component angular momentum being a good quantum number (l). Then, for each angular momentum l and subband index n = 0, $\psi_l(r)$ satisfy the equation

$$-\frac{\hbar^2}{2m}\left[\frac{1}{r}\frac{\partial}{\partial r}r\frac{\partial\psi_l}{\partial r}+\left(\frac{l^2}{r^2}+V_r\right)\psi_l\right]=E_r\,\psi_l \tag{7.9}$$

Analogous to real atoms, the bound states are grouped into three shells: s, p and d. The d shell has two degenerate angular momentum states, under the parabolic potential approximation, with quantum numbers l = ±2 and l = 0 [45].

For light polarized in the growth direction, *E//z*, only transitions (Δl = 0) from bound to continuum states are allowed. On the other hand, for the in-plane polarized light, *E//x* or *E//y*, the allowed transitions are those changing the angular momentum by Δl = ±1, and therefore both bound-to-bound and bound-to-continuum transitions are possible. To obtain the observed photocurrent, the final state must be either in

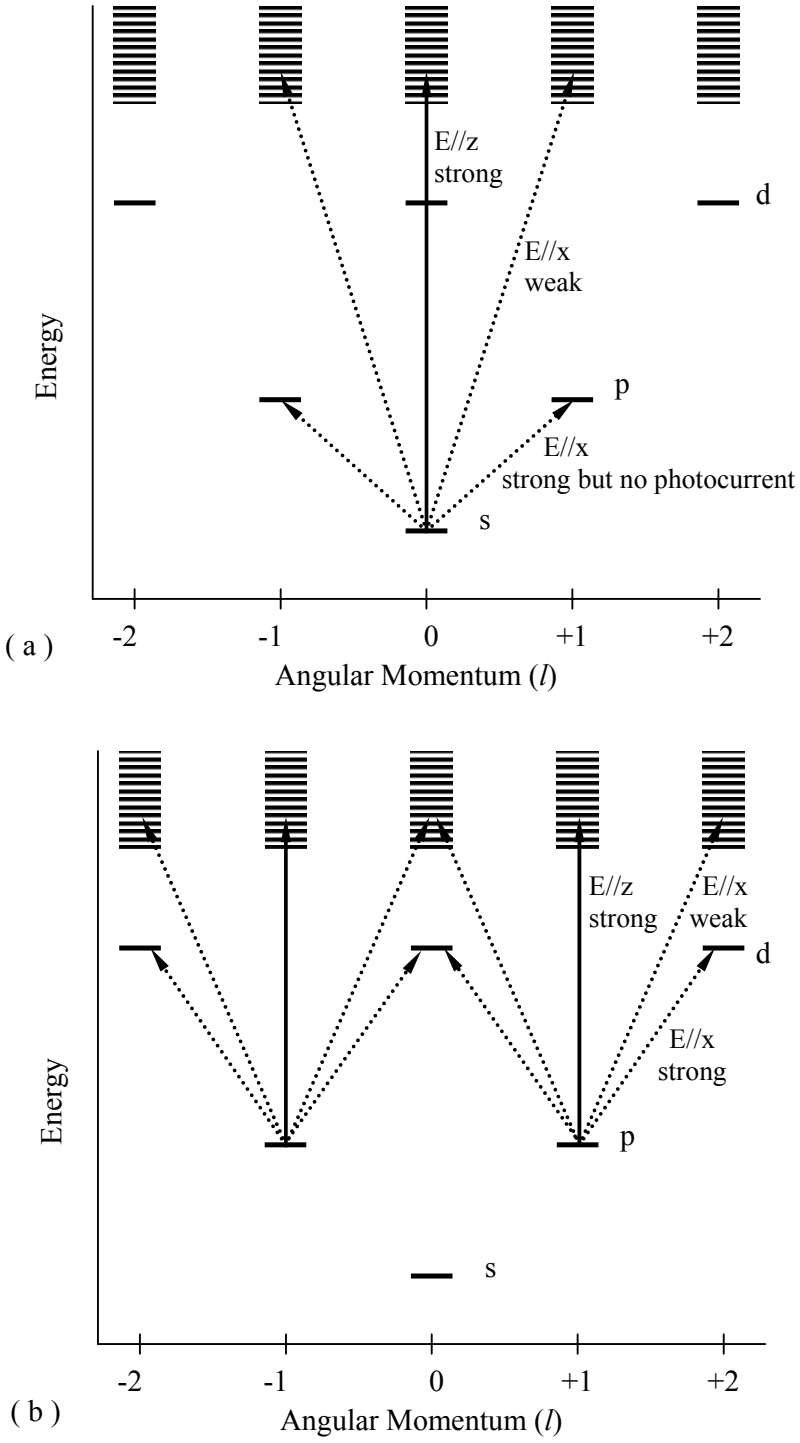

Fig. 7.2 Schematic conduction band inter-shell transitions in a self-assembled InAs/GaAs quantum dot. Solid and dotted arrows represent transitions for *E//z* and *E//x-y* polarized lights, respectively. The top part is for transitions originating from the s shell, and the bottom for p shell.

the continuum or close to the continuum, i.e., the d shell, so that the photoexcited electrons can escape. Additional details are given in [141]. Fig. 7.2 shows schematically some of these possible transitions. The solid arrows indicate transitions that are sensitive to *E//z* light whereas dotted ones are for *E//x* light. The top panel shows transitions originating from an electron occupying the s shell. For a given polarization, the transition oscillator strength is strong for going to the nearest allowed state, for example, for *E//x*, s to p is strong whereas s to continuum is weak. Similarly, the bottom panel shows transitions from the p shell.

7.4 Results and Discussion

Dark current characteristics of all samples at two different temperatures, 77 K and 6 K, are shown in Fig. 7.3. A generally expected behavior is seen with varying the number of electrons. Since the dark current is proportional to $exp(-E_a/k_BT)$ [81,121], where E_a is the activation energy and T is temperature, it decreases with decreasing number of electrons per dot because activation energy is determined by the electron number inside the dot [142]. On the other hand, when the temperature of the samples is reduced, the current due to thermally excited electrons are significantly suppressed. The irregularities below 200 pA in Fig. 7.3b is due to the electrical limit of the coaxial cable used in the measurements. Fig. 7.3b also shows clear tunneling features through the GaAs barrier especially for sample D, which are studied in more details in [142].

Fig. 7.4 shows the normalized spectral photoresponse curves of samples A, B and C under P- and S-polarized lights in the mid-infrared. For the highest doping sample (D), all the energy levels in the dots are filled with electrons (12 e^-/dot). The very small activation energy leads to a high dark current and therefore a high noise current which prevents the spectral response measurements. The measurement geometry is shown in the inset. Note that the P-polarized light contains both *E//x* (50%) and *E//z* (50%) components; whereas the S light is only *E//x*. We have chosen the *x* coordinate to coincide with the S-polarization direction. The main broad peak (Fig. 7.4a) corresponds to the transitions from s and p shells to the continuum (see also Fig. 7.2), which cover an energy range above ~130 meV. The

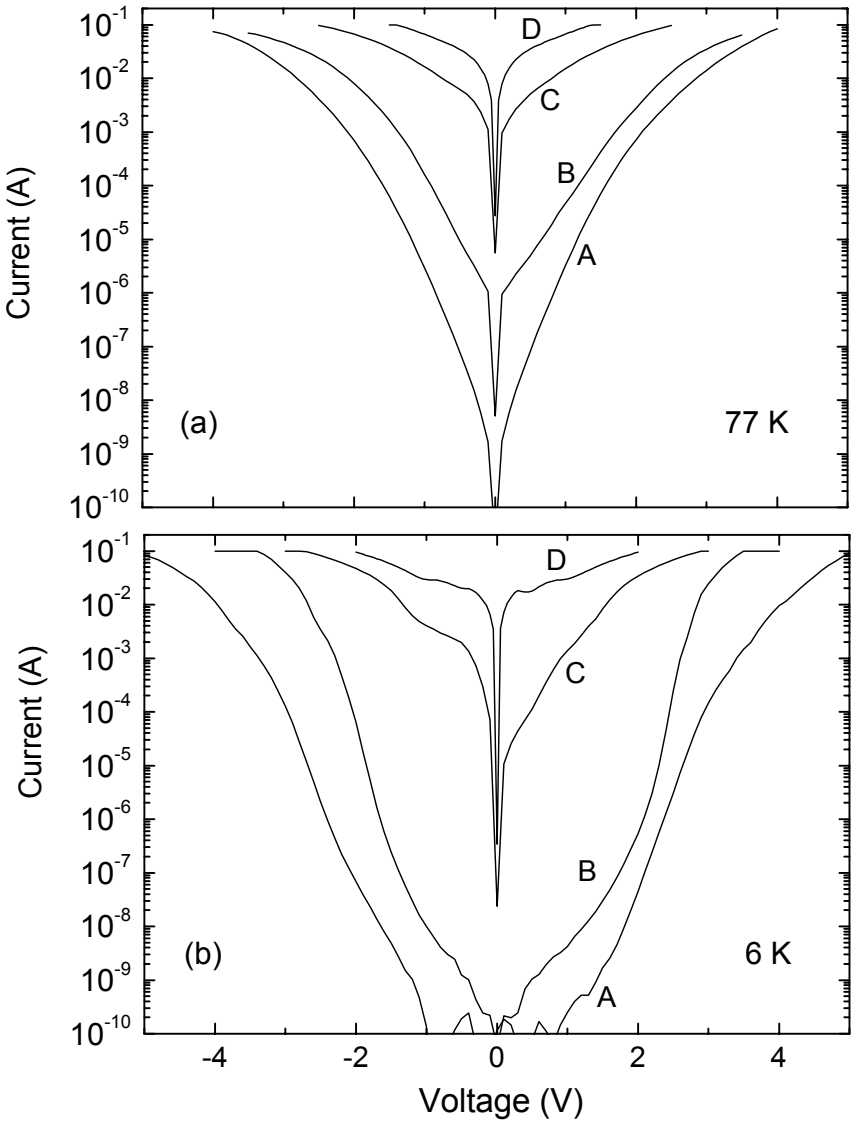

Fig. 7.3 Dark current characteristics for all samples at two different temperatures, 77 K (a) and 6 K (b).

response under S-polarized light (Fig. 7.4b) is weaker than that for P because low lying bound-to-bound transitions from s to p shell and from p to d shell exhaust most of the oscillator strengths. In contrast, the largest *E//z* oscillator strength for both s and p initial states is the one going into the continuum because there are no other lower allowed final states. As the number of electrons per QD increases, the population of the higher states is enhanced. As a result, the transitions to the continuum states from the higher p shell become more prominent and the

photoresponse curve broadens toward the lower energy region. For sample A with an average of 2 electrons per dot, ideally only the lowest s shell is occupied. However, due to the random distribution of dopants in relation to dot positions, some dots have more than 2 electrons leading to a non-zero occupation on the p shell. For samples B and C, both s and p shells are occupied. For the same reason of randomness, d shells are occupied in some dots.

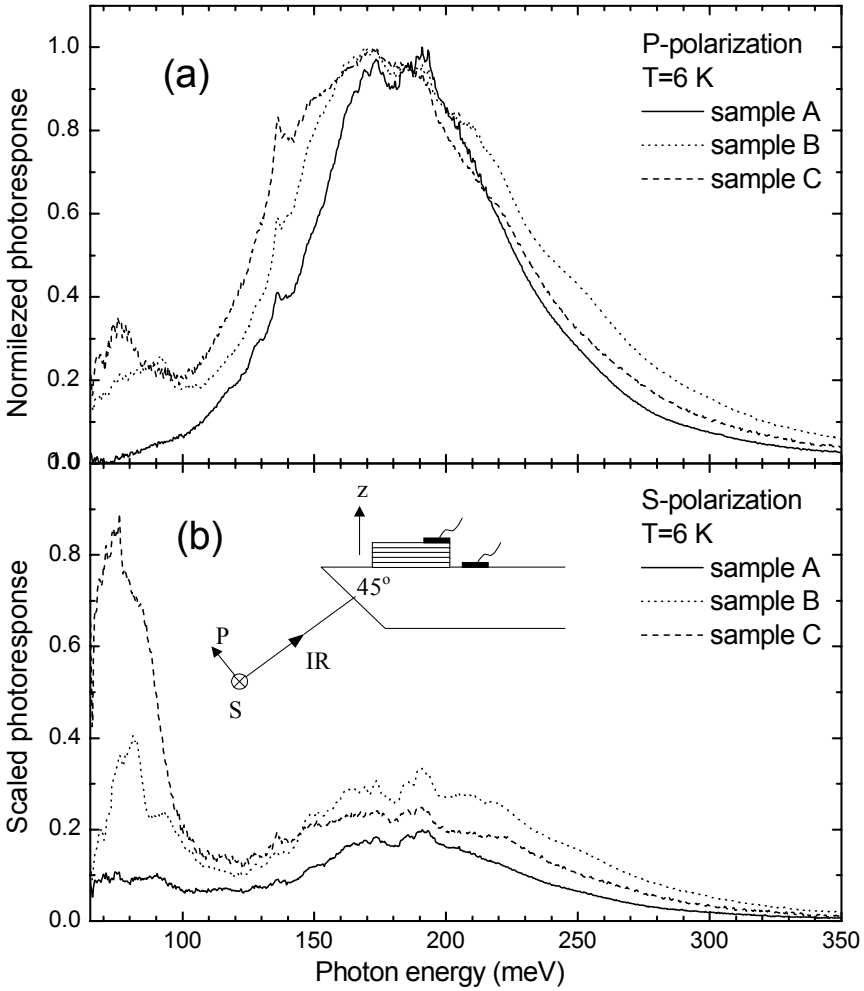

Fig. 7.4 Comparison of mid-infrared photoresponse curves of samples having different numbers of electrons per dot for (a) P-polarized and (b) S-polarized lights. The P-spectra are normalized to unity, while the S-spectra are scaled by the same amounts for comparison. The inset to the bottom panel shows the experimental geometry.

Since the peak feature in the range from 70 to 90 meV displays a strong S-polarized (*E//x*) response, it is attributed to the transition from a lower confined state to a higher one, i.e., from p to d shell (see Fig. 7.2b). This feature increases in strength with the electron number because the p shell is more occupied, and becomes comparable in height to the broad main feature for sample C shown in Fig. 7.4a. This is a ***clear*** and ***strong*** observation for in-plane polarized response in QDIPs.

The spectral response curves in the far-infrared are shown in Fig. 7.5. The behavior in this region is more complicated and we can offer only a hand-waving interpretation. For samples B and C, the peaks in the 40-70 meV range are believed to be caused by the transition from the highest occupied d shell into the continuum. The reason for peaks appearing at different positions and having different polarizations is not clear and may be due to electron-electron interactions. Phonons may also play a role since the energy scales are close to the phonon energies of the system. The dark region lying in between 32 and 37 meV is a result of longitudinal optical and transverse optical (TO) phonon absorptions. The dip at ~66 meV comes from the 2TO absorption [143]. The photoresponse spectrum in this region is thus further complicated since this entire region lies within the one- and two-phonon absorption bands. Since sample A has only 2 electrons per dot, the d shell should be completely empty. It therefore should show no response in this spectral region. This is true in experiments except just above and below the phonon dark region. The two peaks at just above and below the dark region may be caused by the phonon absorption, perhaps coupled with inter-shell transitions. It is known that if a dipole-transition resonance is close to phonon energy, the electron-phonon interaction leads to a strong modification of the spectrum and a coupled mode behavior [144]. Clearly the far-infrared characteristics need further study to arrive a fully consistent interpretation.

Fig. 7.6 shows the responsivity versus voltage characteristics of samples A, B and C at 7.14 μm (174 meV). All samples display a peak characteristic as a function of voltage. Starting from zero voltage the increase can be attributed to the increase in the carrier escape efficiency and in the transport mobility, but the reason for the decrease at larger voltages is not clear. Note the very high values of responsivity

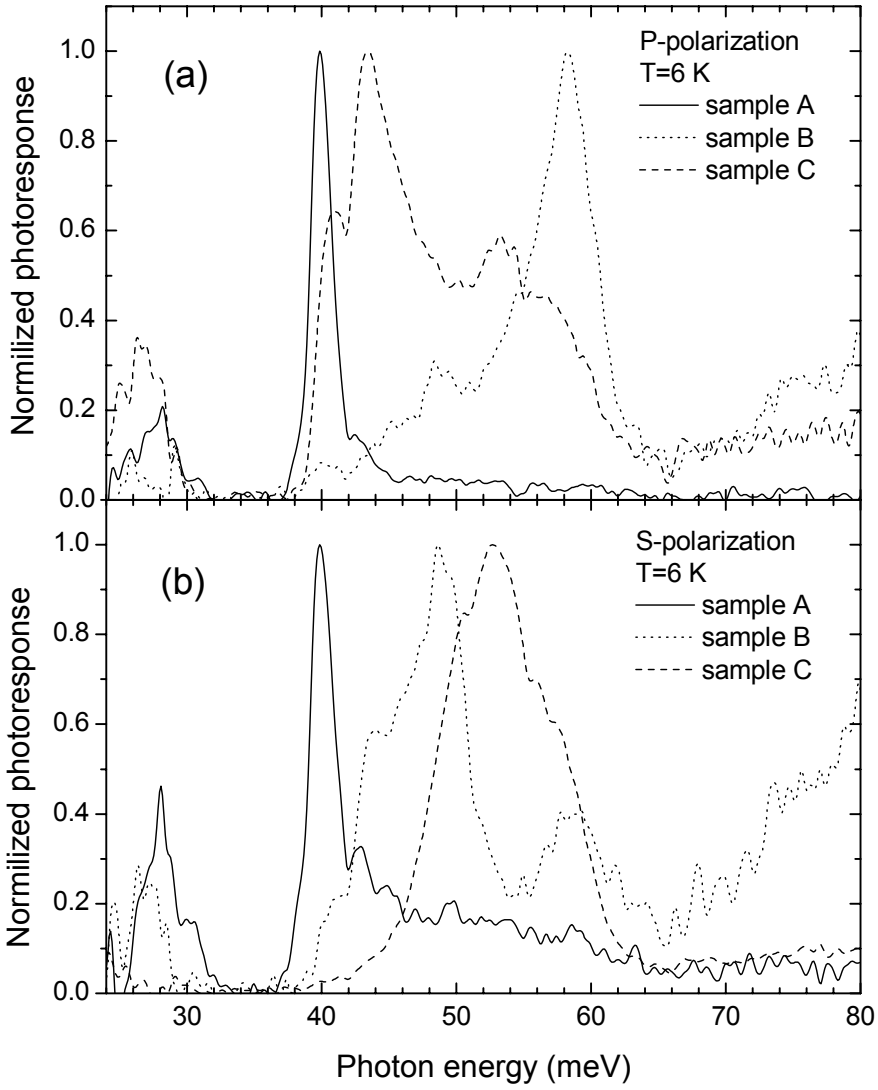

Fig. 7.5 Normalized far-infrared photoresponse curves for (a) P-polarized and (b) S-polarized lights. To compare the relative magnitudes between P and S responses, the lower panel curves should be multiplied by 0.6, 0.8, and 3.8 for sample A, B, and C, respectively, for example, the solid curve in (b) should be multiplied by 0.6 to compare with the curve in (a).

indicating a large photoconductive gain: By using Eq. (7.5) and Eq. (7.6), the photoconductive gain can be estimated speculatively as ~70 for R = 4 A/W, $h\nu$ = 0.174 eV and η = 0.01 (since the absorption in these samples is low). For drift velocity $\upsilon = 2\times10^7$ cm/s (the maximum velocity for the electrons in the GaAs [92]), and having the device length x = 1600 nm, the transit time ($\tau_{trans} = x/\upsilon$) and

therefore the life time (τ_{life}) can be found as >0.5 ns. This is a couple of order higher than that for normal QWIP [145]. This value is even larger for R > 4 A/W (sample C for instance). For samples A and B, there is a delay in the turn-on of the photoresponse as a function of voltage, and the reason again is not clear. The large asymmetry in the responsivity curve of sample C is correlated with the low temperature dark current results (see Fig. 7.3b).

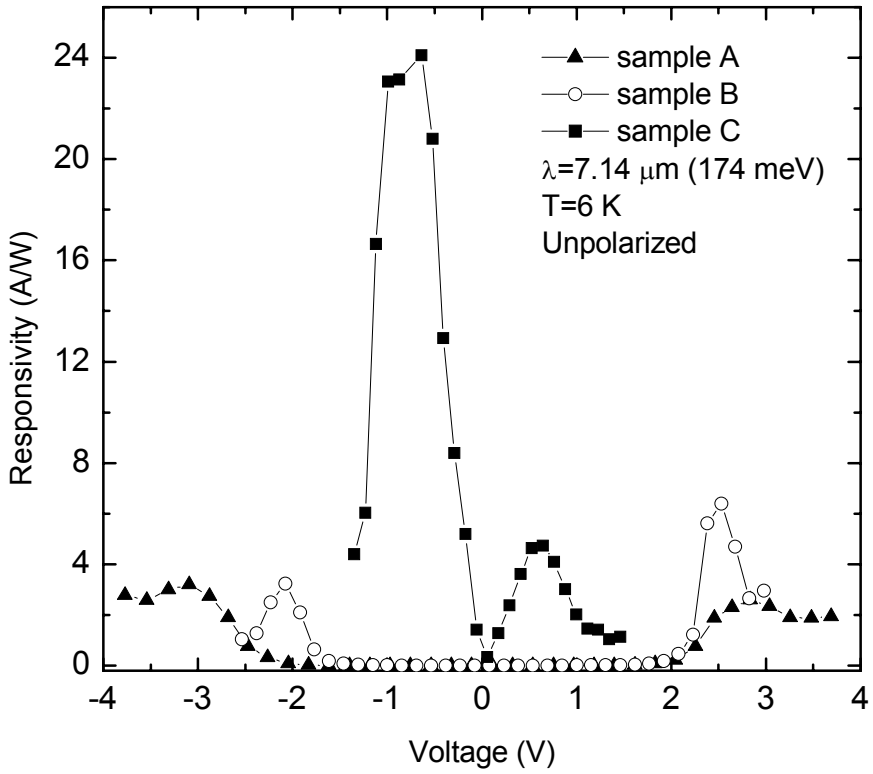

Fig. 7.6 Responsivity versus voltage characteristics for samples A, B and C at 7.14 μm (174 meV) and 6 K.

CHAPTER 8

CONCLUSION

The primary aim of this work was to study the internal photoemission (IP) mechanism of semiconductor heterojunctions used as infrared detectors in the mid/far-infrared region. In order to provide a better understanding of the experimental results, the old and recent theoretical descriptions and models were reviewed, revised and extended. The extensions incorporate the effects of the difference in the effective masses in the active region and the substrate, nonspherical-nonparabolic bands, and the energy loss per collisions on the internal quantum efficiency of the detector. The model is then completed by incorporating the wavelength and doping concentration dependent free carrier absorption to the model. Experiments done in this study have shown that the IP spectrum of SiGe/Si (in the form of Fowler plot) can be consistently described by this completed theoretical model. The secondary aim was to study on the infrared photodetectors having different detection mechanisms and different material systems to complete the picture of the infrared detector subject. Since the thesis is organized in a way that each chapter is self-contained/consistent, it would be appropriate to make conclusion for each chapter separately.

In chapter 3, the mechanisms of photocurrent generation in the SiGe/Si heterojunction internal photoemission (HIP) infrared photodetectors have been studied and a qualitative model has been presented. It has been shown that the performance of our devices depend significantly on the applied bias and the operating temperature. We obtained 31 μm and 18.2 μm cut-off wavelengths for -37

mV and 75 mV, respectively. These cut-off values were extracted by using the complete model derived in chapter 2 for semiconductor heterojunction systems. It has been shown that the experimental and theoretical curves are in a very good agreement. However, the result of the theory is not unique because of the many adjustable parameters involved in the calculations such as L_e, L_p, and $\hbar\omega$. Unfortunately, reliable values for these parameters are not available and they are not easily measurable quantities. The tunability feature seen in our devices can be utilized to design new devices whose cut-off wavelength can be set by the externally applied voltage. However, device parameters should be optimized for an efficient application.

The effects of double barrier on the photoresponse spectrum of the SiGe/Si heterojunction internal photoemission (HIP) infrared photodetectors have been studied in chapter 4. When compared with the single barrier sample that has nominally the same parameters, it has been shown that the double barrier sample acts as a temperature tunable infrared photodetector. From the Fowler analysis we obtained 22.5 μm and 12.6 μm cut-off wavelength values for 10 K and 50 K, respectively. Even though the model described in chapter 2 might have not been applicable to analyze this double-barrier sample, the cut-off values were extracted by using this model on the basis of the expectation that it must be more reliable than the other models.

In chapter 5, an example for metal(silicide)/semiconductor systems has been investigated. We have shown that a theoretical model that includes the effects of scattering in the PtSi film can consistently describe the internal photoemission spectrum of a PtSi-Si diode. It has been also shown that the unexpected dip in the spectrum around 0.4 eV is due to the absorption of light by the ice layer formed on the sample's surface during cooling. The formation of ice layer can be reduced by using more effective pumping systems. The effect of the ice formation on the detector should be taken into account when designing a detector operating in the mid-infrared region.

The dual-band detection with the intersubband part having both bound-to-bound and bound-to-continuum transitions for InGaAs/InP quantum wells which are 2-dimensional systems have been demonstrated in chapter 6. These devices have shown high responsivity, gain and avalanche multiplication at high bias. The high responsivity demonstrated in QWIPs with InGaAs/InP materials may be useful for imaging applications where a short integration time is required.

Finally in chapter 7, an example of 0-dimensional systems has been studied. The detailed optical characterizations on InAs/GaAs self-assembled quantum dot infrared photodetectors with various doping levels have been made. The spectral photoresponse curves in a wide spectral region from the mid- to far-infrared have been reported. Polarization behaviors of transitions and effects of the number of electrons on the photoresponse spectra have been demonstrated. A strong in-plane polarized bound-to-bound transition feature has been observed. A simple picture has been presented to account for the observed features.

REFERENCES

[1] J. M. Lloyd, *Thermal Imaging Systems*, Plenum Press, New York, 1975

[2] H. A. Gebbie, W. R. Harding, C. Hilsum, A. W. Pryce, and V. Roberts, *Proc. of the Royal Society London* **A206**, 87 (1951)

[3] R. D. Hudson, and J. W. Hudson (eds.), *Infrared Detectors, Benchmark Papers in Optics 2*, Halsted Press, Pennsylvania, 1975

[4] R. J. Keyes (ed), *Optical and Infrared Detectors, Topics in Applied Physics* 19, Springer-Verlag, 1977

[5] E. L. Dereniak and G. D. Boreman, *Infrared Detectors and Systems*, John Wiley & Sons, 1996

[6] J. Piotrowski, and A. Rogalski, *Sensors and Actuators A* **67**, 146 (1998)

[7] M. H. Francombe and J. L. Vossen (eds), Advences in Research and Development, *Thin Films* **23**, Academic Press, 1998

[8] A. Rogalski, *Inf. Phys. & Tech.* **41**, 213 (2000)

[9] A.G.U. Perera and H.C. Liu (eds), *Semiconductor Optical and Electro-Optical Devices, Handbook of Thin Film Devices 2*, Academic Press, 2000

[10] A. Rogalski, *Progress in Quantum Electronics* **27**, 59 (2003)

[11] A. Rogalski, *J. Appl. Phys*. **93**, 4355 (2003)

[12] H. C. Liu and F. Capasso (eds), *Intersubband Transitions in Quantum wells: Physics and Device Applications I, Semiconductor and Semimetals* **62**, Academic Press, 2000

[13] A. Rose, *Concepts in Photoconductivity and Allied Problems*, Interscience, New York, 1963

[14] I. Bhat (ed), *J. Electron. Mater.* **25** (no 8), 1133-1415 (1996)

[15] W. D. Lawson, S. Nielsen, E. H. Putley, And A. S. Young, *J. Phys. Chem. Solids* **9**, 325 (1959)

[16] J. L. Schmit and E. L. Stelzer, *J. Appl. Phys.* **40**, 4865 (1969)

[17] G. L. Hansen, J. L. Schmit, and T. N. Casselman, *J. Appl. Phys.* **53**, 7099 (1982)

[18] M. Kimata and N. Tubouchi in: A. Rogalski (ed), *Infrared Photon Detectors*, SPIE Opt. Eng. Press, 1995, pp. 299-349 (Chapter 9)

[19] F. D. Shephard in: M. H. Francombe and J. L. Vossen (eds), *Research and Development, Thin Films* **23**, Academic Press, 1998, pp. 83-114

[20] E. H. Rhoderick and R. H. Williams, *Metal-Semiconductor Contacts*, Clarendon Press, Oxford, 1988

[21] J. H. Werner and U. Rau, *Springer Series in Electronics and Photonics*, **32**, 89, 1994

[22] W. Schottky, *Naturwiss.* **26**, 843, 1938

[23] N. F. Mott, *Proc. Chambr. Phil. Soc.* **34**, 568, 1938

[24] J. Bardeen, *Phys. Rev.* **71**, 717, 1947

[25] V. Heine, *Phys. Rev.* **A138**, 1689, 1965

[26] H. Elabd and W. F. Kosonocky, *RCA Review* **43**, 569, 1982

[27] P. W. Pellegrini, A. Golubovic, C. E. Ludington, and M. M. Weeks, *IEDM Tech. Dig.*, p157-160 (1982)

[28] B. Y. Tsaur, M. M. Weeks, R. Trubiano, P. W. Pellegrini, T. R. Yew, *IEEE Elect. Dev. Lett*. **9**, 650 (1988)

[29] F. D. Shephard, V. E. Vickers, and A. C. Yang, *U.S. Patent* 3,603,847 (1971)

[30] T. L. Lin and J. Maserjian, *Appl. Phys. Lett*. **57**, 1422 (1990)

[31] M. D. Petroff and M. G. Stapelbroek, *U.S. Patent* 4,568,960 filed in 1980, granted in 1986

[32] S. B. Stetson, D. B. Reynolds, M. G. Stapelbroek and R. L. Stemer, *Proc. SPIE* **686**, 48 (1986)

[33] F. Szmulowicz and F. L. Madarsz, *J. Appl. Phys*. **62**, 2533 (1987)

[34] S. Tohyama, N. Teranishi, K. Konuma, M. Nishimura, K. Arai, and E. Oda, *IEEE Trans. Electron Dev*. **38**, 1136 (1991)

[35] S. Tohyama, A. Tanabe, and N. Teranishi, *IEEE Trans. on Elec. Dev.*, **41**, 1535 (1994)

[36] A. G. U. Perera, H. X. Yuan and M. H. Francombe, *J. Appl. Phys*. **77**, 915 (1995)

[37] A. G. U. Perera in: A.G.U. Perera and H.C. Liu (eds), *Semiconductor Optical and Electro-Optical Devices, Handbook of Thin Film Devices* **2**, Academic Press, 2000, pp. 135-170 (Chapter 5)

[38] T. Ando, A. B. Fowler, and F. Stern, *Rev. Mod. Phys*. **54**, 437 (1982)

[39] L. Esaki and H. Sakaki, *IBM Tech. Discl. Bull*. **20**, 2456 (1977)

[40] J. S. Smith, L. C. Chiu, S. Margalit, A. Yariv, and A. Y. Cho, *J. Vac. Sci. Technol. B* **1**, 376 (1983)

[41] L. C. West and S. J. Eglash, *Appl. Phys. Lett*. **46**, 1156 (1985)

[42] B. F. Levine, K. K. Choi, C. G. Bethea, J. Walker, and R. J. Malik, *Appl. Phys. Lett.* **50**, 1092 (1987)

[43] B. F. Levine, *J. Appl. Phys.* **74**, R1 (1993)

[44] J. L. Pan and C. G. Fonstad, *Mat. Sci. and Eng*. **28**, 65 (2000)

[45] L. Jacak, P. Hawrylak and A. Wojs, *Quantum Dots*, Springer-Verlag, 1998

[46] S. Fafard, Z. R. Wasilewski, C. N. Allen, D. Picard, P. G. Piva, and J. P. McCaffrey, *Superlattices and Microstructures* **25**, 87 (1999)

[47] S. Fafard, H.C. Liu, Z. R. Wasilewski, J. P. McCaffrey,M. Spanner, S. Raymond, C. N. Allen, K. Hinzer, J.Lapointe, C. Struby, M. Gao, P. Hawrylak, C. Gould, A. Sachrajda, and P. Zawadzki, *Proc. SPIE* **4078**, 100 (2000)

[48] H. C. Liu, M. Gao, J. McCaffrey, Z. R. Wasilewski and S. Fafard, *Appl. Phys. Lett*. **78**, 79 (2001)

[49] J. Phillips, K. Kamath and P. Bhattacharya, *Appl. Phys. Lett*. **72**, 2020 (1998)

[50] D. Pan, E. Towe and S. Kennerly, *Appl. Phys. Lett*. **73**, 1937 (1998)

[51] C. Miesner, O. Röthig, K. Brunner, and G. Abstreiter, *Physica E* **7**, 146 (2000)

[52] C. Miesner, K. Brunner, and G. Abstreiter, *Inf. Phys. & Techn.* **42**, 461 (2001)

[53] S. Tong, J. L. Liu, J. Wan and L. L. Wang, *Appl. Phys. Lett*. **80**, 1189 (2002)

[54] C. Kittel, *Introduction to Solid State Physics*, Wiley, 1986

[55] R. W. Boyd, *Radiometry and the Detection of Optical Radiation*, Wiley, 1983

[56] N. B. Stevens in: R. K. Willardson and A. C. Beer (eds), *Infrared Detectors, Semiconductors and Semimetals* **5**, Academic Press, 1970

[57] R. H. Fowler, *Phys. Rev*. **38**, 45 (1931)

[58] J. Cohen, J. Vilms, R. J. Archer, *Final Rep*. **AFCRL-68-0651**, Hewlett-Packard Labs, Palo Alto, CA (1968)

[59] V. E. Vickers, *Appl. Optics* **10**, 2190 (1971)

[60] V. L. Dalal, *J. Appl. Phys.* **42**, 2274 (1971)

[61] J. M. Mooney, J. Silverman, *IEEE Trans. Electron Devices* **ED-32**, 33 (1985)

[62] J. M. Mooney, *Ph D. Thesis*, University of Arizona, 1986

[63] B-Y. Tsaur, C. K. Chen, and S. A. Marino, *SPIE* **1540**, 580 (1991)

[64] H. C. Liu, L. Li, J.-M. Baribeau, M. Buchanan, and J. G. Simmons, *J. Appl. Phys*. **71**, 2039 (1992)

[65] R. Strong, D. W. Greve, P. Pellegrini, and M. Weeks, *J. Appl. Phys*. **82**, 5199 (1997)

[66] J. S. Park, T. L. Lin, E. W. Jones, H. M. Del Castillo, and S. D. Gunapala, *Appl. Phys. Lett*. **64**, 2370 (1994)

[67] T. L. Lin, J. S. Park, S. D. Gunapala, E. W. Jones, and H. M. Del Castillo, *IEEE Elect. Dev. Lett*. **15**, 103 (1994)

[68] R. Strong, R. Misra, D. W. Greve, and P. C. Zalm, *J. Appl. Phys*. **82**, 5191 (1997)

[69] Y. Fu, S. C. Jain, M. Willander, and J. J. Loferski, *J. Appl. Phys*. **74**, 402 (1993)

[70] B. Aslan, *M. S. Thesis*, Middle East Technical University, 1999

[71] H. Hara and Y. Nishi, *J. Phys. Soc. Japan* **21**, 1222 (1966)

[72] H. Presting, J. Konle, M. Hepp, H. Kibbel, K. Thonke, R. Sauer, E. Corbin, and M. Jaros, *Opt. Eng*. **39**, 2624 (2000)

[73] J. I. Pankove, *Optical Processes in Semiconductors*, Prentice-Hall, 1971

[74] R. Wang, P. Chen, P. Tsien, G. Luo, J. Zhou, and A. Liu, *Inf. Phys. & Tech*. **39**, 293 (1998)

[75] H. Wada, M. Nagashima, K. Hayashi, J. Nakanishi, M. Kimata, N. Kumada, and S. Ito, *SPIE* **3698**, 72 (1999)

[76] B. Aslan, and R. Turan, *Inf. Phys. & Tech*. **43**, 85 (2002)

[77] G. Masini, L. Colace, F. Galluzzi, G. Assanto, T. P. Pearsall, and H. Presting, *Appl. Phys. Lett*. **70**, 3194 (1997)

[78] J. R. Jimenez, X. Xiao, J. C. Sturm, and P. W. Pellegrini, *Appl. Phys. Lett*. **67**, 506 (1995)

[79] C. Schwartz and H. von Känel, *J. Appl. Phys*. **79**, 8798 (1996)

[80] L. Pahun, Y. Campidelli, F. A. d'Avitaya, and P. A. Badoz, *Appl. Phys. Lett*. **60**, 1166 (1992)

[81] H. C. Liu in: H. C. Liu and F. Capasso (eds), *Intersubband Transition in Quantum Wells: Physics and Device Applications I*, Academic, San Diego, 2000 Chapter 3

[82] B. Aslan, R. Turan, H.C. Liu, M. Buchanan, and J.-M. Baribeau, *Semicond. Sci. Technol.* **19**, 399 (2004)

[83] H. Lafontaine, D. C. Houghton, D. Elliot, N. L. Rowell, J.-M. Baribeau, S. Laframboise, G. I Sproule, and S. J. Rolfe, *Vac. Sci. Technol*. **B14**, 1675 (1996)

[84] T. L. Lin, A. Ksendzov, S. M. Dejewski, E. W. Jones, R. W. Fathauer, T. N. Krabach, and J. Maserjian, *IEEE Trans. Elect. Dev*. **38**, 1141 (1991)

[85] H.C. Liu, M. Buchanan, and J.-M. Baribeau, *Appl. Phys. Lett*. **62**, 988 (1993)

[86] R. Banisch, B. Tillack, K. Pressel, R. Barth, and H. Erzgräber, *Thin Solid Films* **294**, 254 (1997)

[87] C. Renard, S. Bodnar, P. A. Badoz, and I. Sagnes, *J. Cryst. Growth* **157**, 195 (1995)

[88] D. B. Raynolds, D. H. Seib, S. B. Stetson, T. Herter, N. Rowlands, and J. Schoenwald, *IEEE Trans. Nuc. Sci*. **36**, 857 (1989)

[89] J. E. Huffman, A. G. Crouse, B. L. Halleck, T. V. Downes, and T. L. Herter, *J. Appl. Phys*. **72**, 273 (1992)

[90] V. V. Rylkov, J. Leotin, L. Asadauskas, B. A. Aronzon, and D. Yu. Kovalev, *J. Appl. Phys*. **91**, 4511 (2002)

[91] H. C. Liu, J. Li, M. Buchanan, J.-M. Baribeau, and J. G. Simmons, *Elect. Lett*. **29**, 407 (1993)

[92] S. M. Sze, *Physics of Semiconductor Devices*, John Wiley & Sons, 2nd ed., 1981

[93] Ö. S. Anilturk, R. Turan, *Solid-State Elect*. **44**, 41 (2000)

[94] A. Köck, E. Gornik, G, Abstreiter, G. Böhm, M. Walther, and G. Weimann, *Appl. Phys. Lett*. **60**, 2011 (1992)

[95] B. Aslan, R. Turan, H.C. Liu, M. Buchanan, J.-M. Baribeau, and P. Chow-Chong, *Appl. Phys. B*. **78**, 225 (2004)

[96] W. F. Kosonocky, F. V. Shallcross, T. S. Villani, *IEEE Transactions on Electron Devices* **ED-32**, 1564 (1985)

[97] K. Konuma, S. T. Tohyama, A. Tanabe, N. Teranishi, K. Masubuchi, T. Saito, and T. Muramatsu, *IEEE Transactions on Electron Devices* **39**, 1633 (1992)

[98] V. W. L. Chin, M. A. Green, and J. W. V. Storey, *Solid-State Electronics* **36**, 1107 (1993)

[99] V. W. L. Chin, J.W.V. Storey, and M. A. Green, *Solid-State Electronics* **39**, 277 (1996)

[100] J. M. Mooney, *J. Appl. Phys*. **65**, 2869 (1989)

[101] K. Komuma, Y. Asano, and K. Hirose, *Phys.Rev*. **B 51**, 13187 (1995)

[102] A. Czernik, H. Palm, W. Cabanski, M. Schulz, and U. Suckow, *Appl. Phys*. **A 55**, 180 (1992)

[103] D. E. Mercer and C. R. Helms, *J. Appl. Phys*. **65**, 5035 (1989)

[104] X. Xiao, J. C. Sturm, S. R. Parihar, S. A. Lyon, D. Meyerhofer, S. Palfrey, and F. V. Shallcross, *IEEE Electron Device Letters* **14**, 199 (1993)

[105] H. C. Liu, M. Buchanan and Z. R. Wasilewski, J. Appl. Phys. **83**, 6178 (1998)

[106] T. L. Lin and J. M. Iannelli, *Appl. Phys. Lett*. **56**, 2013 (1990)

[107] F. Nava, S. Valeri, G. Majni, A. Cembali, G. Pignatel, and G. Queirolo, *J. Appl. Phys.* **52**, 6641 (1981)

[108] Murarka et al., *J. Appl. Phys.* **54**, 6943 (1983)

[109] G. Warren, *Appl. Opt.* **23**, 1206 (1984)

[110] B. Aslan, H. C. Liu, M. Buchanan and Z. R. Wasilewski, *J. Appl. Phys*. **91**, 10230 (2002)

[111] B. Aslan, H.C. Liu, A. Bezinger, P. J. Poole, M. Buchanan, R. Rehm, and H. Schneider, *Semicond. Sci. Technol*. **19**, 442 (2004)

[112] S. D. Gunapala and S. V. Bandara in: H. C. Liu and F. Capasso (eds), *Intersubband Transition in Quantum Wells: Physics and Device Applications I*, Academic, San Diego, 2000 Chapter 4

[113] H. C. Liu, C. Y. Song, E. Dupont, P. J. Poole. P. H. Wilson, B. J. Robinson and D. A. Thompson, *Electron. Lett.* **35**, 2055 (1999)

[114] H. C. Liu, C. Y. Song, A. Shen, M. Gao, Z. R. Wasilewski and M. Buchanan, *Appl. Phys. Lett.* **77**, 2437 (2000)

[115] H. Schneider, *Appl. Phys. Lett.* **82**, 4376 (2003)

[116] R. Rehm, H. Schneider, M. Walther, P. Koidl and G. Weimann, *Appl. Phys. Lett.* **82**, 2907 (2003)

[117] H. C. Liu, *J. Appl. Phys.* **73**, 3062 (1993)

[118] B. Xing, H. C. Liu, P. H. Wilson, M. Buchanan, Z. R. Wasilewski and J. G. Simmons, *J. Appl. Phys.* **76**, 1889 (1994)

[119] S. Datta, *Quantum Phenomena*, Addison-Wesley, 1989

[120] L. Chu, A. Zrenner, G. Bohm, and G. Abstreiter, *Appl. Phys. Lett*. **76**, 1944 (2000)

[121] H. C. Liu, S. Fafard, R. Dudek and Z. R. Wasilewski, *Photonics West*, paper 4646-11 (2002)

[122] B. Aslan, H. C. Liu, M. Korkusinski, S.-J. Cheng, and P. Hawrylak, *Appl. Phys. Lett*. **82**, 630 (2003)

[123] H. C. Liu, B. Aslan, M. Korkusinski, S.-J. Cheng, and P. Hawrylak, *Inf. Phys. & Tech.* **44**, 503 (2003)

[124] H. C. Liu, M. Buchanan, and Z. R. Wasilewski, *Appl. Phys. Lett*. **72**, 1682 (1998)

[125] S. Fafard, R. Leon, D. Leonard, J. L. Merz, and P. M. Petroff, *Phys. Rev. B* **52**, 5752 (1995)

[126] M. Bayer, O. Stern, P. Hawrylak, S. Fafard, and A. Forchel, *Nature* (London) **405**, 923 (2000)

[127] K. W. Berryman, S. A. Lyon, and M. Segev, *Appl. Phys. Lett*. **70**, 1861 (1997)

[128] L. Chu, A. Zrenner, G. Bohm, and G. Abstreiter, *Appl. Phys. Lett*. **75**, 2599 (1999)

[129] A. D. Stiff, S. Krishna, P. Bhattacharya, and S. Kennerly, *Appl. Phys. Lett*. **79**, 421 (2001)

[130] S. Raghavan, P. Potella, S. Stintz, B. Fuchs, S. Krishna, C. Morath, D. A. Cardimona, and S. W. Kennerly, *Appl. Phys. Lett*. **81**, 1369 (2002)

[131] S. J. Xu, S. J. Chua, T. Mei, X. C. Wang, X. H. Zhang, G. Karunasiri, W. J. Fan, C. H. Wang, J. Jiang, S. Wang, and X. G. Xie, *Appl. Phys. Lett*. **73**, 3153 (1998)

[132] N. Horiguchi, T. Futatsugi, Y. Nakata, N. Yokoyama, T. Mankad, and P. M. Petroff, Jpn. *J. Appl. Phys*. **38**, 2559 (1999)

[133] S. Sauvage, P. Boucaud, T. Brunhes, V. Immer, E. Finkman, and J.-M. Gérard, *Appl. Phys. Lett*. **78**, 2327 (2001)

[134] A. Weber, O. Gauthier-Lafaye, F. H. Julien, J. Brault, M. Gendry, Y. Désieres and T. Benyattou, *Appl. Phys. Lett*. **7**4, 413 (1999)

[135] V. Ryzhii, *Semicond. Sci. Technol*. **11**, 759 (1996)

[136] U. Bockelmann and G. Bastard, *Phys. Rev. B* **42**, 8947 (1990)

[137] J. Urayama, T. B. Norris, J. Singh, and P. Bhattacharya, *Phys. Rev. Lett*. **86**, 4930 (2001)

[138] S. Fafard, Z. R. Wasilewski, C. N. Allen, D. Picard, M. Spanner, J. P. McCaffrey and P. G. Piva, *Phys. Rev. B* **59**, 15368 (1999)

[139] P. Hawrylak, S. Fafard and Z. R. Wasilewski, *Condensed Matter News* **7** (issue 4), 16 (1999)

[140] M. Korkusinski and P. Hawrylak, *Phys. Rev. B* **63**, 195311 (2001)

[141] P. Hawrylak, M. Korkusinski, S. Fafard, R. Dudek and H. C. Liu, *Physica E* **13**, 246 (2002)

[142] J.-Y. Duboz, H. C. Liu, Z. R. Wasilewski, M. Byloos and R. Dudek, *J. Appl. Phys*. **93**, 1320 (2003)

[143] M. J. Howes and D. V. Morgan (eds), *Gallium Arsenide: Material, Devices and Circuits*, Wiley, Chichester, 1985

[144] H. C. Liu, C. Y. Song, Z. R. Wasilewski, A. J. SpringThorpe, J. C. Cao, C. Dharma-wardana, G. C. Aers, D. J. Lockwood and J. A. Gupta, *Phys. Rev. Lett*. **90**, 077402 (2003)

[145] H. C. Liu, *Appl. Phys. Lett*. **60**, 1507 (1992)

VITA

Bülent Aslan was born in Ankara on July 16, 1974. He received his B.S. and M.S. degrees in Physics from the Middle East Technical University (METU) in 1996 and 1999, respectively. Title of his master thesis is "Internal Photoemission Spectroscopy for PtSi/Si and Pt/SiGe Schottky Type Infrared Detectors". He has been working as a research/teaching assistant in the Department of Physics, METU. Between February 2002 and February 2003, he worked as a Visiting Researcher in Quantum Devices Group, Institute for Microstructural Sciences, NRC, Ottawa, Canada.

List of Publications of Bülent Aslan:

1. "Double-barrier long wavelength SiGe/Si heterojunction internal photoemission infrared photodetectors" **B. Aslan**, R. Turan, H.C. Liu, J.-M. Baribeau, M. Buchanan and P.C. Chong, *Applied Physics B* **78**, 225 (2004).
2. "High responsivity, dual-band response and intraband avalanche multiplication in InGaAs/InP quantum well photodetectors" **B. Aslan**, H.C. Liu, A. Bezinger, P. J. Poole, M. Buchanan, *Semiconductor Science and Technology* **19,** 442 (2004).
3. "Mechanisms of photocurrent generation in SiGe/Si HIP infrared photodetectors" **B. Aslan**, R. Turan, H.C. Liu, and J.-M. Baribeau, *Semiconductor Science and Technology* **19**, 399 (2004).
4. "Detailed characterization of a systematic set of quantum dot infrared photodetectors" H.C.Liu, **B.Aslan**, M.Korkusinski, S.-J.Cheng, P.Hawrylak, *Infrared Physics & Technology* **44**, 503 (2003).

5. "Response spectra from mid- to far-infrared, polarization behaviors, and effects of electron numbers in quantum-dot photodetectors" **B. Aslan**, H. C. Liu, M. Korkusinski, S.-J. Cheng, and P. Hawrylak, *Applied Physics Letters* **82** 630 (2003).
6. "Erratum: "Short wavelength (1–4 μm) infrared detectors using intersubband transitions in GaAs-based quantum wells" [J. Appl. Phys. **83**, 6178 (1998)]" **B. Aslan**, H. C. Liu, M. Buchanan, and Z. R. Wasilewski, *Journal of Applied Physics* **91**, 10230 (2002).
7. "On the internal photoemission spectrum of PtSi/p-Si infrared detectors", **B. Aslan** and R. Turan, *Infrared Physics & Technology* **43**, 85 (2002).
8. "Observation of strain relaxation in $Si_{1-x}Ge_x$ layers by optical and electrical characterization of Schottky junction", R. Turan, **B. Aslan**, O. Nur, M.Y.A. Yousif and M. Willander, *Applied Physics A* **72**, 587 (2001).
9. "Internal photoemission spectroscopy for a PtSi/p-Si Schottky junction", **B. Aslan** and R. Turan, *Turkish Journal of Physics* **24**, 577 (2000).
10. "Effect of layer relaxation on the internal photoemission in $Pt/Si_{1-x}Ge_x$ Schottky barrier type infrared detectors", **B. Aslan**, R. Turan, O. Nur, M. Karlsteen and M. Willander, *Material Research Society Symposium Proceedings* **607**, 235 (2000).
11. "Internal photoemission spectroscopy for a PtSi/p-Si Schottky junction", **B. Aslan** and R. Turan, *Proceeding of International School of Solid State Physics* **330** (2000), World Scientific.
12. "Correlation between barrier height and band offsets in $metal/Si_{1-x}Ge_x/Si$ heterostructures", O. Nur, M. Karlsteen, M. Willander, R. Turan, **B. Aslan**, M.O. Tanner and K.L. Wang, *Applied Physics Letters* **73** (26), 3920 (1998).

International conferences/meetings attended:

1. Materials Research Society (MRS) 1999 Fall Meeting, Boston - USA, November 29 – December 2, 1999
   (Poster presentation: Effect of Layer Relaxation on the Internal Photoemission in $Pt/Si_{1-x}Ge_x$ Schottky Barrier Type Infrared Detectors)

2. International School of Solid State Physics, 16th Course: Silicides: Fundamentals and Applications, Erice - Italy, June 5-16, 1999
   (Poster presentation: Internal Photoemission Spectroscopy for a PtSi/p-Si Schottky Junction)

National conferences/meetings attended:

1. 5th National Optic, Electro-optic, and Photonic Meeting, Ankara - Turkey, December 12, 2003
   (Oral presentation: InAs/GaAs Quantum Dot and SiGe/Si Heterojunction Infrared Detectors.)
2. 3rd National Electro-optic Meeting, Ankara - Turkey, November 2, 2001
   (Oral presentation: Pt Based Schottky Type Infrared Detectors.)